Ventilation of oxygen minimum zones by geostrophic turbulence in a shallow water model

by

Eike Köhn

Master's thesis

submitted in partial fulfilment of the requirements
for the degree of Master of Science
in Climate Physics (Meteorology and Physical Oceanography)
at the Faculty of Mathematics and Natural Sciences
at the Christian-Albrechts-Universität zu Kiel

1st Supervisor: Prof. Dr. Martin Claus
2nd Supervisor: Prof. Dr. Richard J. Greatbatch

Kiel, Germany
April 2018

C | A | U
Christian-Albrechts-Universität zu Kiel

GEOMAR

ABSTRACT

Increased observational efforts have revealed a multidecadal decrease of oxygen concentrations with superimposed interannual to decadal variability in the oxygen minimum zone (OMZ) of the eastern tropical North Atlantic (ETNA). Recent studies have linked this variability to long-term changes in the ventilation by the latitudinally alternating zonal jets (LAZJs).

In this study, a 1.5 layer non-linear shallow water model coupled to an advection-diffusion model is employed in basins with either rectangular or Atlantic geometry to obtain a conceptual understanding of the influence of the LAZJs on the ventilation of the ETNA OMZ. Using an equatorial annual period forcing, westward propagating off-equatorial Rossby waves are generated that subsequently break up into non-linear eddies. The responsible non-linear triad instability mechanism thereby sets the amplitude and size of the generated eddies, which rectify to LAZJs when temporally averaged. An oxygen-mimicking tracer is transported by the resulting velocity field, forming a region with minimum tracer concentration whose location is in general agreement with the observed ETNA OMZ. The thickness-weighted tracer budget reveals that the Eulerian mean advective flux convergence outweighs the eddy advective flux convergence in balancing the strongly simplified tracer consumption. Thickness-weighted averaging the advective flux convergence also yields an eddy mixing term which is shown to play an important role in the budget and is analysed in more detail. Despite the purely annual period forcing, interannual to decadal and longer tracer variability is excited in the basin, including the region of the ETNA OMZ. A comparison between modelled and observed oxygen trends in the lower OMZ does not lead to a rejection of the null hypothesis that the observed decadal oxygen trends are part of the system's intrinsic variability. However, the observed pronounced decadal oxygen decrease in the upper OMZ during 2006-2013 is not reproduced by the model. The picture is reversed on a multidecadal time scale. In contrast to the upper OMZ, the multidecadal oxygen

decrease in the lower OMZ is not reproduced by the idealised model. While this would support the idea of an anthropogenically driven long-term deoxygenation of the lower OMZ, it is important to bear the simplicity and shortcomings of the model in mind. Furthermore, the sparsity in measured oxygen data prior to the recently increased observational efforts complicates the reliable estimation of multidecadal trends.

ZUSAMMENFASSUNG

Vermehrte Beobachtungen haben eine multidekadische Verringerung von Sauerstoffkonzentrationen mit überlagerten interannualen bis dekadischen Schwankungen in der Sauerstoffminimumzone (OMZ) des östlichen tropischen Nordatlantiks (ETNA) erkennen lassen. Kürzlich erschienene Studien verknüpfen diese Variabilität mit langzeitlichen Veränderungen in der Ventilation durch meridional alternierende zonale Strömungsbänder (LAZJs).

In dieser konzeptuellen Studie wird mithilfe eines Flachwassermodells mit 1.5 Schichten, gekoppelt an ein Advektions-Diffusions-Modell, der Einfluss der LAZJs auf die Ventilation der ETNA OMZ untersucht. Durch einen annual oszillierenden Antrieb werden in einem rechteckigen und in einem Becken mit atlantischer Geometrie Rossbywellen erzeugt, welche abseits des Äquators westwärts propagieren und schließlich in nichtlineare Wirbel aufbrechen. Der dafür verantwortliche Instabilitätsmechanismus auf Grundlage der Interaktion dreier nichtlinearer Rossbywellen bestimmt dabei die Stärke und Größe der resultierenden Wirbel, welche im zeitlichen Mittel Strukuren ähnlich den LAZJs rektifizieren. Ein Sauerstoff imitierender Tracer wird durch das angeregte Strömungsfeld transportiert, wobei eine Region mit lokal minimalen Konzentrationen erzeugt wird, deren Lage mit der der ETNA OMZ grundlegend übereinstimmt. Das mit der Schichtdicke gewichtete Tracerbudget zeigt, dass die Eulersche mittlere advektive Flusskonvergenz deutlich wichtiger als die wirbelgetriebene advektive Flusskonvergenz ist, um die stark vereinfachte Zehrung des Tracers zu balancieren. Aus dem Mitteln der advektiven Flusskonvergenz resultiert außerdem ein Wirbelvermischungsterm, der ebenfalls eine wichtige Rolle im Tracerbudget spielt. Dieser Term wird näher analysiert. Trotz des Antriebs mit rein annualer Periode wird interannuale bis dekadische und längere Variabilität im Tracerfeld erzeugt, selbst in der Region der ETNA OMZ. Der Vergleich zwischen modellierten und beobachteten Sauertstofftrends führt nicht zu einer Zurückweisung der Nullhypothese, dass die

beobachteten dekadischen Trends in der tiefen OMZ Teil der intrinsischen Variabilität des Systems sind. Hingegen wird die starke dekadische Abnahme an Sauerstoff in der oberen OMZ zwischen 2006-2013 nicht vom Model reproduziert. Auf multidekadischen Zeitskalen ist das Bild umgekehrt. Im Gegensatz zur oberen OMZ wird die multidekadische Abnahme an Sauerstoff in der tiefen OMZ nicht vom Model reproduziert. Während dies auf einen anthropogen getriebenen Sauerstoffentzug der tiefen OMZ hindeutet, ist es wichtig die Idealisierung und Einfachheit des Modells zu berücksichtigen. Zusätzlich erschweren große Lücken in Sauerstoffkonzentrationsmessreihen vor dem kürzlich intensivierten Messprogamm die verlässliche Bestimmung von multidekadischen Trends.

Contents

List of Figures

List of Tables

Chapter 1
Introduction

1.1 The oxygen minimum zone in the eastern tropical North Atlantic

The term "oxygen minimum zones" (OMZs) describes large areas in the open ocean subject to permanent hypoxia (*Helly and Levin*, 2004). The largest and strongest OMZs are found at intermediate depth (∼400 m) in the northern Indian Ocean and on the eastern side of the (sub-) tropical North and South Pacific (ETNP, ETSP) (*Paulmier and Ruiz-Pino*, 2009), with partly "suboxic" conditions of oxygen (O_2) concentrations below 10 μmol kg^{-1} (Fig. 1.1a). The OMZs in the eastern (sub-) tropical North and South Atlantic (ETNA, ETSA) are marked by somewhat milder "hypoxic" conditions of oxygen concentrations below 60 μmol kg^{-1} to 120 μmol kg^{-1} (e.g. *Karstensen et al.* (2008)). The existence of the OMZs is attributed to the interplay of biological and physical processes. Enhanced primary productivity at the sea surface fostered by open ocean and coastal upwelling leads to an increased export of organic material to the ocean interior. The re-mineralization of the sinking material consumes oxygen and thus acts as an oxygen sink (*Wyrtki*, 1962). At the same time, the (sub-) tropical eastern Atlantic and Pacific lie within the "shadow zones" predicted by the classical theory of the ventilated thermocline (*Luyten et al.*, 1983). These areas are characterized by a sluggish horizontal circulation and are hence subject to little oxygen supply, i.e. a weak ventilation. *Stramma et al.* (2008a, 2010) observed both a horizontal and vertical expansion and intensification of the OMZs over decades, which is in line with

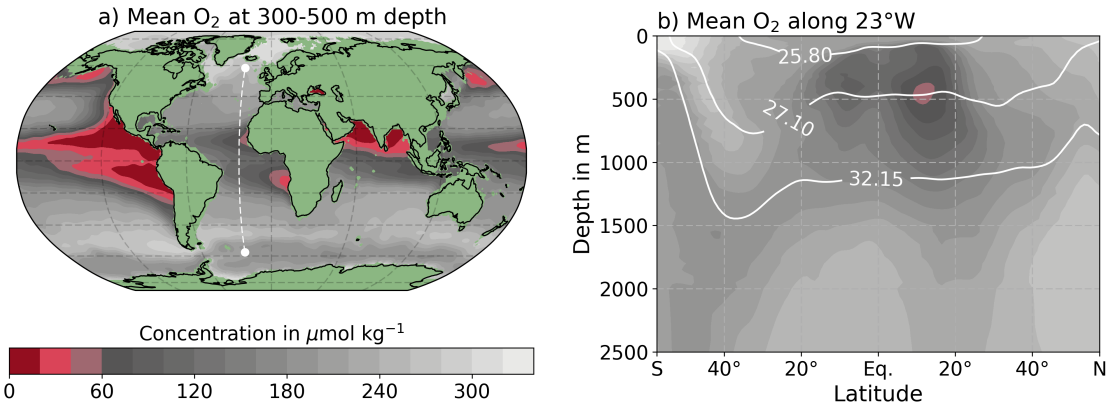

Figure 1.1: a) Distribution of mean oxygen content in the 300-500 m depth layer and b) along the 23 °W meridional section (highlighted by the white dashed line in a)) derived from the World Ocean Atlas 2013 (*Garcia et al.*, 2014). Oxygen concentrations were converted from ml l^{-1} to μmol kg^{-1} using a molar volume for oxygen of 22.392 l mol^{-1} and in-situ densities (*Hofmann et al.*, 2011). In b) the potential density surfaces $\sigma_0 = 25.8$, $\sigma_0 = 27.1$, and $\sigma_1 = 32.15\,kg\,m^{-3}$ are included. σ_0 and σ_1 thereby represent the potential density referenced to a reference pressure of 0 and 1000 dbar, respectively. These three isopycnals are considered to be the lower boundaries of the TSW, CW and AAIW (*Stramma et al.* (2005), abbreviations explained in Tab. 1.1). Density fields were calculated from the World Ocean Atlas 2013 temperature and salinity fields (*Locarnini et al.*, 2013; *Zweng et al.*, 2013).

an overall observed deoxygenation of the global ocean (*Keeling et al.*, 2010; *Schmidtko et al.*, 2017). The loss of oxygen is a key stressor on ecosystems, i.e. by changes in the biogeochemistry or loss of habitat, having strong effects on coastal economies depending on fisheries (*Diaz and Rosenberg*, 2008; *Vaquer-Sunyer and Duarte*, 2008; *Stramma et al.*, 2012a; *Breitburg et al.*, 2018). The question at hand is how much of the observed long-term variability in the OMZs is due to anthropogenic influences in relation with global climate change (list of references given in *Brandt et al.* (2015)), and how much can be attributed to internal variability of the ocean and climate system acting on seasonal to multidecadal time scales.

The ETNA OMZ is located off the north-west African continent with its north-western boundary marked by the south-westward flowing North Equatorial Current (NEC), and the southern boundary by the equatorial zonal current band system, with the North Equatorial Countercurrent (NECC)/North Equatorial Undercurrent

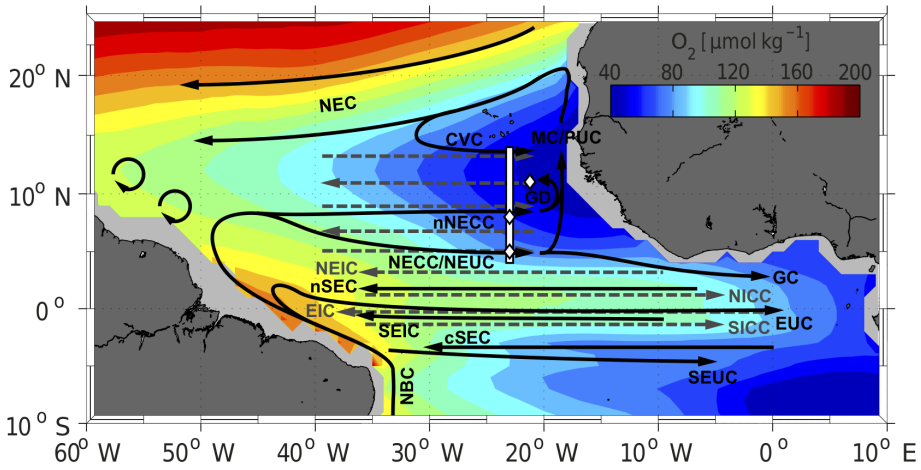

Figure 1.2: Mean oxygen distribution at the 27.1 kg m^{-3} potential density surface obtained from the MIMOC climatology (*Schmidtko et al.*, 2013, 2017) with a conceptual view of the mean flow field in the tropical Atlantic and ETNA OMZ superimposed (adapted from *Brandt et al.* (2015); *Pena-Izquierdo et al.* (2015)). The black solid arrows denote mean surface and thermocline currents in the upper 300 m, while the dashed grey lines represent the currents found at intermediate depth. The white line shows the location of the 23 °W section from 4 °-14 °N and the diamonds show the locations of multi-year moorings. See Tab. 1.1 for the name abbreviations of the individual currents. This figure is taken from *Hahn et al.* (2017).

(NEUC) as the northernmost current band, at ∼5 °N (Fig. 1.2). Along the African coast the Mauritania Current (MC) transports water poleward (*Stramma et al.*, 2008b). The most distinct circulatory feature in the otherwise sluggish ETNA OMZ is the eastward flowing northern branch of the NECC (nNECC) at 8 °-10 °N, which reaches the southern flank of the Guinea Dome (GD) associated with isopycnal doming in the central water layer and enhanced open ocean upwelling south of the Cape Verde Islands (*Stramma et al.*, 2005). Below the surface intensified NECC and the surface expression of the nNECC, the NEUC and the nNECC are part of the so-called latitudinally alternating zonal jets (LAZJs), which extend from the near surface to at least 1000 m depth, and which play a major role in supplying oxygen from the oxygen enriched western part of the subtropical Atlantic to the OMZ (*Hahn et al.*, 2017). The flow field in the ETNA OMZ is further coupled with equatorial dynamics through the generation of (coastal) Kelvin and (off-) equatorial Rossby waves. On the equator,

the variability is marked by a strong annual and semi-annual cycle, which is linked to basin-mode resonance of the fourth and second baroclinic mode, respectively (*Cane and Moore*, 1981; *Brandt et al.*, 2016).

The ETNA OMZ is made up of two local minima of oxygen concentration (Fig. 1.1b). The shallow oxygen minimum zone is found at around 100 m depth, i.e. in the Central Water (CW) layer, while oxygen concentrations drop to even lower values at $400-500$ m in the deep OMZ, which is at the boundary between the CW and Antarctic Intermediate Water (AAIW) (*Karstensen et al.*, 2008). More or less regular and continuous in-situ observational records are present since 1999 (*Brandt et al.*, 2010), cutting through the ETNA OMZ along the latitudinal 23 °W section (Fig. 1.1b). In connection with historical data mostly from the 1970s and 80s this dataset allows for attempts to quantify oxygen variability on decadal to multidecadal time scales. *Stramma et al.* (2008a) estimated a decrease in the ETNA OMZ oxygen content by $0.34 \pm 0.13\,\mu\text{mol}\,\text{kg}^{-1}\,\text{yr}^{-1}$ from 1960 onwards. In a more detailed analysis *Brandt et al.* (2015) detected different negative trends for the upper and lower OMZ in the period from 1900-2013, of $-0.8 \pm 0.5\,\mu\text{mol}\,\text{kg}^{-1}$ per decade and $-1.8 \pm 0.3\,\mu\text{mol}\,\text{kg}^{-1}$ per decade, respectively (Fig. 1.3). However, on a shorter time scale from 2006-2013, the trend was much stronger in the upper OMZ with $-14.3 \pm 6.9\,\mu\text{mol}\,\text{kg}^{-1}$ per decade but reversed in the lower OMZ to $2.7 \pm 1.9\,\mu\text{mol}\,\text{kg}^{-1}$ per decade. These results suggest shorter term variability imposed on the long-term decrease of oxygen in the OMZ. *Hahn et al.* (2014) show that the time scales of processes driving the variance in moored time series cover a wide range. Calculating a budget for the ETNA OMZ, *Hahn et al.* (2017) pick up the hypothesis of *Brandt et al.* (2010) that the observed changes are most likely linked to the zonal advection of oxygen and connect the recent oxygen increase in the deep OMZ with an intensification of the LAZJ. In their study, *Stramma et al.* (2012b) try to compare observed oxygen trends to simulated oceanic oxygen fields from Earth Systems Models. Despite an overall agreement in the distribution and trend, the regional patterns carry a lack in realism, complicating the identification

of responsible mechanisms. *Duteil et al.* (2014) find that the OMZ is modelled more realistically if the resolution of models is increased from 0.5 ° to 0.1 °, which is much higher than the horizontal resolution in *Stramma et al.* (2012b). The authors claim that LAZJs are crucial in setting the oxygen concentration in the OMZ. Hence, the persistent inability of models to accurately represent the LAZJs makes the identification of the mechanisms behind the observed variability in the OMZ's extent and intensity almost impossible. The study of *Duteil et al.* (2014) implies that an accurate representation of the mesoscale eddy field is of vital importance in understanding the dynamics behind the OMZ ventilation.

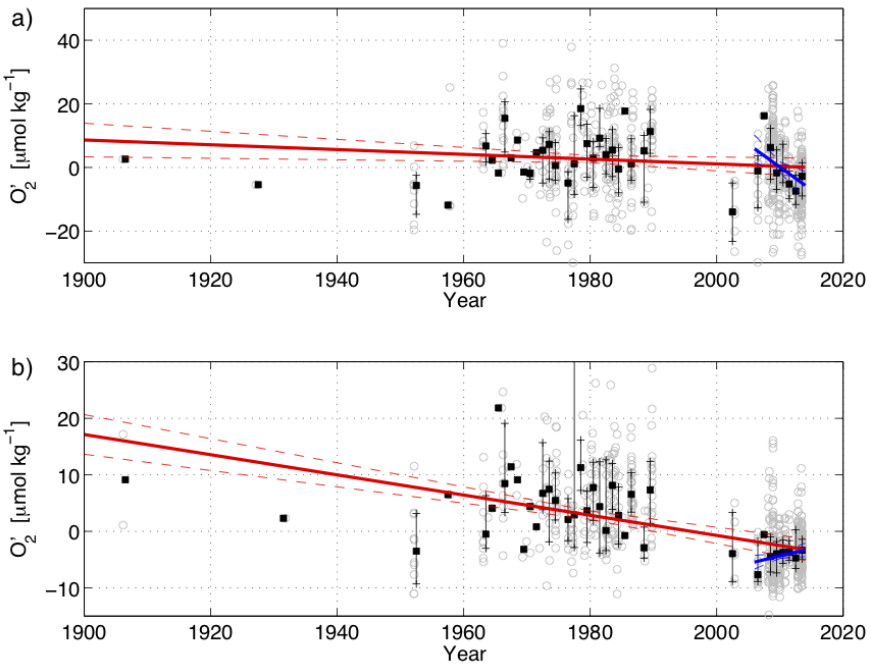

Figure 1.3: Oxygen anomalies for the region 9−15 °N, 20−26 °W and 150 − 300 m (intermediate oxygen maximum, upper panel) and 350−700 m (deep oxygen minimum, lower panel). Grey circles represent all available data, whiskers show interquartile range of data within each year and the black squares annual medians. Trends are calculated using annual medians weighted by the square root of available data within each year for the period 1900 − 2013 (solid red line) and 2006 − 2013 (solid blue line). The dashed lines mark the standard errors of the trends. Taken from *Brandt et al.* (2015).

Table 1.1: Abbreviations used in this study including the acronyms of current names in Fig. 1.2.

Abbreviation	Name/Meaning
AAIW	Antarctic Intermediate Water
AMM	Atlantic Meridional Mode
AZM	Atlantic Zonal Mode
CVC	Cape Verde Current
CW	Central Water
EIC	Equatorial Intermediate Current
ETNA	Eastern Tropical North Atlantic
ETNP	Eastern Tropical North Pacific
ETSA	Eastern Tropical South Atlantic
ETSP	Eastern Tropical South Pacific
EUC	Equatorial Undercurrent
GC	Guinea Current
GD	Guinea Dome
LAZJ	Latitudinally alternating zonal jets
MC	Mauritania Current
NACW	North Atlantic Central Water
NBC	North Brazil Current
NEC	North Equatorial Current
NECC	North Equatorial Countercurrent
nNECC	northern North Equatorial Countercurrent
NICC	North Intermediate Counter Current
NEIC	North Equatorial Intermediate Current
NEUC	North Equatorial Undercurrent
OMZ	Oxygen Minimum Zone
PUC	Poleward Undercurrent
SACW	South Atlantic Central Water
SEIC	South Equatorial Intermediate Current
cSEC	central South Equatorial Current
nSEC	northern South Equatorial Current
SEUC	South Equatorial Under Current
SICC	South Intermediate Counter Current
TSW	Tropical Surface Water

1.2 Geostrophic turbulence and zonal jets

Non-linear dynamics in two-dimensional or stably stratified flows in a rotating framework are referred to as geostrophic turbulence, for which the quasi-geostrophic equations form the dynamical basis (*Salmon*, 1982). Through these dynamics the large scale oceanic and atmospheric circulation is enriched by eddying features and other non-linear mesoscale components. In quasi-geostrophic flows the kinetic energy spectrum exhibits a K^{-3} law (where K is the total wavenumber) (*Charney*, 1971), which is associated with a "forward cascade" of potential enstrophy (i.e. potential vorticity squared), hence a transfer to smaller scales, while energy is transferred to larger scales, referred to as the "inverse energy cascade". *Rhines* (1975) analysed the evolution of a turbulent two dimensional flow field under the effect of the variation of the Coriolis parameter with latitude, the so-called β-effect. The study showed that the β-effect adds an upper threshold for the up-scale energy transfer. *Rhines* (1975) argues that in the limit of low frequencies the flow has to become anisotropic (favouring north-south wave numbers) in order to fulfil the Rossby wave dispersion relation. The author finds out that the end-state of an evolving eddy field on a β-plane is marked by zonally elongated eddies with a meridional length scale corresponding to the so-called Rhines scale (see Section 2.3.4 for definition). The zonal jets found in the atmosphere of Earth or Jupiter are found to be governed by these dynamics (*Galperin et al.*, 2004). As they are visible in the instantaneous flow field these jets are referred to as being "manifest" (*Berloff et al.*, 2011).

In contrast to the periodic domain to which the considerations of *Rhines* (1975) apply, the oceans are confined by lateral boundaries for which, in an idealised setting, the flow field is found to be isotropic, hence without systematically elongated eddies (*LaCasce*, 2002). Still, the observation of zonal jets in Earth's global ocean as the manifestation of the dynamical concept developed by *Rhines* (1975) would be exciting (*Schlax and Chelton*, 2008). As Earth's global ocean is filled with strong (non-linear)

eddies (*Chelton et al.*, 2011), the possible existence of these zonal jets is however masked, hence complicating their detection. Observational evidence of oceanic latitudinally alternating elongated zonal current bands was first provided by *Maximenko et al.* (2005, 2008). In their studies, the existence of the jets was shown by temporal averaging of surface dynamic topography fields derived from satellite altimetry over long time scales and spatial high-pass filtering of in-situ temperature measurements, respectively. *Maximenko et al.* (2008) carefully refer to the observed jet-like features as "striations", as the dynamics behind the patterns are not yet clear. *Berloff et al.* (2011) also claim that the name "jet" is somewhat imprecise as the zonal current bands are poorly visible in the instantaneous flow field. Hence, the oceanic jets are vested with the word "latent", highlighting that their associated flow amplitude (in the order of $1\,\mathrm{cm\,s^{-1}}$) is much weaker then the highly energetic flow features associated with mesoscale eddies. Other studies have found further observational evidence of striations or at least an anisotropic flow field in the global oceans using satellite altimetry (*Huang et al.*, 2007) or global observations of sea surface temperatures (SST) (*Buckingham et al.*, 2014). Further studies claim the detection of zonal jets in various regions of the global ocean (*Melnichenko et al.*, 2010; *Van Sebille et al.*, 2011; *Ivanov et al.*, 2012; *Belmadani et al.*, 2017). The deployment of autonomously measuring float systems enabled the detection of latitudinally alternating zonal current bands also at intermediate depth in the tropical oceans (*Ollitrault et al.*, 2006; *Cravatte et al.*, 2012) and the global ocean (*Ollitrault and Colin de Verdière*, 2014).

Despite the frequent observation, there is still debate about the realism of the jets, found by long-term averaging of dynamical fields. *Schlax and Chelton* (2008) claim that zonal jets can also be rectified by randomly zonally propagating Gaussian eddies. They question the assumption by *Maximenko et al.* (2005) that the zonal velocity fields from randomly distributed eddies average to zero (see Fig. 3 in *Ivanov et al.* (2012) and *Chen et al.* (2016) for a visualization of the argument). This argument was partially supported by *Chen et al.* (2015). However, *Buckingham and Cornillon*

(2013) find an inconsistency between the *Schlax and Chelton* (2008) hypothesis and the time mean striations. According to *Buckingham and Cornillon* (2013), not all of the striation patterns can be attributed to the zonal propagation of eddies, as in the observed ocean eddy field the mean and standard deviation of the zonal velocity do not decline as rapidly with increasing averaging period, as described by *Schlax and Chelton* (2008).

The dynamics behind the zonal jets are subject of current research (e.g. *Kamenkovich et al.* (2009a)) mainly using ocean models. Simplified two-layer models (*Panetta*, 1993) or ocean general circulation models (*Nakano and Hasumi*, 2005) had already revealed similar patterns before the observation of the "latent" zonal jets. So far, a wide variety of mechanisms has been proposed to be responsible for the jet formation, ranging from the potential vorticity (PV) staircase (*Baldwin et al.*, 2007; *Dritschel and McIntyre*, 2008), over primary and secondary instability mechanisms in the ocean interior (*Pedlosky*, 1975; *Berloff et al.*, 2009), to radiating instabilities from the eastern boundary (*Hristova et al.*, 2008; *Wang et al.*, 2012) where stationary jets are found in connection with permanent meanders in boundary currents (*Centurioni et al.*, 2008). Related to this mechanism, *Afanasyev et al.* (2011) and *Davis et al.* (2014) suggested a mechanism based on the spreading of vorticity anomalies from the eastern boundary into the basin interior, known as β-plumes. *LaCasce and Pedlosky* (2004) and *O'Reilly et al.* (2012) demonstrated the potential of long baroclinically unstable Rossby waves to introduce the zonal jets whose locations are time variant. Building on this idea, *Marshall et al.* (2013) introduced the concept of Rossby rip currents, in which Eulerian mean eastward current bands are formed to balance the westward mass transport through Stokes drift associated with baroclinic Rossby waves and eddies, in analogy to rip currents found close to beaches. The most relevant suggested generation mechanism related to our study is the non-linear Rossby wave triad interaction, which has been suggested to be responsible for the LAZJs found in the Pacific (*Qiu et al.*, 2013a).

The existence of zonal jets is shown to have an influence on the material transport within the oceans (*Kamenkovich et al.*, 2009b; *Chen and Flierl*, 2015). The introduced anisotropy in the lateral tracer transport (*Kamenkovich et al.*, 2015) has hence some implications for the ventilation mechanism of the ETNA OMZ, for which the LAZJs are observed to be a prominent feature. The analysis of the zonal jets and their link to the ventilation of the OMZ will be the subject of this study.

1.3 Research questions

The aim of this study is to establish a simple dynamical understanding of the ventilation of the ETNA OMZ through lateral tracer advection in a geostrophically turbulent field. Therefore, a simple reduced gravity model is set up, representing the first baroclinic mode in the region of interest. Under annual period forcing a turbulent flow field is excited, which transports a tracer through the basin. In a model run with Atlantic basin geometry, a more or less realistic region of minimum tracer is established in the region of the ETNA OMZ. The questions that are tackled in this study are hence:

1. How do the tracer and dynamical fields behave under annual period forcing at the equator? What are the mechanisms behind the zonal jet generation in the 1.5 layer shallow water model?

2. How does the ventilation of the ETNA OMZ function in a non-linear 1.5 layer reduced-gravity model?

3. What is the interannual to multidecadal variability of the zonal jets and the associated tracer field and how does this compare to observed trends in the real ocean?

The study is structured as follows: Chapter 2 contains a description of the used model and the experiment set up. Furthermore, analytical tools and dynamical concepts

are introduced. In Chapter 3, the analysis of the model output with respect to the questions stated above is presented. Chapter 4 subsequently yields a discussion of the results, in which the findings are further analysed and compared to existing literature. In Chapter 5 the main findings of the study are summarised and a brief outlook with further suggestions to study the ventilation of OMZs by zonal jets is given. The Appendix contains further details concerning the model code.

Chapter 2
Data and Methods

In the first part of this chapter (Section 2.1) the employed non-linear shallow water model, written by Prof. Dr. Martin Claus[1], is introduced (the implementation of the model is explained in more detail in the Appendix A.1). In Section 2.2, the experiment configurations are explained, while in Section 2.3 the methods to analyse the model output are introduced. Furthermore, some dynamical concepts are introduced in this third part of the chapter. The main variables appearing in this chapter are also listed in Table A.1. Notation and symbols are summarised in Table A.2.

2.1 The non-linear shallow water model

2.1.1 The 1.5 layer shallow water model

The 1.5 layer shallow water model (cf. Chapter 6 in *Gill* (1982)) consists of two stacked density layers. The upper active layer has a uniform density $\rho = \rho_0$ and an undisturbed layer thickness H, while the underlying layer with higher density $\rho_0 + \Delta\rho$ is infinitely deep and at rest (Fig. 2.1). The interface displacement η between both layers is measured positively downwards, while the surface displacement ξ is measured positively upwards. The disturbed layer thickness is hence defined as $h = H + \eta + \xi$. The effective gravitational acceleration between two fluid layers is termed reduced gravity and can be expressed as $g' = g(\Delta\rho/\rho_0)$, where g is the acceleration due to gravity. As the density difference between the two layers is taken to be much smaller

[1]Prof. Dr. Martin Claus is affiliated with the University Kiel, Germany and GEOMAR Helmholtz Centre for Ocean Research Kiel, Germany, mclaus@geomar.de

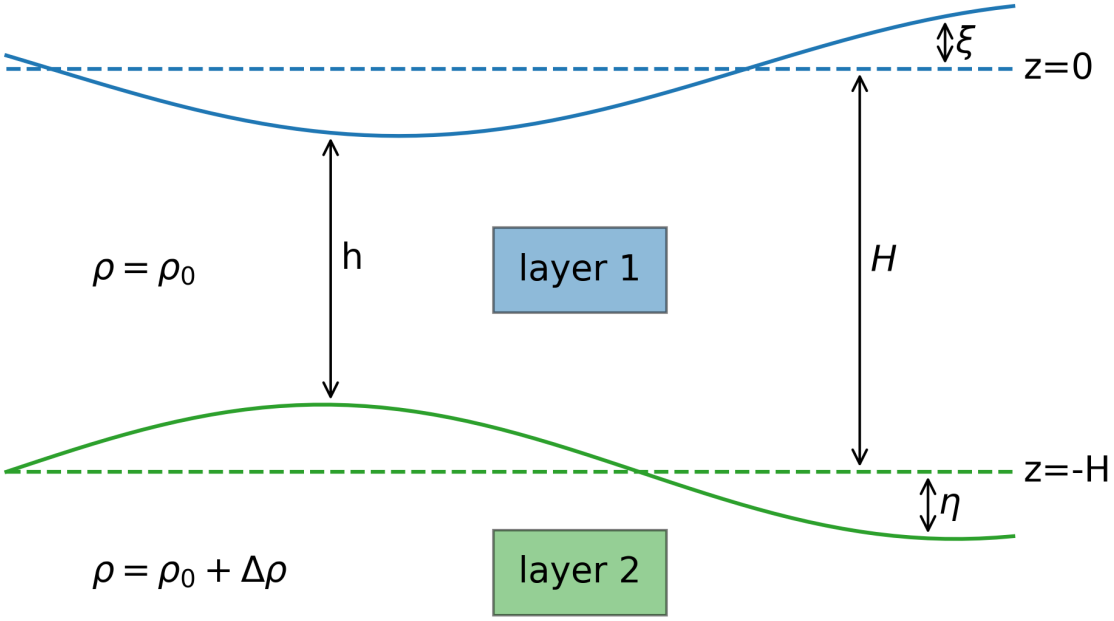

Figure 2.1: The 1.5 layer set-up of the shallow water model with an upper active layer over an infinitely deep lower layer at rest.

than between the upper layer and the overlying air, the resulting restoring force is much stronger for the surface than for the interface between the upper and lower layer. Hence by making the so-called "rigid lid" approximation, it is assumed that $h = H + \eta$ as $\xi \ll \eta$. The 1.5 layer model represents a single baroclinic mode.

2.1.2 The non-linear shallow water equations

The vertically uniform zonal and meridional velocities in the upper layer are given by u and v. Together with the interface displacement η they constitute the prognostic variables in the shallow water system. In spherical coordinates the governing non-linear

shallow water equations are

$$\frac{\partial u}{\partial t} + \frac{u}{r\cos\vartheta}\frac{\partial u}{\partial \lambda} + \frac{v}{r}\frac{\partial u}{\partial \vartheta} - \frac{uv\tan\vartheta}{r} - fv = -g'\frac{1}{r\cos\vartheta}\frac{\partial \eta}{\partial \lambda} + M_u + F_u \tag{2.1a}$$

$$\frac{\partial v}{\partial t} + \frac{u}{r\cos\vartheta}\frac{\partial v}{\partial \lambda} + \frac{v}{r}\frac{\partial v}{\partial \vartheta} + \frac{u^2\tan\vartheta}{r} + fu = -g'\frac{1}{r}\frac{\partial \eta}{\partial \vartheta} + M_v + F_v \tag{2.1b}$$

$$\frac{\partial \eta}{\partial t} + \frac{1}{r\cos\vartheta}\frac{\partial (hu)}{\partial \lambda} + \frac{1}{r\cos\vartheta}\frac{\partial (hv\cos\vartheta)}{\partial \vartheta} = F_\eta, \tag{2.1c}$$

where (λ, ϑ) are longitude and latitude respectively, t is time, r is Earth's radius and

$$f = 2\Omega\sin\vartheta \tag{2.2}$$

is the Coriolis parameter dependent on latitude, with Ω being Earth's angular velocity. The zonal and meridional momentum equations (2.1a, 2.1b) carry the lateral momentum mixing terms M_u and M_v and the zonal and meridional momentum forcing terms F_u and F_v, respectively. The forcing term F_η in the continuity equation (2.1c) represents a mass source or sink to the active layer.

Introducing the potential vorticity $q = (f + \zeta)/h$, where

$$\zeta = \frac{1}{r\cos\vartheta}\left(\frac{\partial v}{\partial \lambda} - \frac{\partial u\cos\vartheta}{\partial \vartheta}\right) \tag{2.3}$$

is the relative vorticity, and defining $E = (u^2 + v^2)/2 + g'\eta$ as the energy density or Bernoulli potential, consisting of the sum of kinetic and available potential energy, the equation system can be rewritten as

$$\frac{\partial u}{\partial t} = qhv - \frac{1}{r\cos\vartheta}\frac{\partial E}{\partial \lambda} + M_u + F_u \tag{2.4a}$$

$$\frac{\partial v}{\partial t} = -qhu - \frac{1}{r}\frac{\partial E}{\partial \vartheta} + M_v + F_v \tag{2.4b}$$

$$\frac{\partial \eta}{\partial t} = -\frac{1}{r\cos\vartheta}\left(\frac{\partial (hu)}{\partial \lambda} + \frac{\partial (hv\cos\vartheta)}{\partial \vartheta}\right) + F_\eta \tag{2.4c}$$

The zonal and meridional momentum mixing terms are formulated as

$$M_u = -\frac{1}{r\cos\vartheta}\frac{\partial}{\partial\lambda}P_{\lambda\lambda} - \frac{1}{r}\frac{\partial}{\partial\vartheta}P_{\lambda\vartheta} + \frac{2\tan\vartheta}{r}P_{\lambda\vartheta} \tag{2.5a}$$

$$M_v = -\frac{1}{r\cos\vartheta}\frac{\partial}{\partial\lambda}P_{\lambda\vartheta} - \frac{1}{r}\frac{\partial}{\partial\vartheta}P_{\vartheta\vartheta} - \frac{\tan\vartheta}{r}\left(P_{\lambda\lambda} - P_{\vartheta\vartheta}\right) \tag{2.5b}$$

with the symmetric momentum flux density tensor $\mathbf{P}$ (*Shchepetkin and O'Brien*, 1996). Its viscous components are given by

$$P_{\lambda\lambda} = -A_h h\left(\frac{1}{r\cos\vartheta}\frac{\partial}{\partial\lambda}u - \frac{1}{r}\frac{\partial}{\partial\vartheta}v - \frac{\tan\vartheta}{r}v\right) \tag{2.6a}$$

$$P_{\vartheta\vartheta} = -P_{\lambda\lambda} \tag{2.6b}$$

$$P_{\lambda\vartheta} = P_{\vartheta\lambda} = -A_h h\left(\frac{1}{r\cos\vartheta}\frac{\partial}{\partial\lambda}v - \frac{1}{r}\frac{\partial}{\partial\vartheta}u + \frac{\tan\vartheta}{r}u\right) \tag{2.6c}$$

with the constant and uniform lateral eddy viscosity A_h.

2.1.3 The tracer equation

The shallow water model is coupled to an advection-diffusion model in which the tracer is advected by the flow field diagnosed by the shallow water model. The tracer is thereby set to mimic oxygen. The analytical model equation is similar to the advection-diffusion model used in the study of equatorial oxygen variability by *Brandt et al.* (2012):

$$\underbrace{\frac{\partial(Ch)}{\partial t}}_{1} + \underbrace{\nabla\cdot(Ch\mathbf{u})}_{2} = \underbrace{\nabla\cdot(\kappa_h h\nabla C)}_{3} - \underbrace{JCh}_{4} - \underbrace{h\gamma(C-C_0)}_{5} + \underbrace{CF_\eta}_{6} \tag{2.7}$$

where κ_h is the lateral diffusivity of the tracer C, J is the biological consumption rate, and $1/\gamma$ represents the time scale of a relaxation towards a specified tracer distribution field C_0. Thus the equation contains the tendency term (1), advection (2), lateral diffusion (3), strongly simplified biological consumption as a tracer sink (4), relaxation

as a tracer source (5), and a term related to the forcing (6). The latter term is only needed if the shallow water model is forced in the continuity equation, i.e. via F_η, adding or subtracting mass and consequently tracer from the active layer.

For the shallow water model used in this study, equations 2.4a-2.4c are implemented on the Arakawa-C grid (*Arakawa*, 1972) (Appendix A.1.1). The implementation of the lateral mixing term using the scheme of *Shchepetkin and O'Brien* (1996) is explained in the Appendix A.1.2, while the Appendix A.1.4 explains the implementation of the tracer equation in more detail. The model is finally integrated using the Adams-Bashforth 3^{rd} order time stepping scheme (Appendix A.1.3).

2.2 Experiment model configurations

The model domain is located on a sphere with a radius of $r = 6371\,\text{km}$., i.e. simulating Earth, and spans a latitudinal range from 20 °S to 50 °N and a longitudinal range from 65 °W to 15 °E, hence mimicking a rectangular version of the (sub-)tropical Atlantic. The horizontal resolution is set to 0.1 °. The model is set-up with an undisturbed layer depth of $H = 500\,\text{m}$ and a reduced gravity of $g' = 1.5 \times 10^{-2}\,\text{m}\,\text{s}^{-2}$, fixing the gravity wave speed to $c = \sqrt{g'H} \approx 2.7\,\text{m}\,\text{s}^{-1}$, which is only slightly larger than the first baroclinic mode gravity wave phase speed in the subtropical Atlantic (*Chelton et al.*, 1998). Hence, the choice of the gravity wave speed configures the model to represent the first baroclinic mode. Earth's angular velocity Ω is set to $7.272\,205 \times 10^{-5}\,\text{rad}\,\text{s}^{-1}$, scaling the Coriolis parameter dependent on latitude (Eq. 2.2). Lateral eddy viscosity is set to $A_h = 100\,\text{m}^2\,\text{s}^{-1}$. The model is integrated using a no-slip boundary condition with a sufficiently small time step $\Delta t = 500\,\text{s}$ in order to fulfil the CFL-criterion (*Courant et al.*, 1928), given by $|\mathbf{u}\Delta t|/\Delta x < 1$, where Δx is the grid spacing and $\mathbf{u}$ is the horizontal velocity.

The model is run in two configurations. The first configuration contains no realistic coastlines and hence features a (pseudo-) rectangular ocean basin, while the second configuration is calculated with Atlantic Ocean coastlines with a 0.1 ° resolution[2]. Every ocean grid point is automatically associated with an undisturbed layer depth H, thus even in the configuration including coastlines, the real ocean bottom topography is neglected. In both configurations, the zonal and meridional boundaries are closed by setting the undisturbed layer depth $H = 0$ on the boundaries. To avoid numerical stability issues, the Strait of Gibraltar is closed in the Atlantic basin configuration. Even though the focus is on the study of the northern hemisphere basin, the domain is chosen to extend well south of the equator to allow for the free development of the equatorial dynamics, which would otherwise be hindered due to the imposed no-slip boundary condition. For both configurations the model is run for 400 yr, allowing for multiple decades of model output from a fully spun-up dynamical field and tracer distribution.

The forcing is given by an annually oscillating, zonally constant mass source/sink along the equator. Its meridional structure is based on an equatorial Kelvin wave, so that

$$F_\eta(\lambda, \vartheta) = \begin{cases} -\sin(\omega_{yr} t) A_0 \exp[-\beta y^2/(2c)] & \text{if } 15\,^\circ\text{S} \leq \vartheta \leq 15\,^\circ\text{N} \\ 0, & \text{otherwise} \end{cases} \tag{2.8}$$

where $A_0 = 3 \times 10^{-5}\ \text{m s}^{-1} \approx 2.6\ \text{m day}^{-1}$ is the forcing amplitude, y is the meridional distance from the equator and ω_{yr} is the annual frequency (Fig. 2.2). The meridional gradient of the Coriolis parameter is given by

$$\beta = \frac{1}{r}\frac{\partial f}{\partial \vartheta} = \frac{2\Omega}{r}\cos\vartheta \tag{2.9}$$

The forcing mechanism for the entire domain through the excitement and propagation

[2]The topographic dataset was retrieved from NASA Earth Observations (NEO) website `https://neo.sci.gsfc.nasa.gov/view.php?datasetId=SRTM_RAMP2_TOPO` on April 13, 2017.

of (equatorial) Kelvin and Rossby waves will be described in Section 3.1. It is similar to the approach taken by *Qiu et al.* (2013a), but instead of an explicit diabatic pumping or suction in the continuity equation, they employ a basin-wide wind forcing in the zonal momentum equations to generate the equatorial Kelvin and Rossby waves. The forcing used in our study will lead to a slight overall mean mass reduction of the upper layer, due to the cycle of initial reduction and subsequent replenishment of mass.

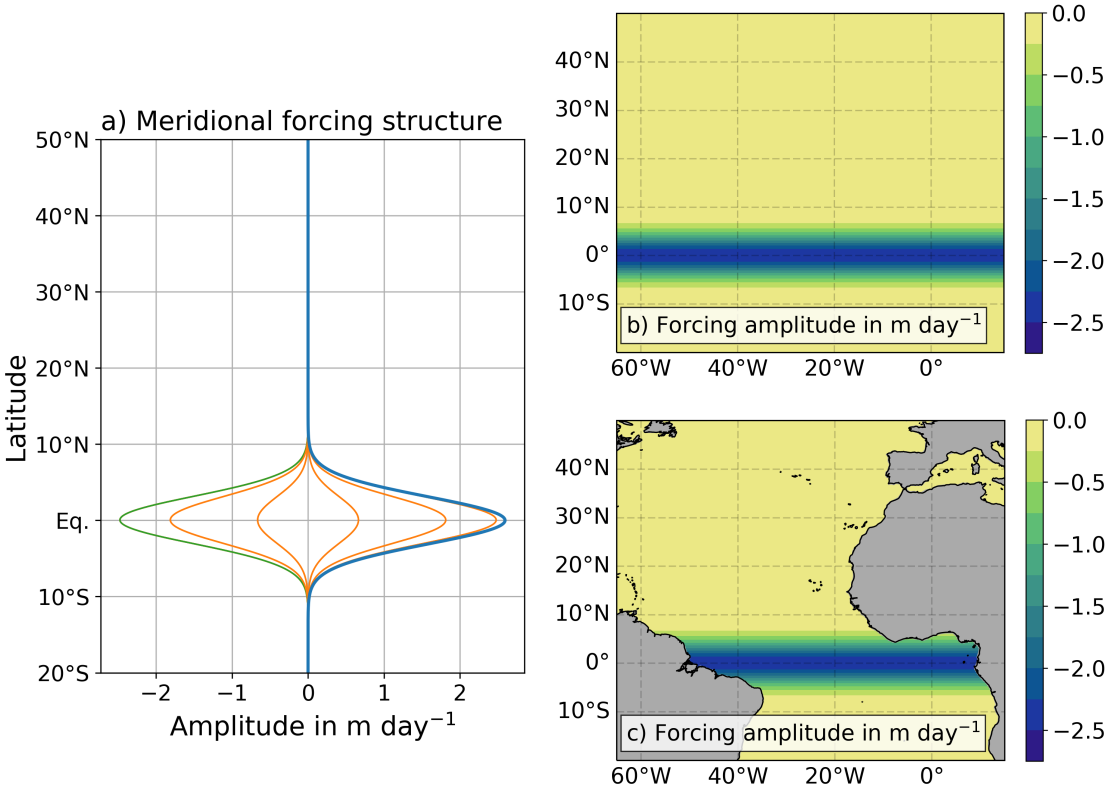

Figure 2.2: a) The meridional structure of the forcing F_η. The maximum forcing amplitude is given in blue. Monthly averages of the forcing term are given by the orange lines. The monthly average of March is represented by the green line, for which the forcing's spatial structure is shown in the rectangular basin (b) and in the Atlantic basin (c).

The tracer is restored to 1 along the western edge of the basin, acting as the tracer source. The source strength and location is defined by the two dimensional step

function C_0 with

$$C_0(\lambda,\vartheta) = \begin{cases} 1 & \text{if } 65\,^\circ W \leq \lambda \leq 55\,^\circ W \\ 0, & \text{otherwise} \end{cases} \tag{2.10}$$

To prevent a sharp edge in the tracer concentration at the step in the C_0 field, the restoring rate γ is set up to be spatially dependent with

$$\gamma(\lambda,\vartheta) = \begin{cases} \gamma_0/2\left(1-\tanh[\frac{\lambda-\lambda_0}{\lambda_s}]\right) & \text{if } 65\,^\circ W \leq \lambda \leq 55\,^\circ W \\ 0, & \text{otherwise} \end{cases} \tag{2.11}$$

where $\lambda_0 = 63\,^\circ$, $\lambda_s = 1\,^\circ$ and $\gamma_0 = 1/8.35$ day^{-1}, which corresponds to twice the restoring time scale used in (*Brandt et al.*, 2012), who analyse the impact of equatorial dynamics on tracer spreading using a similar tracer model as the one used here. They base the value of γ_0^{-1} on one hundredth of the Atlantic basin mode period. As the present study considers off-equatorial tracer spreading, the restoring time scale can be defined independently of the basin mode period and is thus set high to make sure that tracer is quickly supplied, yielding an "infinite" tracer source. The zonal structures of the latitudinally independent fields of C_0 and γ, are shown in Figure 2.3.

The tracer consumption rate is set to $J = 6.5 \times 10^{-10}$ s^{-1}, which hence features much longer time scales ($\sim$ 50 years) compared to the restoring term. The value is half the consumption rate diagnosed from fitting a one-dimensional advection-diffusion model to observations in the Pacific by *Van Geen et al.* (2006) and used in conceptual studies of the oxygen field in the equatorial Atlantic in *Brandt et al.* (2008, 2010, 2012). Next to ensuring that the tracer is able to cross the entire basin before being damped out, the weaker consumption chosen here further respects the general relationship of lower apparent oxygen utilization rates at greater depth (*Karstensen et al.*, 2008), considering that the zonal jet system observed in the global ocean exists down to at least $\sim$1000 m. The consumption acts in proportion to the instantaneous tracer concentration over the entire basin and eventually leads to a (quasi-) equilibrium

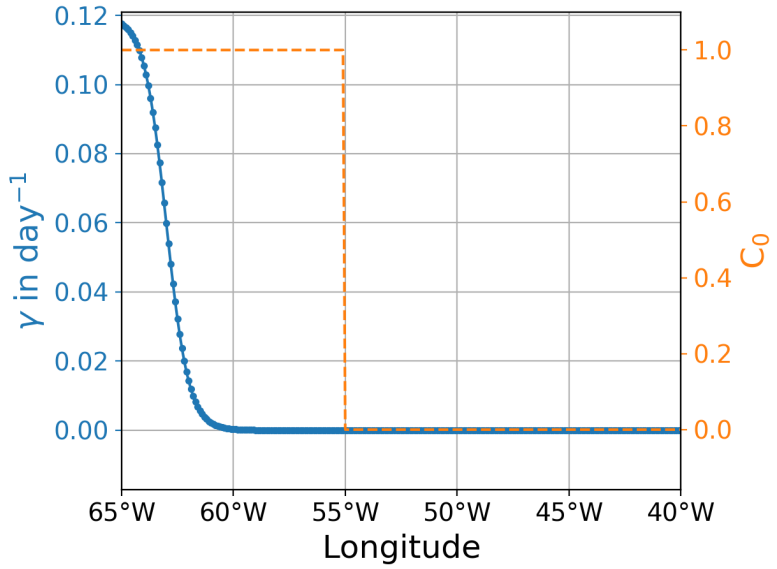

Figure 2.3: The structure of the restoring rate γ (blue) and the structure of the field C_0 (orange), which the tracer is restored to, for the western part of the basin.

between tracer source and sink. The lateral diffusivity of tracer is set to be identical with the lateral eddy viscosity, i.e. $\kappa_h = A_h$.

2.3 Analysing the model output

The model output is given in monthly averages and snapshots in monthly intervals. The following subsections will give a brief description of the analysis tools applied to the dataset.

2.3.1 Statistical analysis of the model output

Spatial Mean

For a spatial mean on a sphere the varying grid box area corresponding to every grid point has to be taken into account. The two dimensional spatial average of a variable

α is thus defined as

$$\langle \alpha \rangle^{\lambda\vartheta} = \frac{\sum_{i=1}^{N} \sum_{j=1}^{M} \alpha^{i,j} \cos \vartheta^{j}}{\sum_{i=1}^{N} \sum_{j=1}^{M} \cos \vartheta^{j}} \tag{2.12}$$

where N and M are the number of grid points in the zonal and meridional direction, respectively. Hence, the values of each grid point are weighted with the cosine of the corresponding latitude ϑ.

Temporal Mean

The temporal mean of the model output at a given grid point (defined by indices i, j) is given by

$$\overline{\alpha^{i,j}} = \frac{1}{K} \sum_{k=1}^{K} \alpha^{i,j} \tag{2.13}$$

where K is the number of time steps.

Thickness-weighted averaging

To differentiate between large-scale and eddying parts of the flow, it is common practice to use the Reynolds decomposition $\alpha = \overline{\alpha} + \alpha'$, where $\overline{\alpha}$ is the temporal mean, i.e. background state and α' is the superimposed fluctuation, i.e. eddying part of the variable α (*Gent et al.*, 1995). However, in a layered system it is more natural to use a thickness-weighted average (e.g. *Aiki and Greatbatch* (2012)). Therefore, the decomposition is performed as $\alpha = \hat{\alpha} + \alpha''$ where

$$\hat{\alpha} = \frac{\overline{\alpha h}}{\overline{h}} \tag{2.14}$$

is the thickness-weighted average and α'' is the corresponding deviation (*Greatbatch*, 1998). Corresponding to the Reynolds average, we have $\widehat{\alpha''} = 0$ and hence $\overline{h\alpha''} = 0$. If the variable α corresponds to a velocity, take here the horizontal velocity $\mathbf{u}$, the difference between the thickness-weighted average and the regular average is called

bolus velocity $\mathbf{u}^*$. Using definition 2.14, it follows

$$\begin{aligned} \mathbf{u}^* &= \hat{\mathbf{u}} - \overline{\mathbf{u}} \\ &= \frac{\overline{\mathbf{u}'h'}}{\overline{h}} \end{aligned} \tag{2.15}$$

which in the linear approximation corresponds to the Stokes drift velocity, stating the difference between the Eulerian and Lagrangian velocity (*Marshall et al.*, 2013). From definition 2.14, the following identity (*Favre*, 1965, 1983) can also be deduced

$$\begin{aligned} \overline{h\alpha_1\alpha_2} &= \overline{h\hat{\alpha}_1\hat{\alpha}_2} + \overline{h\hat{\alpha}_1\alpha_2''} + \overline{h\alpha_1''\hat{\alpha}_2} + \overline{h\alpha_1''\alpha_2''} \\ &= \overline{h}\hat{\alpha}_1\hat{\alpha}_2 + \hat{\alpha_1}\overline{h\alpha_2''} + \hat{\alpha_2}\overline{h\alpha_1''} + \overline{h\alpha_1''\alpha_2''} \\ &= \overline{h}\hat{\alpha}_1\hat{\alpha}_2 + \overline{h\alpha_1''\alpha_2''} \end{aligned} \tag{2.16}$$

which will be employed in the establishment of a tracer budget.

Standard deviation

The standard deviation σ of the model variable α at a given grid point is calculated as

$$\sigma(\alpha) = \sqrt{\frac{1}{K}\sum_{k=1}^{K}(\alpha^{i,j} - \overline{\alpha^{i,j}})^2}. \tag{2.17}$$

Thickness-weighted standard deviation

In the thickness-weighted framework, the standard deviation is calculated as

$$\hat{\sigma}(\alpha) = \sqrt{\frac{1}{K}\sum_{k=1}^{K}(\alpha^{i,j} - \widehat{\alpha^{i,j}})^2}. \tag{2.18}$$

2.3.2 Establishing the tracer budget

Thickness-averaging the tracer equation (2.7) yields

$$\frac{\partial\left(\hat{C}\bar{h}\right)}{\partial t} = -\nabla\cdot\left(\overline{Ch\mathbf{u}}\right) + \nabla\cdot\left(\overline{h\kappa_h\nabla C}\right) - J\hat{C}\bar{h} - \gamma\bar{h}\left(\hat{C}-C_0\right) + \overline{CF_\eta} \tag{2.19}$$

Using equation 2.16 to differentiate between the advective terms collected in the first term on the right hand side yields

$$\begin{aligned}\underbrace{\frac{\partial\left(\hat{C}\bar{h}\right)}{\partial t}}_{1} = \underbrace{-\nabla\cdot\left(\bar{h}\bar{\mathbf{u}}\hat{C}\right)}_{2}\underbrace{-\nabla\cdot\left(\bar{h}\bar{\mathbf{u}}^*\hat{C}\right)}_{3}\underbrace{-\nabla\cdot\left(\overline{h\mathbf{u}''C''}\right)}_{4}\\ \underbrace{+\nabla\cdot\left(\overline{h\kappa_h\nabla C}\right)}_{5}\underbrace{-J\hat{C}\bar{h}}_{6}\underbrace{-\gamma\bar{h}\left(\hat{C}-C_0\right)}_{7}\underbrace{+\overline{CF_\eta}}_{8}\end{aligned} \tag{2.20}$$

The terms (1), (5), (6), (7) and (8) correspond to the tendency, diffusive flux convergence, consumption, relaxation and forcing respectively. The tendency term does not necessarily vanish, as fluctuations on longer time scales than the averaging period might still contribute to the evolution of the tracer field. Term (2) in Equation 2.20 represents the Eulerian mean advective flux convergence, while term (3) is the eddy advective flux convergence. In the latter, tracer is advected with the bolus velocity $\mathbf{u}^*$. Term (4) in Equation 2.20 also constitutes a flux convergence and can have both, advective and diffusive characteristics. Its unclear nature has been subject to some analyses (e.g. *Greatbatch* (1998, 2001)). In this study, this term will be referred to as "eddy mixing term".

2.3.3 Estimating power spectral density

The estimation of power spectral density is used in the context of wavenumber spectra or frequency spectra to identify dominant wavelengths or periodicities in spatial or

temporal signals. The detrended input signal is transformed into frequency space using the discrete Fourier transform, which is a linear function,

$$\tilde{x}_k = \sum_{m=0}^{n-1} x_m \exp\left[-2\pi i \frac{mk}{n}\right] \qquad \text{with } k = 0, ..., n-1 \tag{2.21}$$

where x_m are the individual data points in the signal of length n, and $\tilde{x}_k$ are the complex Fourier transform components (*Oliphant*, 2006). A power spectrum estimate is obtained by multiplying the Fourier transform by its complex conjugate.

$$P(\tilde{x}_k) = \begin{cases} \frac{2}{n^2}|\tilde{x}_k|^2 & \text{for } k = 1, 2, ..., \frac{n}{2} - 1 \\ \frac{1}{n^2}|\tilde{x}_k|^2 & \text{for } k = 0 \quad \vee \quad k = n/2 \end{cases} \tag{2.22}$$

The factor 2 is due to the symmetry of the discrete Fourier transform for real input signals between positive and negative frequencies (*Press et al.*, 1992). The normalization factor n^{-2} is used to set the integral power of the Fourier transform equal to the mean squared amplitude of the input function, following Parseval's theorem. The corresponding frequencies are given by

$$f_k = \frac{k}{nS} \tag{2.23}$$

where S is the constant sampling interval.

2.3.4 Characteristic length scales

Rossby radius of deformation

The length scale at which rotational effects become as important for the evolution of the flow field as wave propagation is called the Rossby radius of deformation. It is defined via the ratio of the gravity wave speed and the Coriolis parameter (*Gill*, 1982)

and is hence given for the baroclinic configuration as

$$L_{\mathrm{Ro}} = \frac{(g'H)^{1/2}}{|f|} \tag{2.24}$$

Within a band of 5 ° of the equator, the equatorial Rossby radius of deformation is defined as

$$L_{\mathrm{Ro}_{eq}} = \left(\frac{c}{2\beta}\right)^{1/2} \tag{2.25}$$

because of the vanishing Coriolis parameter (*Gill*, 1982; *Chelton et al.*, 1998).

Rhines scale

Based on scale analysis, the Rhines scale is defined as (e.g. *Theiss* (2004); *Olbers et al.* (2012))

$$L_{\mathrm{Rh}} = \left(\frac{u_{\mathrm{rms}}}{\beta}\right)^{1/2} \tag{2.26}$$

where u_{rms} is the root mean square of the zonal eddy velocity. As there is no background zonal mean velocity imposed, u_{rms} is calculated at a fixed location over the time axis using the full zonal velocity u as

$$u_{\mathrm{rms}} = \sqrt{\frac{1}{N}\sum_{i=1}^{N} u_i^2} \tag{2.27}$$

The Rhines scale constitutes the boundary between motions in which either the transport of planetary or relative vorticity dominates. In turbulent flow fields with the characteristic horizontal length scale larger than the Rhines scale, Rossby wave dynamics introduce an anisotropy in the motions. In another definition, the Rhines scale is given as $\sqrt{2u_{\mathrm{rms}}/\beta}$ (e.g. *Eden* (2007)). However, as the definition is based on scale analysis, the inclusion of the factor of $\sqrt{2}$ is neglected in this study.

2.3.5 Resonant triad interaction

Based on non-linear dynamics, *Pedlosky* (1987) (Chapter 3.26) presents an instability mechanism invoking the interplay of three Rossby waves, i.e. a Rossby wave triad. The theory is developed for quasi-geostrophic flow on the β-plane, where the Coriolis frequency depends linearly on latitude, i.e. $f = f_0 + \beta y_d$, with y_d being the latitudinal distance from the centre latitude ϑ_0, at which f_0 and β are evaluated following Eq. 2.2 and 2.9. The triad instability concept (derived in Cartesian coordinates x, y) is based on the fact that a single Rossby wave

$$\psi \propto \cos(kx + ly - wt + \phi) \tag{2.28}$$

with streamfunction ψ, zonal and meridional wavenumber k and l, respectively, frequency ω and arbitrary phase angle ϕ is an exact solution to the unforced and non-viscous quasi-geostrophic potential vorticity equation

$$\frac{\partial}{\partial t}\left(\nabla^2\psi - \frac{f_0^2}{c^2}\psi\right) + J\left(\psi, \nabla^2\psi\right) + \beta\frac{\partial\psi}{\partial x} = 0 \tag{2.29}$$

with the Jacobian

$$J(A, B) = -\frac{\partial A}{\partial y}\frac{\partial B}{\partial x} + \frac{\partial A}{\partial x}\frac{\partial B}{\partial y} \tag{2.30}$$

and the streamfunction $\psi = g'\eta f_0^{-1}$ defined as such, so that

$$\frac{\partial\psi}{\partial x} = v \quad \text{and} \quad \frac{\partial\psi}{\partial y} = -u. \tag{2.31}$$

Any superposition of Rossby waves will however violate Equation 2.29. Expanding the streamfunction ψ in terms of the Rossby number $\epsilon \ll 1$, i.e.

$$\psi = \psi_0 + \epsilon\psi_1 + \epsilon^2\psi_2 + ..., \tag{2.32}$$

yields solutions of different orders for Equation 2.29. The $\mathcal{O}(1)$ quasi-geostrophic potential vorticity equation

$$\frac{\partial}{\partial t}\left(\nabla^2\psi_0 - \frac{f_0^2}{c^2}\psi_0\right) + \beta\frac{\partial\psi_0}{\partial x} = 0 \tag{2.33}$$

yields the linear dynamics and hence ψ_0 can be described as a superposition of linear Rossby waves with arbitrarily different amplitudes a

$$\psi_0 = \sum_j a_j \cos\theta_j \tag{2.34}$$

where $\theta_j = k_j x + l_j y - w_j t + \phi_j$. The non-linear interaction only becomes obvious in the $\mathcal{O}(\epsilon)$ equation

$$\frac{\partial}{\partial t}\left(\nabla^2\psi_1 - \frac{f_0^2}{c^2}\psi_1\right) + \beta\frac{\partial\psi_1}{\partial x} = \sum_m\sum_n \frac{a_m a_n}{2} B(K_m, K_n)[\cos(\theta_m + \theta_n) - \cos(\theta_m - \theta_n)] \tag{2.35}$$

where $B(K_m, K_n) = (K_m^2 - K_n^2)\,(k_m l_n - k_n l_m)$, with $K_m^2 = k_m^2 + l_m^2$ and $K_n^2 = k_n^2 + l_n^2$. Equation 2.35 is of a linear, forced nature, in which the interaction of any two waves produces a forcing term (i.e. the right hand side), as long as their wavelengths are different or their wave vectors are non-parallel. Under certain conditions, it is possible that the non-linear interaction of two waves leads to the forcing of a third Rossby wave, that can then develop into a linear, free oscillation. This process is called " resonant triad interaction", as the resonance of two waves leads to the growth in amplitude of a third wave. Taking an arbitrary set of three Rossby waves, the condition for this to happen is given by

$$k_1 + k_2 + k_3 = 0 \tag{2.36a}$$

$$l_1 + l_2 + l_3 = 0 \tag{2.36b}$$

$$\omega_1 + \omega_2 + \omega_3 = 0 \tag{2.36c}$$

If these conditions are fulfilled the time evolution of the wave amplitudes and hence the energy exchange between the waves is governed by

$$\frac{da_1}{dt} + \frac{B\left(K_2, K_3\right)}{K_1^2 + f_0^2 c^{-2}} a_2 a_3 = 0 \tag{2.37a}$$

$$\frac{da_2}{dt} + \frac{B\left(K_3, K_1\right)}{K_2^2 + f_0^2 c^{-2}} a_3 a_1 = 0 \tag{2.37b}$$

$$\frac{da_3}{dt} + \frac{B\left(K_1, K_2\right)}{K_3^2 + f_0^2 c^{-2}} a_1 a_2 = 0 \tag{2.37c}$$

during the time of interaction. Assuming the primary wave to be represented by a_2, K_2, etc., it is only possible for secondary waves to extract energy from the primary wave, if

$$K_1 < K_2 < K_3, \tag{2.38}$$

constrained by the conservation of energy and enstrophy. In this case, the exponential growth rate χ of the secondary waves is proportional to the amplitude of the primary wave and is given by (*Qiu et al.*, 2013a)

$$\chi = a_2 \left(\frac{B\left(K_2, K_3\right) B\left(K_1, K_2\right)}{\left(K_1^2 + f_0^2 c^{-2}\right)\left(K_3^2 + f_0^2 c^{-2}\right)} \right)^{1/2}. \tag{2.39}$$

The study of this triad instability mechanism is possible in an idealized set-up comparable to the rectangular basin used in this study. Following *Schopf et al.* (1981) the ray path of a westward propagating Rossby wave originating from a purely meridional boundary can be calculated analytically in Cartesian coordinates. A fundamental aspect of the ray tracing theory is the WKBJ (Wentzel-Kramers-Brillouin-Jeffreys) approximation, which relaxes the requirement of a constant Coriolis parameter from quasi-geostrophic theory (see Eq. 2.29) and thus allows for variations in f along the ray path. This step is justifiable by the argument that changes in f act over much larger spatial scales compared to the wavelengths considered here (*Schopf et al.*, 1981). Under the assumption of an equatorial β-plane ($f = \beta y_d$) and an initially vanishing

meridional wavenumber l, the path for a ray emanating from the initial meridional position y_0 at the eastern boundary ($x_0 = 0$), is hence given as

$$x(t) = -\frac{c}{2\omega}\left(1 - \frac{4\omega^2}{c^2}y_0^2\right)\Theta \tag{2.40}$$

$$y(t) = y_0 \cos\Theta \tag{2.41}$$

where $\Theta = -2\omega^2 t(kc)^{-1}$ and c is the gravity wave speed. The meridional wavenumber evolves over time t as $l(t) = \beta y_0 c^{-1} \sin\Theta$. Using the generated Rossby wave frequency $\omega = \omega_0$, one can infer the initial zonal wavenumber $k = k_0$ from the Rossby wave dispersion relation

$$\omega = \frac{-\beta k}{(k^2 + l^2 + f^2 c^{-2})} \tag{2.42}$$

Along the ray path the zonal wavenumber k and the frequency ω remain constant. Calculating the ray paths for a range of initial latitudes, the Rossby wave caustic becomes visible (Fig. 2.4a). All Rossby wave rays bend towards the equator, where the energy is bundled around a focal point (*Schopf et al.*, 1981; *Claus et al.*, 2014).

Following *Qiu et al.* (2013a) it is then possible to calculate at every location along the ray path the growth rate of all secondary waves (Fig. 2.4b) that fulfil the triad conditions (Eq. 2.36) and are able to extract energy from the primary wave (Eq. 2.38). If the growth rate becomes sufficiently large, the primary Rossby wave will break-up due to "non-linear triad instability".

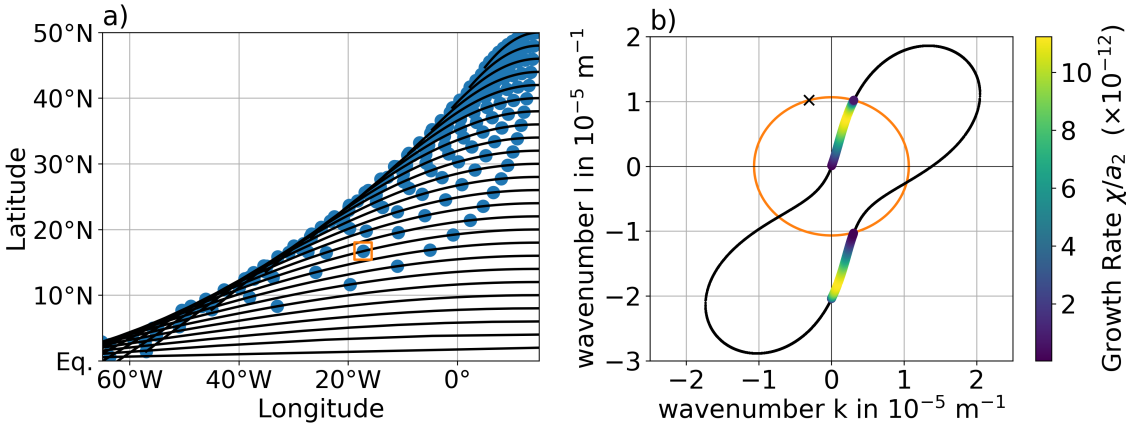

Figure 2.4: a) Ray paths (black lines) for Rossby waves emanating from the eastern boundary with initially vanishing meridional wavenumber on an equatorial β-plane. The blue dots show the annual progression of the waves along the path, forming the typical Rossby wave front in the meridional direction. b) Secondary waves in wavenumber space fulfilling the triad interaction criteria (Eq. 2.36) (black dots) at the location specified by the orange square in a). The black cross marks the zonal and meridional wavenumber of the primary wave, while the orange circle marks the corresponding absolute wavenumber. Growth rates of secondary waves that are able to extract energy from the primary wave (Eq. 2.38) normalized by the primary wave amplitude are given by coloured dots. This figure is following Figure 13 of *Qiu et al.* (2013a).

Chapter 3

Results

3.1 Model spin-up

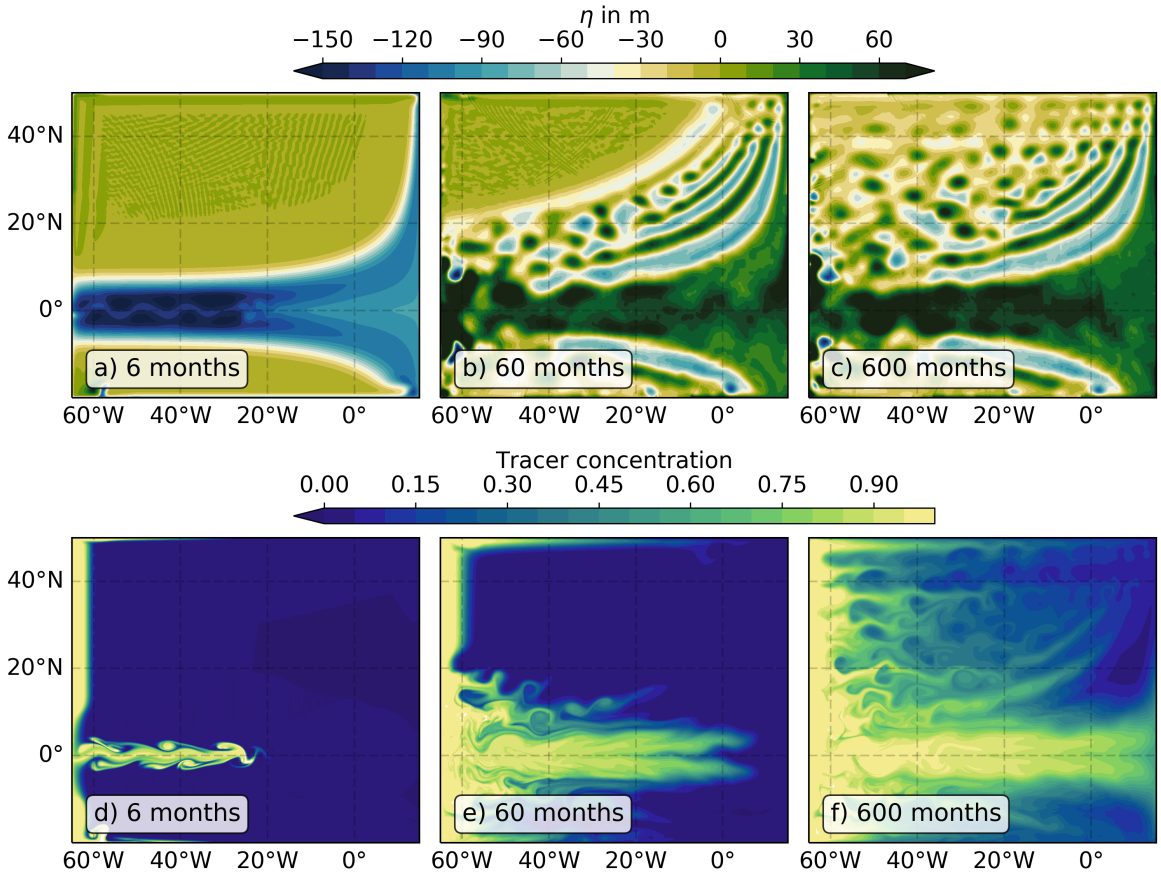

Figure 3.1: Spin-up of the interface displacement (a-c) and tracer field (d-f) in the rectangular basin after 6, 60, and 600 months, respectively. Note that the midpoint of the diverging colorbar for the interface displacement is shifted to negative values, due to the imposed annual cycle of initial mass reduction and subsequent replenishment in the active layer. The initial low amplitude alternating interface displacement signal in the north-west (a,b) is due to numerical errors.

In the following, the non-linear model spin-up is described for the rectangular basin

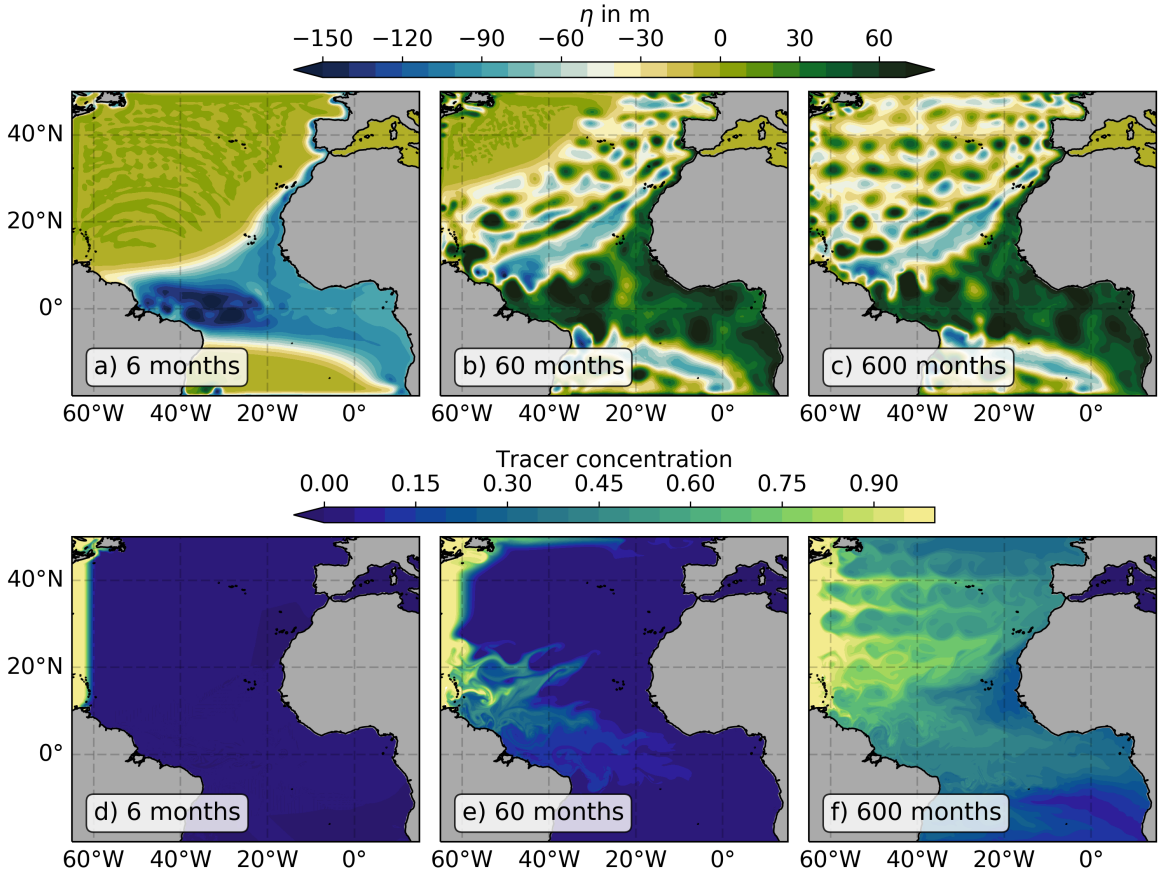

Figure 3.2: Spin-up of the interface displacement (a-c) and tracer field (d-f) in the Atlantic basin after 6, 60, and 600 months, respectively.

configuration (Fig. 3.1), but the description is almost identical for the Atlantic basin (Fig. 3.2). The model is spun-up from rest, starting with a negative phase of the forcing, i.e. an upward suction of the interface (Fig. 3.1a). As the forcing is set to have an equatorial Kelvin wave structure, an eastward propagating equatorial Kelvin wave is immediately excited. At the eastern boundary this Kelvin wave is reflected westwards as a long equatorial Rossby wave, visible by the two local minima slightly removed from the equator in the interface displacement after 6 months. Further, coastal Kelvin waves propagate north and southward along the eastern boundary, exciting off-equatorial Rossby waves (Fig. 3.1b). The Rossby wave fronts move westward into the interior of the basin, where they grow unstable and shed isolated eddies, predominantly of anticyclonic nature (Fig. 3.1c). The instability leading to the break-up of the Rossby

wave fronts appears to be very similar to the resonant triad interaction mechanism described by *Qiu et al.* (2013a), in which the non-linear interaction of Rossby waves leads to the growing anomalies and finally to the break-up of the fronts (c.f. Section 2.3.5; *Pedlosky* (1987)). Once the westward propagating eddies reach the western boundary, their energy is dissipated and they vanish in the so-called "eddy graveyard" (*Zhai et al.*, 2010). North of 40 °N, the eddies are formed directly at the eastern boundary and their amplitude decreases on their way westwards (Fig. 3.1c). The dynamical field is in a statistical steady state, once the Rossby waves or eddies at the northernmost latitude have crossed the entire basin. The theoretical phase speed for long Rossby waves $c_{ph} = \omega/k \approx \beta c^2 f^{-2}$ derived from the dispersion relation (Eq. 2.42) is slightly below $0.01\,\mathrm{m\,s^{-1}}$ at 50 °N, and hence the dynamical spin-up is expected to be finished after ∼20 years.

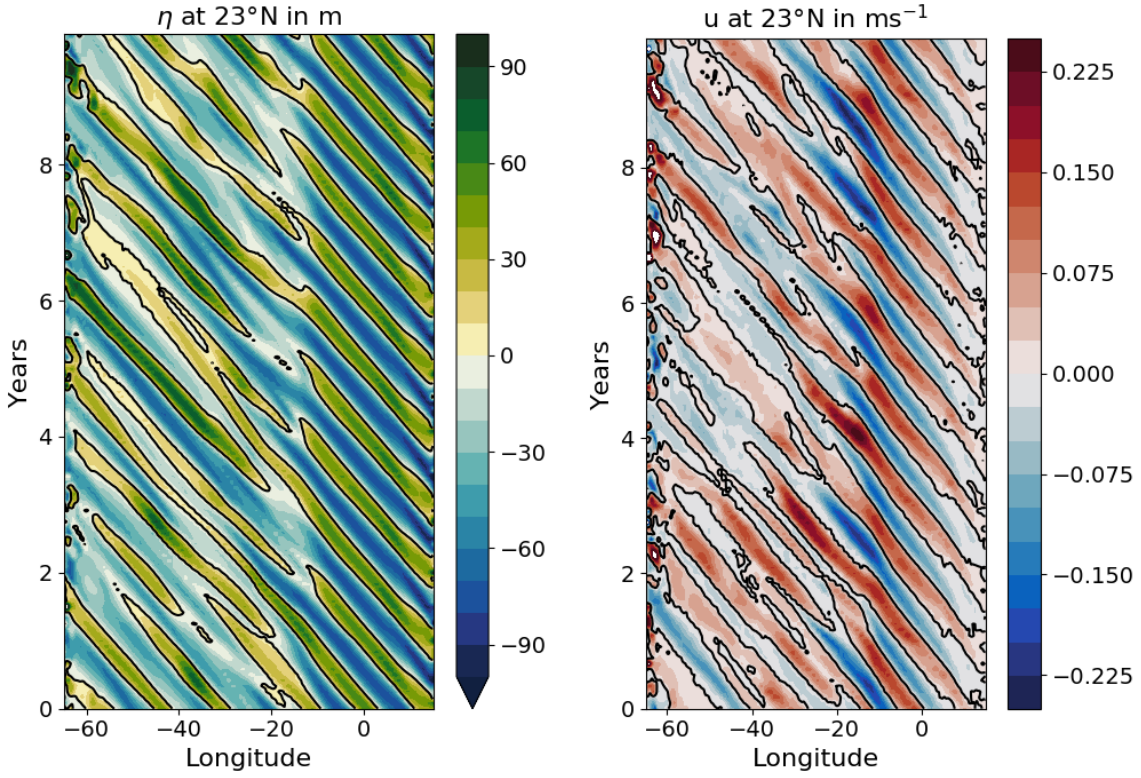

Figure 3.3: Hovmoeller plots of a) the interface displacement and b) the zonal velocity along 23 °N in the rectangular basin for a randomly chosen 10 year period in the spun up state. The black line marks the 0 contour. West of ∼20 °W, the regular Rossby signal breaks up as the generated eddies start to shift latitudes in the turbulent regime.

In the spun-up state the generated eddies follow a pathway more or less along a line of latitude. In a Hovmoeller diagram of the interface displacement along 23 °N, the westward propagation of the eddies is clearly visible with a propagation speed similar to the long Rossby wave phase speed, which predicts 5.3 yr for the crossing of the 80 ° wide basin (Fig. 3.3a). The interface displacement shows a regular oscillation with an annual period east of 15 °W, corresponding to the stable Rossby wave fronts. West of 15 °W the signal is subject to some modulations. Here, the Rossby wave fronts have broken up and the interface displacement signal is carried by the westward propagating eddies that undergo some modulation due to non-linear eddy interaction. These irregularities are slightly more pronounced in the zonal velocity field (Fig. 3.3b). However, the still discernible overall regularity in the westward propagation hints towards eddy pathways that are somewhat aligned along a line of latitude.

Co-evolving with the dynamical field, the tracer is transported away from its source region into the basin interior. In Figure 3.1d the tracer injection region along the western boundary is clearly visible. The eastward flow associated with the immediate Kelvin wave development creates an eastward growing tracer tongue. The lower tracer values along the western boundary between 10 °N/S stem from the structure of the forcing and the associated westward off-equatorial flow in geostrophic balance. After 60 months the first off-equatorial Rossby wave fronts/eddies have already reached the western boundary, leading to a widening of the equatorial tracer tongue (Fig. 3.1e). Eventually, the tracer field evolves into a state in which the equatorial tracer tongue reaches all across the equator and has a large enough width, so that the tracer can be transported by the flow along the fronts of the stable off-equatorial Rossby waves (Fig. 3.1f). The arrival of the eddies that propagate westwards more or less along the same line of latitude leads to the formation of off-equatorial tracer tongues or filaments, in which the tracer is passed on from one eddy to the next. Coastal Kelvin waves propagate all around the basin, hence also westwards along the northern boundary, manifesting themselves in a creation of a tracer tongue close to the northern boundary.

In the Atlantic basin, the equatorial tracer tongue is not as pronounced, as the South American continent prohibits the direct interaction between equatorial waves and the tracer source (Fig. 3.2). Only through the arrival of the first off-equatorial signals at the western boundary, the tracer is distributed into an equatorial tracer tongue and into filaments due to the more or less coherent eddy streets. The tracer maximum at the northern boundary observed in the rectangular basin is not visible in the Atlantic model, due to the blocking position of Newfoundland, Canada. However, similar to the rectangular basin, the tracer is transported along the Rossby wave fronts all the way to the Canary islands. East of these wave fronts and north of the equatorial tracer tongue a tracer minimum is established whose location is in general agreement with the OMZ observed in the real ETNA (Fig. 1.2, discussed further in Chapter 4).

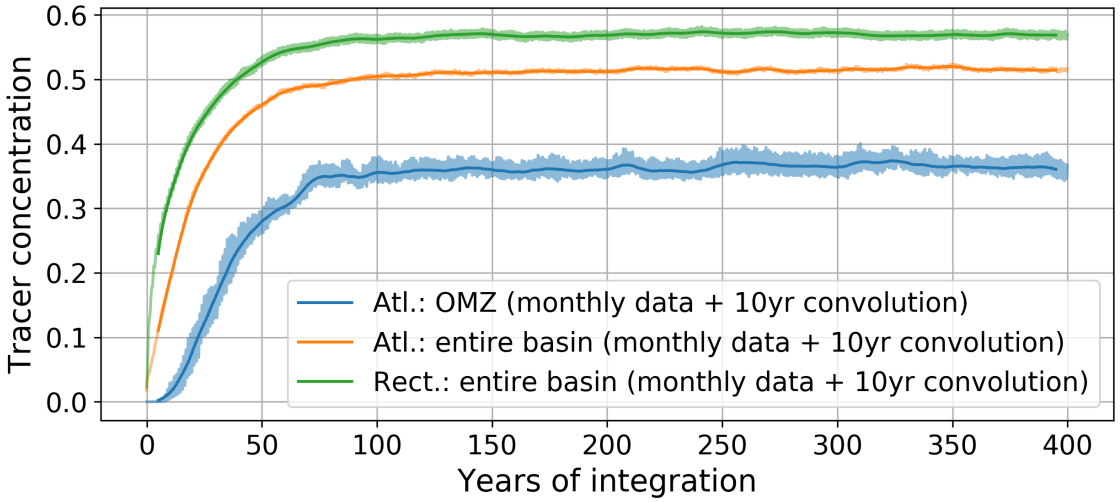

Figure 3.4: Spin-up of the tracer field in the Atlantic and rectangular basin. The orange and green line represent the average over the entire domain, respectively, while the blue line represents an average over the OMZ of Mauritania from 9 °N to 15 °N and 26 °W to 20 °W. A convolution of the time series with a 10 year kernel is superimposed onto each time series. The monthly means shown here are based on thickness-weighted averages $\hat{C}$.

The tracer field takes much longer than the dynamical field to be spun-up. Shown in Figure 3.4 is the temporal evolution of the tracer inventory of the entire model. It becomes obvious that the spin-up for the tracer is only finished after about 150

years. The long duration of the tracer spin-up is related to the long time scale of the tracer consumption J^{-1} and the overall consumption being proportional to the tracer concentration. Even in the spun-up state the overall tracer content is not constant, but shows some fluctuations. Integrated over the whole rectangular basin the tracer content carries a standard deviation of about 0.7% around the mean value of 0.57. The total Atlantic basin has a mean concentration of 0.52 with a standard deviation of 0.51% of this value. In the OMZ of the Atlantic basin, the mean tracer concentration is lower with 0.37 but carries a larger variability of 2.88%, which is rather linked to the smaller averaging region than linked to enhanced variability in the OMZ (see Section 3.5).

3.2 Statistical mean state

3.2.1 Mean fields

As shown in the previous section, the last 80 years of model integration are well within the spun-up state. Hence, Fig. 3.5 shows the mean state calculated over this period for the rectangular basin. The interface displacement shows zonally elongated ridges and troughs, with the highest amplitudes of 45 m (peak-to-peak) found north of 30 °N (Fig. 3.5a). In this latitude band the ridges and troughs extend all the way to the eastern boundary, while they only appear further west closer to the equator. Zonally elongated zonal velocity bands populate the basin (Fig. 3.5c), which are in geostrophic balance with the mean interface displacement field. The zonal velocity is intensified close to the eastern longitude of their emergence. While the mean interface displacement shows weaker amplitudes close to the equator, the zonal currents are most prominent around an equatorial eastward current of more than $5\,\mathrm{cm\,s^{-1}}$, which can be explained by the vanishing Coriolis parameter close to the equator and hence the higher effectiveness of lower pressure gradients to drive geostrophically balanced currents. The meridional

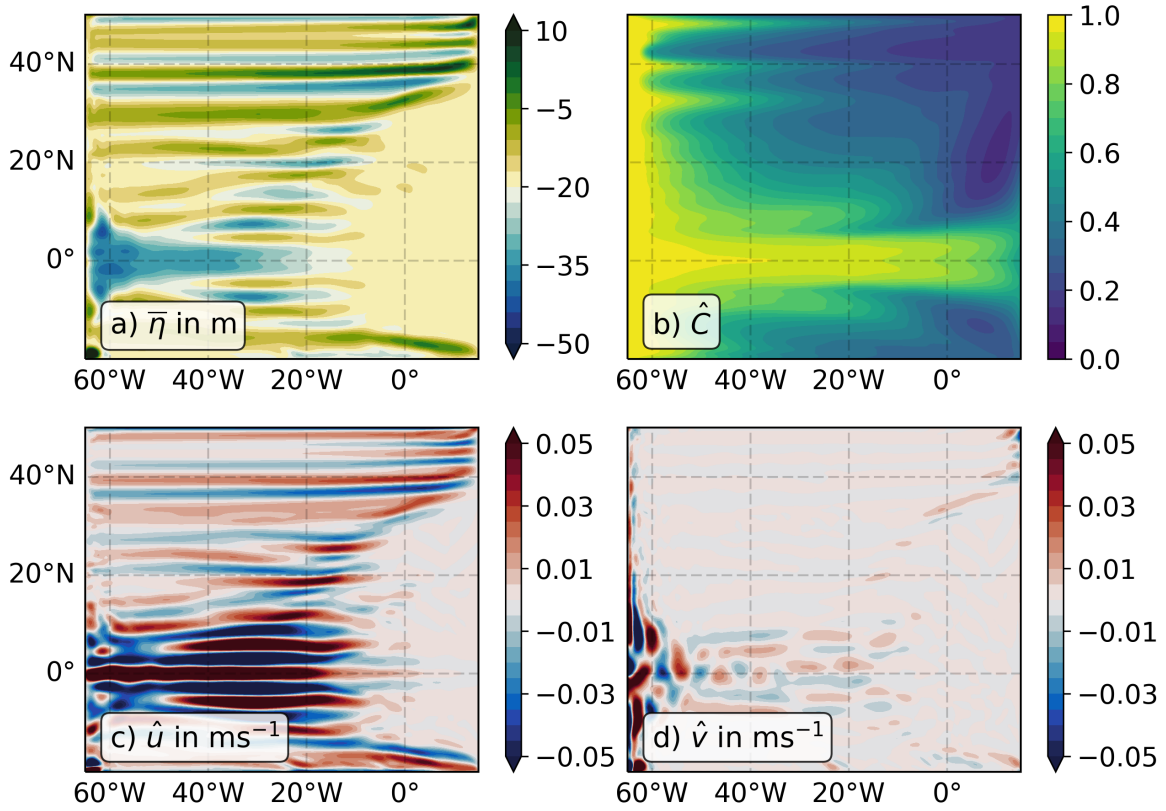

Figure 3.5: Mean fields of the a) interface displacement, b) tracer concentration and c) zonal and d) meridional velocity components in the rectangular basin for the last 80 years of model integration. The interface displacement is averaged in a normal sense, while b-d) show thickness-weighted averages.

velocity hardly shows any signal in the interior of the basin, except near and especially on the equator, where zonally alternating mean velocities of $1\,\mathrm{cm\,s^{-1}}$ are rectified (Fig. 3.5d). The mean tracer field (Fig. 3.5b) shows a pronounced equatorial oxygen tongue, with a secondary maximum at around 10 °N/S on each hemisphere respectively, clearly visible at 20 °W. Two pronounced tongues are further established at around 32 °N and 40 °N, which are in the region of the intense tracer filaments visible in an instantaneous snapshot (Fig. 3.1f). A tracer minimum is observed on the eastern side of the basin, centred at 20 °N and 10 °E, i.e. close to the eastern boundary. To its west, a ridge of higher tracer concentrations stretches from the equatorial secondary maximum into the north-eastern corner of the basin. The position of this ridge corresponds to the location of emergence of the zonal current bands.

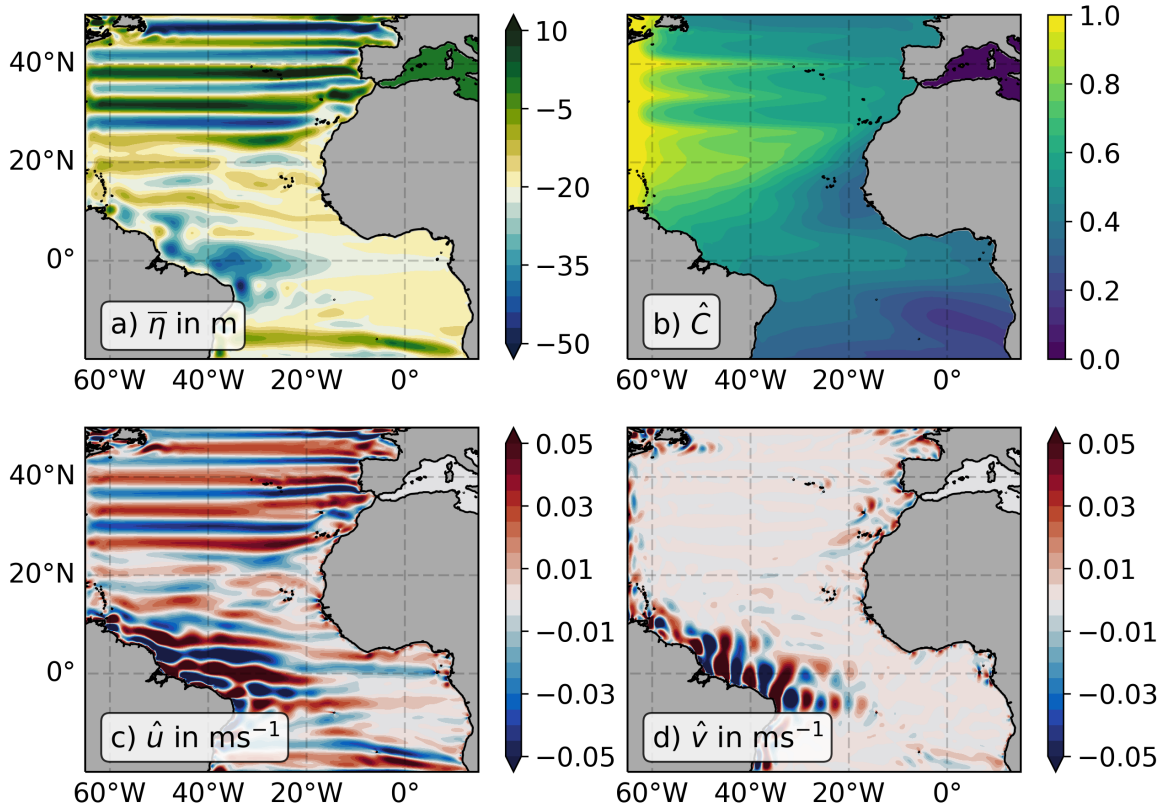

Figure 3.6: Mean fields of the a) interface displacement, b) tracer concentration and c) zonal and d) meridional velocity components in the Atlantic basin for the last 80 years of model integration. The interface displacement is averaged in a normal sense, while b-d) show thickness-weighted averages.

In the Atlantic basin, the overall picture is similar with some intensified patterns. The zonal current bands show stronger velocities north of 25 °N, associated with stronger peak-to-peak amplitudes of the ridges and troughs in the interface displacement (Fig. 3.6a,c). Between 25 °N and about 10 °N, the zonal current bands stretch from the western boundary all the way to the African continent with zonally constant strength of about 1 cm s^{-1}. Along the African coast small intensified mean zonal and meridional velocity signals appear in association with capes or other pronounced topographic features. Also the Cape Verde Islands or the Canary Islands seem to influence the flow field (Fig. 3.6c,d). Around the equator, the zonal velocity reaches a global maximum with flow amplitudes of over 5 cm s^{-1}. This maximum is most pronounced at the western boundary, again with an eastward current situated directly on the equa-

tor. The zonally alternating meridional velocity signal is again present on the equator with over $5\,\mathrm{cm\,s^{-1}}$, hence larger amplitudes compared to the rectangular basin. The equatorial tracer tongue is much weaker in the Atlantic basin (Fig. 3.6b), but still a local tracer minimum is observed directly north of it off the Mauritanian coast, as already foreseen in the spin-up (Fig. 3.2f). Its western boundary is again marked by a slanted gradient in tracer concentration reaching from the Canary Islands past the Cape Verde Islands into the interior of the basin.

3.2.2 Variability

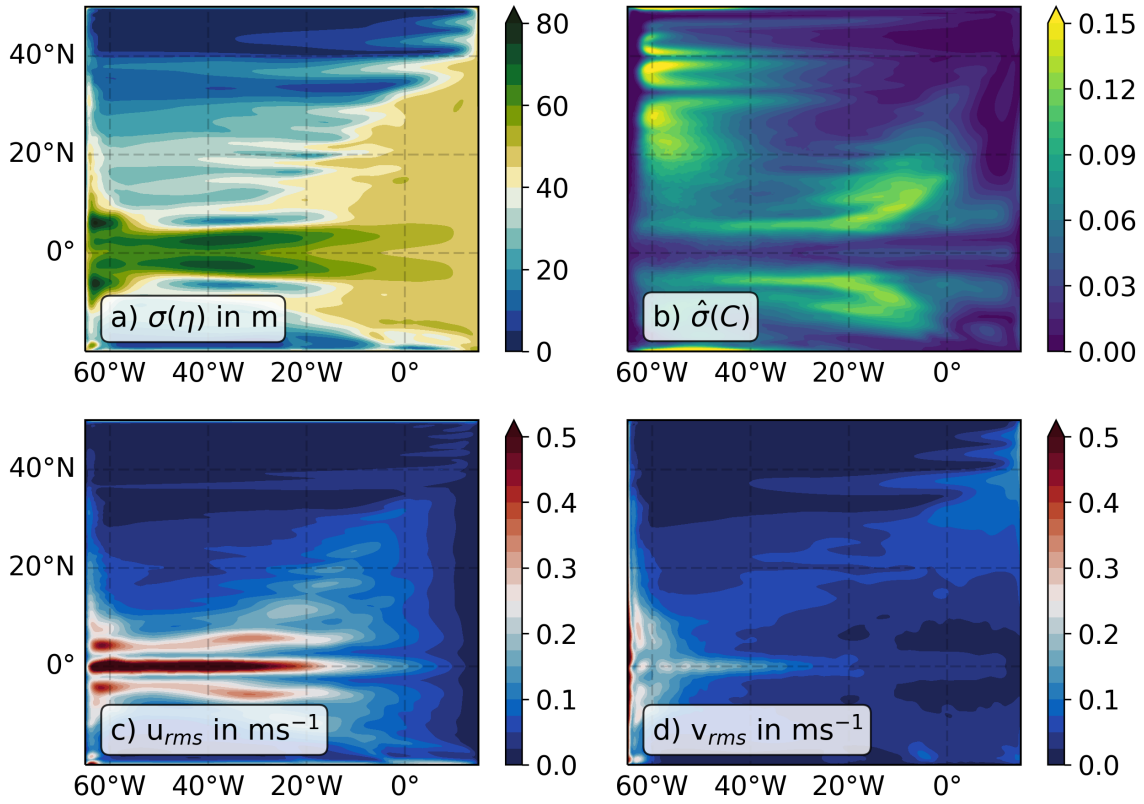

Figure 3.7: a) Standard deviation of the interface displacement and b) thickness-weighted standard deviation of the tracer content for the last 80 years in the rectangular basin. Panel c) and d) show the root mean square zonal and meridional velocity for the same period, respectively.

In their spun-up states the models exhibit a pronounced variability, which is mostly marked by the annual period forcing, but also contains fluctuations on other temporal

scales (further analysed in Section 3.5). The standard deviation field of the interface

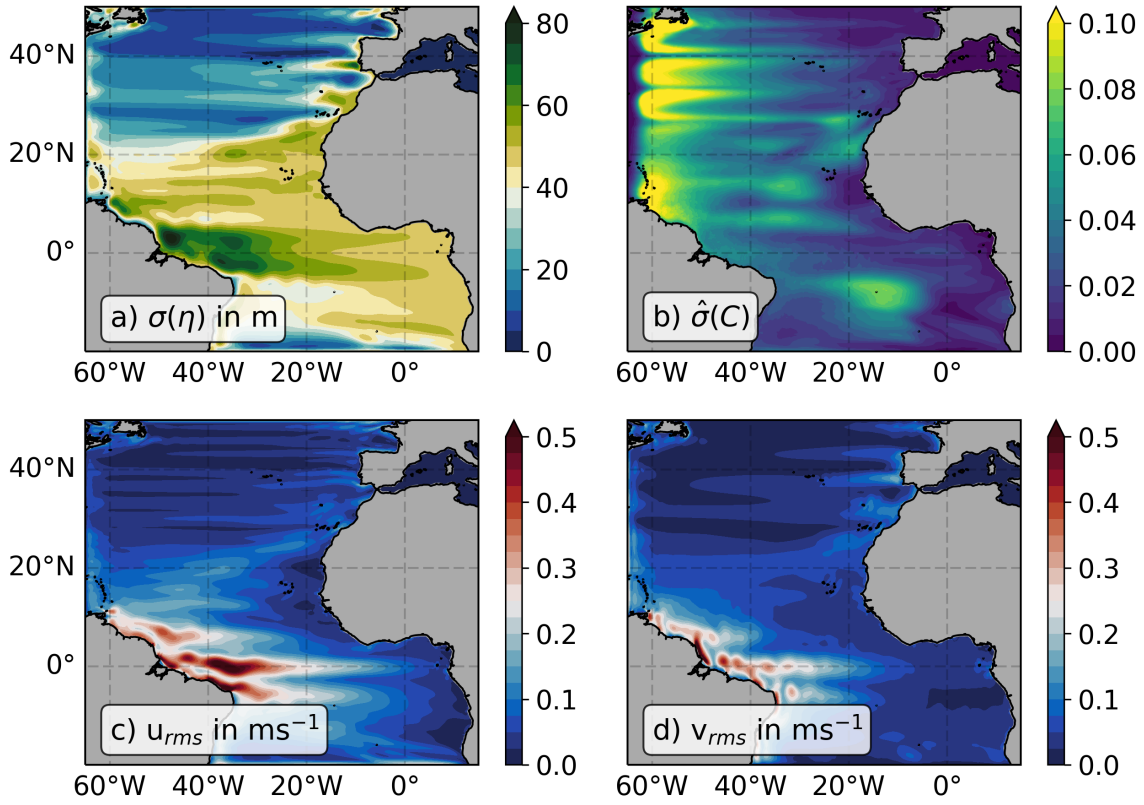

Figure 3.8: Standard deviation of a) interface displacement and b) tracer content for last 80 years in the Atlantic basin. Panel c) and d) show the root mean square zonal and meridional velocity for the same period, respectively. The standard deviations for the horizontal velocities (not shown) carry a similar amplitude and structure to the root mean square fields.

displacement in the rectangular basin carries the clear imprint of the regular Rossby wave fronts with a spatially coherent standard deviation of about 50 m (Fig. 3.7a) on the eastern side of the domain. West of the frontal break-up line, the imprint of the zonal current bands is visible, with tongues of increased variance emanating from the break-up line and decreasing amplitude further west, in agreement with the weakening eddy amplitude towards the west (Fig. 3.1c). Predominantly the zonal and also to a lesser degree the meridional velocity variability is enhanced along the equator and around the break-up of the Rossby wave fronts, displayed by their root mean square velocity in Fig. 3.7c,d. The tracer shows its most predominant variability at the eastern edge of the tracer source region, where tracer is removed and transported into

the basin interior by the impinging eddies, and constantly replenished afterwards (Fig. 3.7b). Increased tracer variability is further maintained along the zonal current bands. Another hotspot of tracer variability is located eastward/equatorward of the break-up of the stable Rossby wave fronts, related to the annual tracer tongues forming along the stable fronts.

In the Atlantic basin the general picture is similar (Fig. 3.8), with the difference that the interface displacement shows a larger standard deviation of up to 50 m across the basin from the equator up to 20 °N, highlighting that the Rossby wave fronts in this latitude bands do not fully disintegrate on their way west (Fig. 3.8a). In fact, snapshots of the interface displacement show coherent Rossby waves front signals across the entire Atlantic (Fig. 3.2b,c). The tracer variability around the tracer minimum off the Mauritanian coast also differs from the rectangular case. The northern boundary of the tracer minimum migrates annually by $\sim$5 ° along the African coast (about between 17 °-22 °) in accordance with the shedding of Rossby waves (not shown). Its imprint is visible in the increased variance in tracer concentration around 20 °N off the African coast (Fig. 3.8b). The southern and western boundary of the tracer minimum region are also marked by slightly increased variability, with a maximum in variance around 5 °N and 30 °W, respectively.

3.3 Zonal current bands - their meridional scale and dynamics

The zonal current bands visible in the temporally averaged zonal velocity fields (Fig. 3.5 and 3.6), from here on synonymously referred to as (latent) zonal jets, exist predominantly in the region of the non-linear eddies. Especially north of 30 °N, the eddies seem to propagate along the same lines of latitude, so that in the temporal average strong zonal current bands are rectified. Further south, the non-linear eddies interact

with each other, causing them to shift latitudes during their westward propagation. This is reflected by weaker mean zonal jets, especially in the Atlantic basin. In the Atlantic basin, the zonal jets also exist, although weak, in the region of the tracer minimum, which is located east of the region where the Rossby wave fronts break up into eddies. In the rectangular basin, they generally appear only to the west of the Rossby wave break-up. However, closer to the equator the zonal jets also exist in regions where the Rossby wave fronts are still stable. In the rectangular basin their presence is especially visible around the equator at 15 °W (Fig. 3.5c).

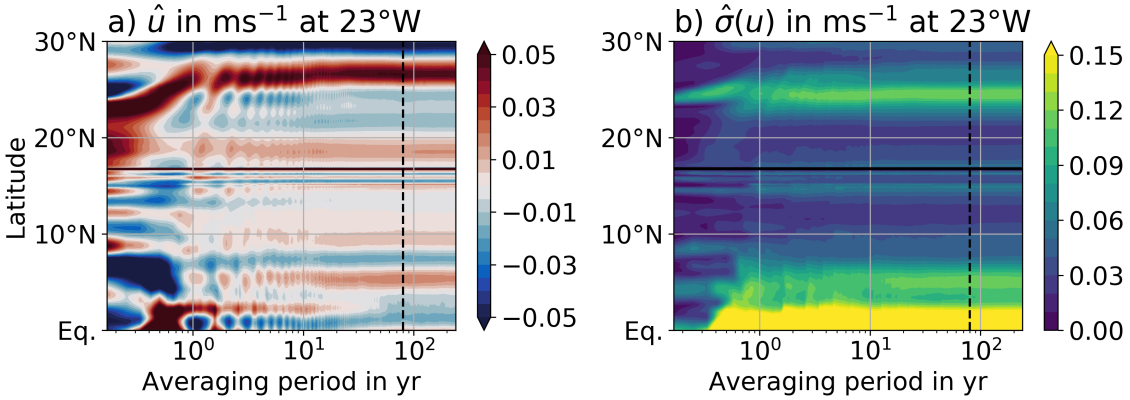

Figure 3.9: a) Thickness-weighted mean and b) thickness-weighted standard deviation of zonal velocity as a function of the averaging period at 23 °W in the Atlantic basin. The start point is arbitrarily chosen to be at year 160 of the model integration. The averaging period is increased monthly until the end of the model run.

To better understand the zonal current bands that ultimately affect the tracer distribution in the model, this section analyses the dynamics behind their formation, comprising an analysis of their meridional scale. A first idea of their rectification time scale is given by Fig. 3.9a, which shows the mean zonal velocity for varying averaging periods at 23 °W in the Atlantic basin, arbitrarily chosen to begin at year 160 of the model integration. Spanning the latitudinal range from the equator to 30 °N, three different regions are shown: the equatorial region, the tracer minimum region and the region north of 25 °N, marked by stronger zonal jets. Thereby, only the northernmost region is already marked by westward propagating non-linear eddies. The two

regions to the south are marked by still stable Rossby wave fronts. Averaging the zonal velocity over less than 20 years leads to zonal jets slightly varying in latitude, depending on the averaging length. This behaviour is mostly visible around 10 °N, where the eastward velocity signal meanders by 1 ° in latitude. Averaging periods of more than 20 years lead to consistent zonal jets, with only minor variability in structure and strength. Correspondingly, the standard deviation of the zonal velocity signal increases with averaging periods up to 20 years and remains about constant for longer averaging periods (Fig. 3.9b).

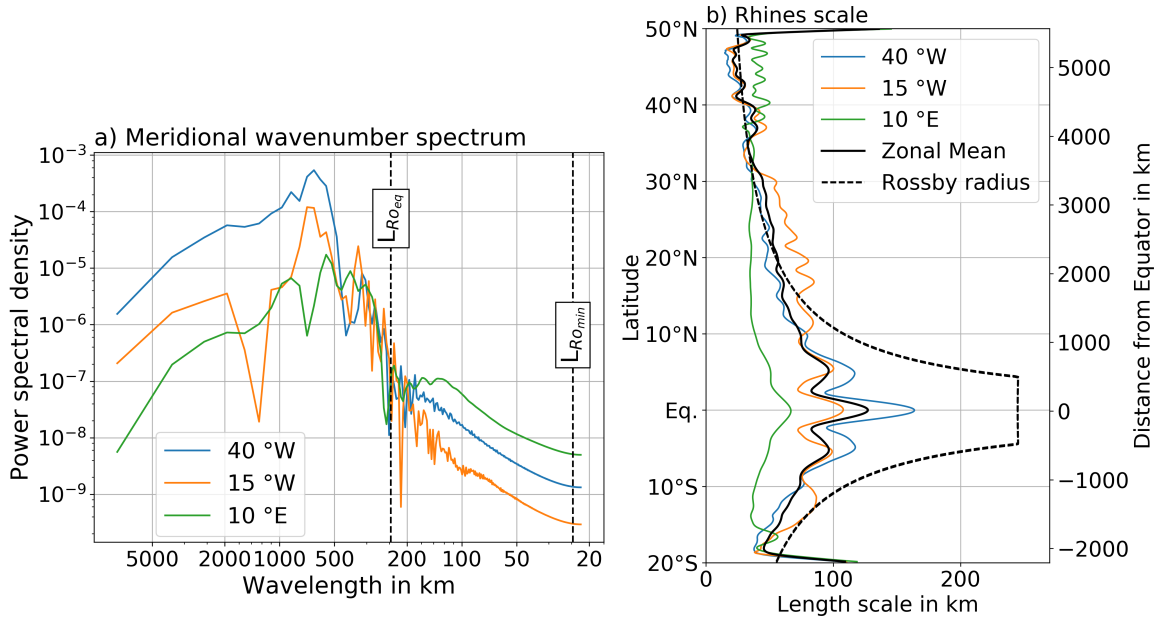

Figure 3.10: a) Meridional wavenumber spectra for the zonal velocity in the rectangular basin at three different longitudes (40 °W, 15 °W and 10 °E), for which the Fourier transform was calculated at each time step over the last 80 years of model integration and subsequently averaged. The corresponding spectral density peaks are at wavelengths of 648 km, 707 km and 555 km, respectively. Given by the vertical dashed lines is the range of baroclinic Rossby radii of deformation within the domain. The smallest is found at the maximum latitude ($L_{Ro_{min}}$) and the largest is given by the equatorial Rossby radius of deformation ($L_{Ro_{eq}}$). b) The Rhines scale dependent on latitude at the three different longitudes and the zonal mean. The baroclinic Rossby radius, with its equatorial definition around the equator, is given by the dashed red line.

Calculating a mean meridional wave spectrum of the zonal velocity field in the rectangular basin reveals dominant wavelengths of around 650 km to 700 km for longitudes where the zonal jets are fully developed (Fig. 3.10a). In the eastern part of

the basin, where the zonal jets exist only in the northernmost latitudes, the dominant wavelength is at around 550 km. In all cases, the dominant wavelength exceeds the baroclinic Rossby radius of deformation, which ranges in the domain from ∼25 km at 50 °N to 245 km on the equator (Fig. 3.10b). Hence, the jets and correspondingly the eddies that lead to their rectification are generally wider than first mode baroclinic eddies typically found in these latitudes.

Another theoretical length scale associated with the meridional scale of zonal jets resulting from geostrophic turbulence on a β-plane is the Rhines scale (see Equation 2.26 for its definition). To compare the meridional scale of the zonal jets from the rectangular basin model run to this theoretical concept, the Rhines scale is calculated at the same longitudes for which the meridional wave spectra were estimated (Fig. 3.10b). It shows for all longitudes a maximum at the equator ranging from 66 km to 163 km, with smaller values on the eastern side of the basin, where the zonal rms velocity is lower (Fig. 3.7c). Moving away from the equator, the computed Rhines scale decreases almost linearly for the two western longitudes (40 °W, 15 °W) down to 15 km at around 45 °N. At 10 °E the Rhines scale is computed to be relatively constant around 35 km north of 10 °N. The zonally averaged Rhines scale shows properties corresponding to the western longitudes, i.e. to the fully developed zonal jet system. For all computed scales, the imprint of the zonal jets is visible by the meridional oscillations in the zonal rms velocity field (Fig. 3.7c). In comparison with the Rossby radius of deformation, the computed Rhines scale is smaller within the equatorial band up to 15 °N/S, but is roughly similar outside of this region. Overall, the computed Rhines scales are similar to the Rossby radius of deformation and are hence smaller than the dominant meridional wavelengths diagnosed from the mean zonal velocity field.

As the zonal jets have been shown to be rectified by Rossby waves and non-linear eddies (Fig. 3.9a), their meridional scales or wavelengths are likely to be tightly

connected. In a study by *Qiu et al.* (2013a), non-linear resonant triad interaction has been suggested to be the responsible mechanism behind the break-up of the Rossby wave fronts. Thereby, the wavelengths of the most unstable secondary waves involved in the instability process appear to set the resulting eddy size. In the following, the resonant triad instability process is analysed in order to compute these meridional length scales.

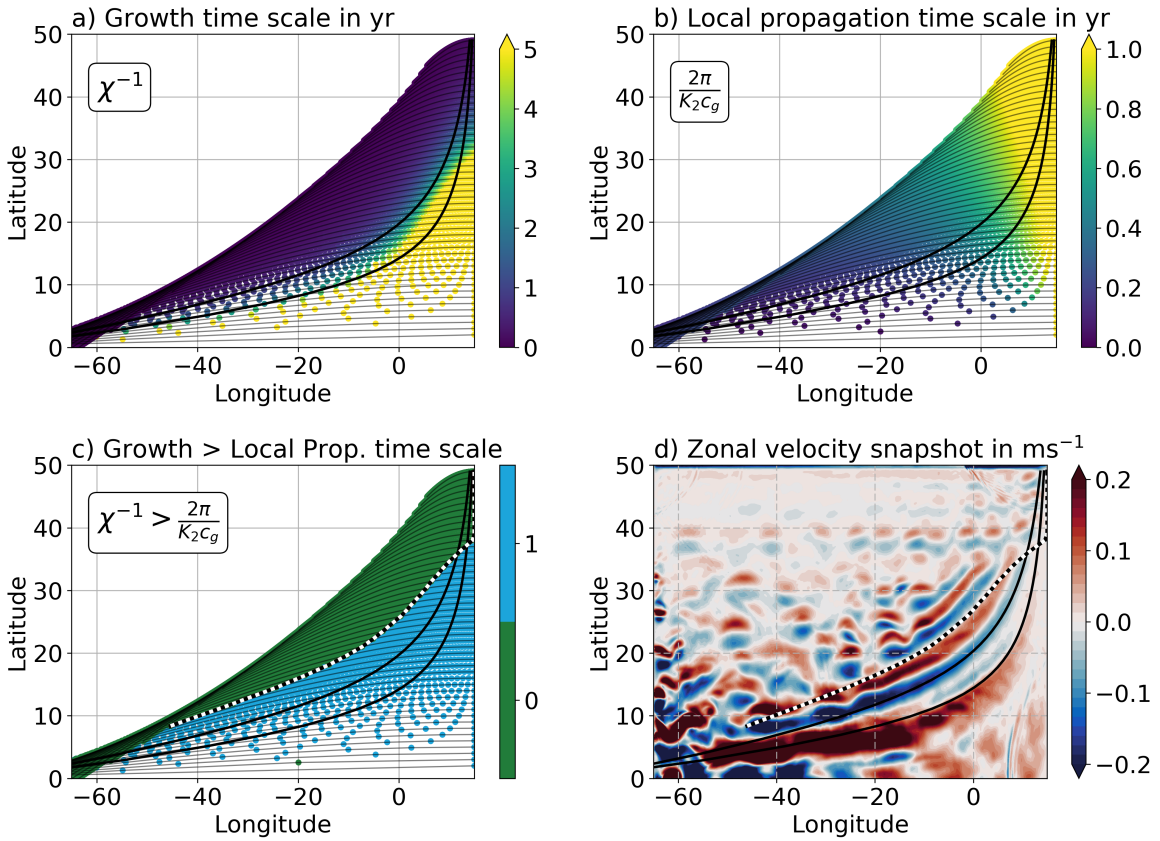

Figure 3.11: a) Growth time scales of the most unstable secondary waves in the resonant triad interaction along Rossby wave ray paths on a β-plane. b) Propagation time scale of the primary Rossby wave along the ray paths. Note the different colorbar in comparison to a). c) Comparison of the growth time scales and local propagation time scale from a) and b). The boundary is marked by the black-white dashed line. d) Snapshot of the zonal velocity u in the rectangular basin at the end of the model run for the northern hemisphere. The black-white dashed line is the same as in c) but is projected into spherical coordinates (see text for details). In all panels the two black lines mark phase lines of the Rossby wave fronts. In d) these lines are again projected into spherical coordinates for consistency.

Following the instability analysis described by *Pedlosky* (1987) and *Qiu et al.* (2013a)

(c.f. Section 2.3.5), the growth rates χ (or their inverse, i.e. the growth time scales) of the most unstable secondary waves are computed along the ray paths of primary Rossby waves on a β-plane. Figure 3.11a shows the growth rates of the most unstable short secondary waves (Eq. 2.39), assuming the amplitude a_2 of the primary wave to be 75 m, which corresponds to about $\sqrt{2}$ times the standard deviation of the interface displacement field along the eastern boundary (Fig. 3.7a), which is solely governed by the annually oscillating wave signal that propagates along the eastern boundary. The growth time scale decreases along the ray path, corresponding to ever larger growth rates, implying that the primary wave grows more and more unstable. The ray paths emanating from northern latitudes are subject to larger growth rates and hence exhibit more unstable waves, while the ray paths remain more stable on their way west closer to the equator. Note that due to the distorted wave front shape (see phase lines in Fig. 3.11a), it is not obvious from Fig. 3.11a that the waves close to the equator remain more stable over a longer period of time. A threshold as to when the primary wave is said to break-up is given by the local propagation time scale of the Rossby wave front. This time scale is given by $2\pi \left(K_2 c_g\right)^{-1}$, where $K_2 = \left(k^2 + l^2\right)^{1/2}$ is the total wavenumber of the Rossby wave and $c_g = \left(\left(\partial\omega_2/\partial k_2\right)^2 + \left(\partial\omega_2/\partial l_2\right)^2\right)^{1/2}$ is the group velocity derived from the Rossby wave dispersion relation (Eq. 2.42). When the growth time scale is larger than the local propagation time scale, the triad instability mechanism is too weak to extract energy from the primary wave while it propagates westwards. If the growth time scale is smaller, the secondary waves grow quicker than the primary wave can propagate westward, hence breaking up the primary wave front. Thus, the location of the breakdown of the primary wave front is expected to be where $\chi^{-1} = 2\pi \left(K_2 c_g\right)^{-1}$ (*Qiu et al.*, 2013a). Figure 3.11b shows the local propagation time scale along the ray paths with faster waves towards the equator. In Fig. 3.11c the location of expected break-up is finally diagnosed by comparing the time scales. The break-up line runs from the north-east of the basin to the south-west and is even more slanted than the lines of the same Rossby wave phase in the north-eastern corner. In

fact, the theory predicts the Rossby wave fronts north of ∼37 °N to be immediately unstable at the eastern boundary, before propagating into the interior. Projecting and imposing this break-up line, derived from theoretical considerations on an equatorial β-plane in Cartesian coordinates onto a snapshot of the zonal velocity (Fig. 3.11d) in spherical coordinates, shows a general agreement with the emergence of the eddies from the Rossby wave fronts. The projection has thereby little effect on the exact position of the line. This result suggests the resonant triad interaction to be the responsible instability mechanism, at least north of ∼10 °N. South of this latitude the Rossby wave fronts seem to pass too quickly through the 80 ° wide basin, leaving not enough time for the instability process to kick in.

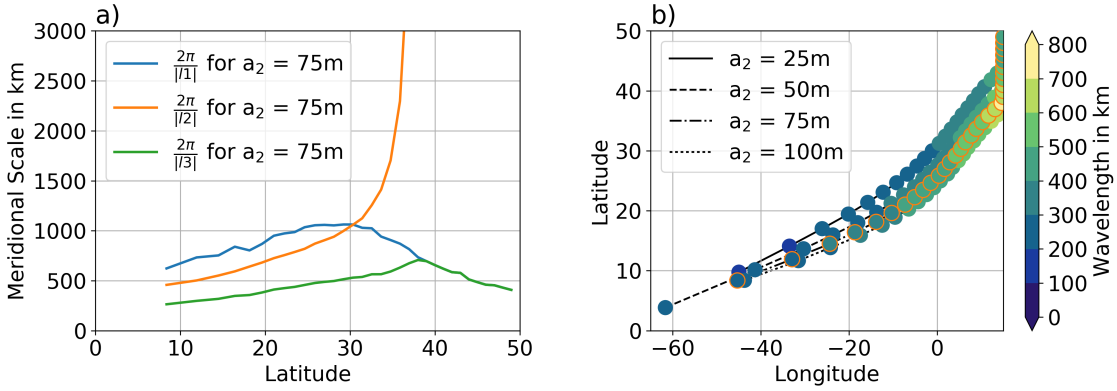

Figure 3.12: a) Meridional wavelengths of the primary wave (orange), the most unstable short secondary wave (green) and the corresponding long secondary wave (blue) undergoing triad interaction at the break-up line of the Rossby wave front for a primary wave amplitude of $a_2 = 75\,\mathrm{m}$. b) Location of the Rossby wave front break-up and meridional scales of the most unstable short secondary waves $2\pi|l_3|^{-1}$ that extract energy from the primary wave for four different amplitudes of the primary wave $a_2 = 25\,\mathrm{m}$, $50\,\mathrm{m}$, $75\,\mathrm{m}$ and $100\,\mathrm{m}$. The scatter markers carry an orange edge for the $a_2 = 75\,\mathrm{m}$ case.

In a next step, it is then possible to infer the wavelength of the most unstable secondary waves at the moment of the break-up of the Rossby wave front (Fig. 3.12a). The energy of the primary wave will be mostly transferred to this wavelength and hence set the size of the emerging eddies. The wavelengths of the most unstable short secondary waves at the break-up location of the Rossby wave fronts range between

206 km to 708 km, with a mean value at around 500 km and their peak at 38 °N. The corresponding long secondary waves participating in the wave triads show wavelengths up to 1070 km peaking at around 30 °N (Fig. 3.12a). Overall, the wavelengths of the secondary waves correspond well to the dominant wavelengths found by the meridional wavenumber spectrum. While the most unstable short secondary waves exhibit wavelengths smaller than 500 km south of 25 °N and thus appear to be too small, the wavelengths of the corresponding long waves drop below 1000 km and mark 610 km at 8 °N, implying that within the latitudes closer to the equator, the long secondary waves might be responsible for setting the eddy size. However, as visible in Fig. 3.11d, the Rossby wave fronts hardly break up within 10 ° around the equator. Thus, the triad instability mechanism does not have enough time to extract energy and transfer it to short secondary waves. Hence, the diagnosed meridional scale of the zonal jets as visible in Fig. 3.5c is set by the still stable Rossby wave fronts and not the secondary waves, as these are still too little developed on their way across the basin.

As pointed out by *Qiu et al.* (2013a), the meridional scale of the most unstable secondary waves is also dependent on the primary wave amplitude, as the growth rates of the secondary waves is proportional to the primary wave amplitude (Eq. 2.39). Lowering the primary wave amplitude shifts the line of break-up further to the west and at the same time decreases the meridional wavelength of the most unstable short secondary waves (Fig. 3.12b). Doubling the primary wave amplitude from 50 m to 100 m leads to an eastward shift of the line by about 3 ° and increases the overall secondary wavelengths by 100 km to 200 km.

The complexity of the eastern boundary structure hinders a similar conceptual approach for the eddy generation in the Atlantic basin, as the ray theory developed by *Schopf et al.* (1981) does not account for realistic coastlines. However, the resonant triad mechanism has been suggested to be active in the Pacific (*Qiu et al.*, 2013a) and is also likely to be active in the Atlantic configuration, thus generating the eddies in

a similar way as described for the rectangular basin. Based on the above presented analysis, the zonal jets west of the Rossby wave front break-up are strongly linked to the non-linear triad instability mechanism, in both the rectangular and Atlantic basin. Neither the equatorial jets that extend far east in the rectangular basin, nor the weaker zonal jets in the region of the Atlantic tracer minimum can hence be directly related to this process. The former seem to be purely related to the stable Rossby wave fronts that are able to stretch across the entire basin. They form around the eastward equatorial mean current, which can be understood as a rectification of the annually excited eastward Kelvin wave. The zonal jets in the tracer minimum region in the Atlantic are most likely the rectification of westward travelling disturbances in the interface displacement field of the Rossby waves induced by topographic features of the African coastline.

3.4 Tracer budget

Following the dynamical analysis of the zonal jets, their impact on the tracer transport through the basin will be analysed in the following section. Applying thickness-weighted averaging to the advection-diffusion model (Eq. 2.7) leads to the tracer budget as given in Eq. 2.20. The tendency of the tracer content on the time scale corresponding to the averaging period can hence be estimated as a sum of the advective flux convergence, the diffusive flux convergence, the restoring terms acting as a source and sink as well as the forcing term. Figure 3.13 shows the fields of the individual terms of the tracer budget for the rectangular basin. The conceptual view obtained from the budget is that along the western boundary the relaxation (Fig. 3.13l) is balanced by the total advective flux convergence which transports the tracer into the ocean interior (Fig. 3.13j). There the advectively driven accumulation of tracer is mainly balanced by the consumption (Fig. 3.13k), with only minor smoothing effects from the diffusive flux convergence, accented in the region of the very pronounced oxy-

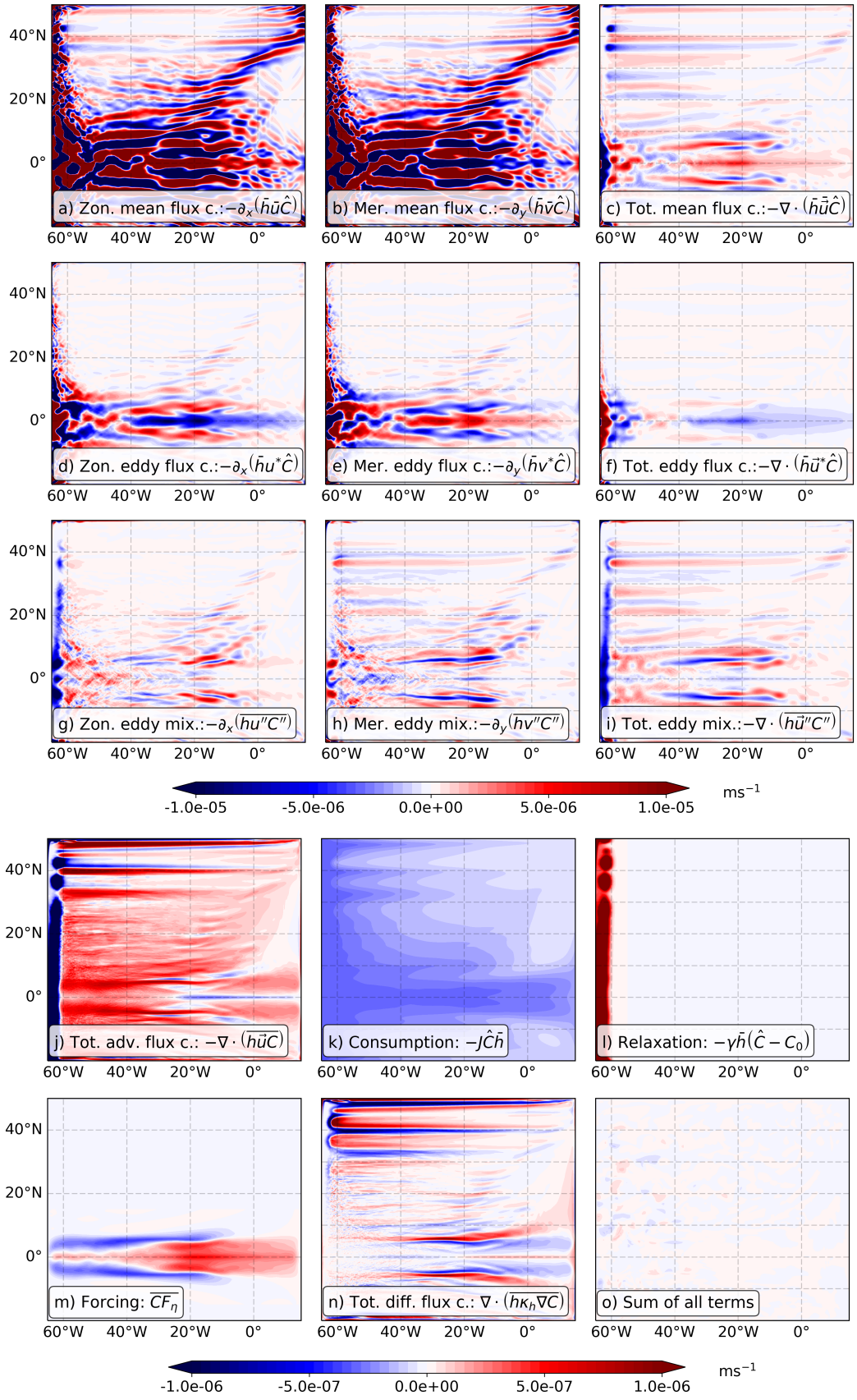

Figure 3.13: Tracer budget terms for the last 80 years of model integration in the rectangular basin. See the panel labelling for the individual panel content, whereby "c." abbreviates "convergence". The decomposed advective terms a) and b), d) and e), g) and h) are summed in c), f) and i) respectively or summarized in j). Note the different colorbar in the lower 6 panels.

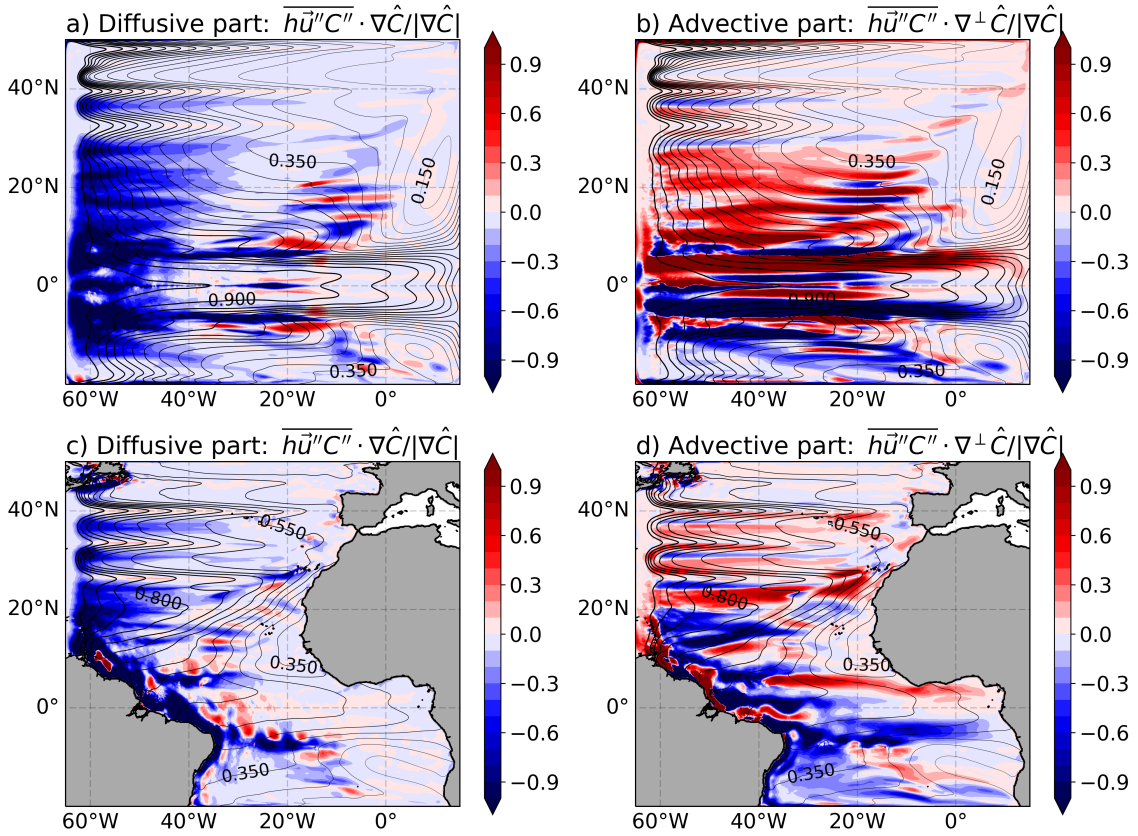

Figure 3.14: Classification of the eddy mixing term in a diffusive part (a,c) and an advective part (b,d) in the rectangular basin (a,b) and the Atlantic basin (c,d). The diffusive part, i.e. the flux across lines of constant concentration, is estimated by projection of the eddy mixing term onto the gradient of the thickness-weighted average of the tracer field. The projection onto the gradient rotated by 90 ° yields the advective part along lines of constant concentration. The projections normalized by the norm of the gradient are given by the colour coding, while the thickness-weighted tracer concentration is given by contour lines. The contour lines are spaced by 0.05 and the contour line thickness is proportional to the tracer concentration.

gen tongues in the northern part of the basin (Fig. 3.13n). The forcing term only has some minor impact along the equator (Fig. 3.13m). In a spun-up state, the tendency of the tracer content should vanish with ever longer averaging periods. Indeed, the tendency estimated as the sum of all terms is close to zero for the 80 yr averaging period, with some low-amplitude exceptions just east of the tracer source region (Fig. 3.13o), where high variance in the tracer concentration is present (c.f. (Fig. 3.7b)).

A more thorough analysis of the total advective flux convergence reveals that each component contributing to the total advective flux convergence has a much stronger

amplitude than the budget terms discussed above and that the individual components cancel each other out to a large degree, leaving the moderate amplitude total advective flux convergence as a residual. The largest amplitudes are given by the zonal and meridional mean flux convergence (Fig. 3.13a,b), which exhibit latitudinally alternating zonally elongated structures corresponding to the zonal jets, which on the northern hemisphere are slightly tilted from the north-east to the south-west, with their eastern end corresponding to the break-up line of the Rossby wave fronts as described in Section 3.1 and deduced theoretically in Section 3.3. East of the break-up line some weaker alternating features exist with an opposite tilt. The zonal and meridional mean flux convergences are of similar amplitude, so that due to cancellation the total mean flux convergence is somewhat weaker, exhibiting clear latitudinally alternating zonal structures in the western part of the basin (Fig. 3.13c) and some reduced equatorial signal. The cancellation along the Rossby wave front break-up line is almost perfect, leaving hardly any total mean flux convergence. Interestingly, even though the basin interior is populated by eddies, the zonal and meridional eddy flux convergences (Fig. 3.13d,e) are much weaker than the mean flux convergences throughout the basin. They further cancel out each other, so that the total eddy flux convergence (Fig. 3.13f) makes hardly any contribution to the total advective flux convergence, with an exception on the equator. The eddy mixing term however seems to play a larger role. The total eddy mixing exhibits (Fig. 3.13i) similar to the total mean flux convergence a meridionally alternating jet structure, but slightly offset and of opposite sign, so that the sum of the two leads to the spatially coherent field of the total advective flux convergence (Fig. 3.13j). The zonally coherent signal in the eddy mixing term in the western part of the basin is rooted in its meridional flux convergence (Fig. 3.13h), while the zonal component only plays a role around the equator (Fig. 3.13g).

As already described in section 2.3.2, the nature of the eddy mixing term can be both advective and diffusive. To classify the eddy mixing term diagnosed here, a projection of the eddy mixing term onto the gradient of the thickness-weighted average of tracer

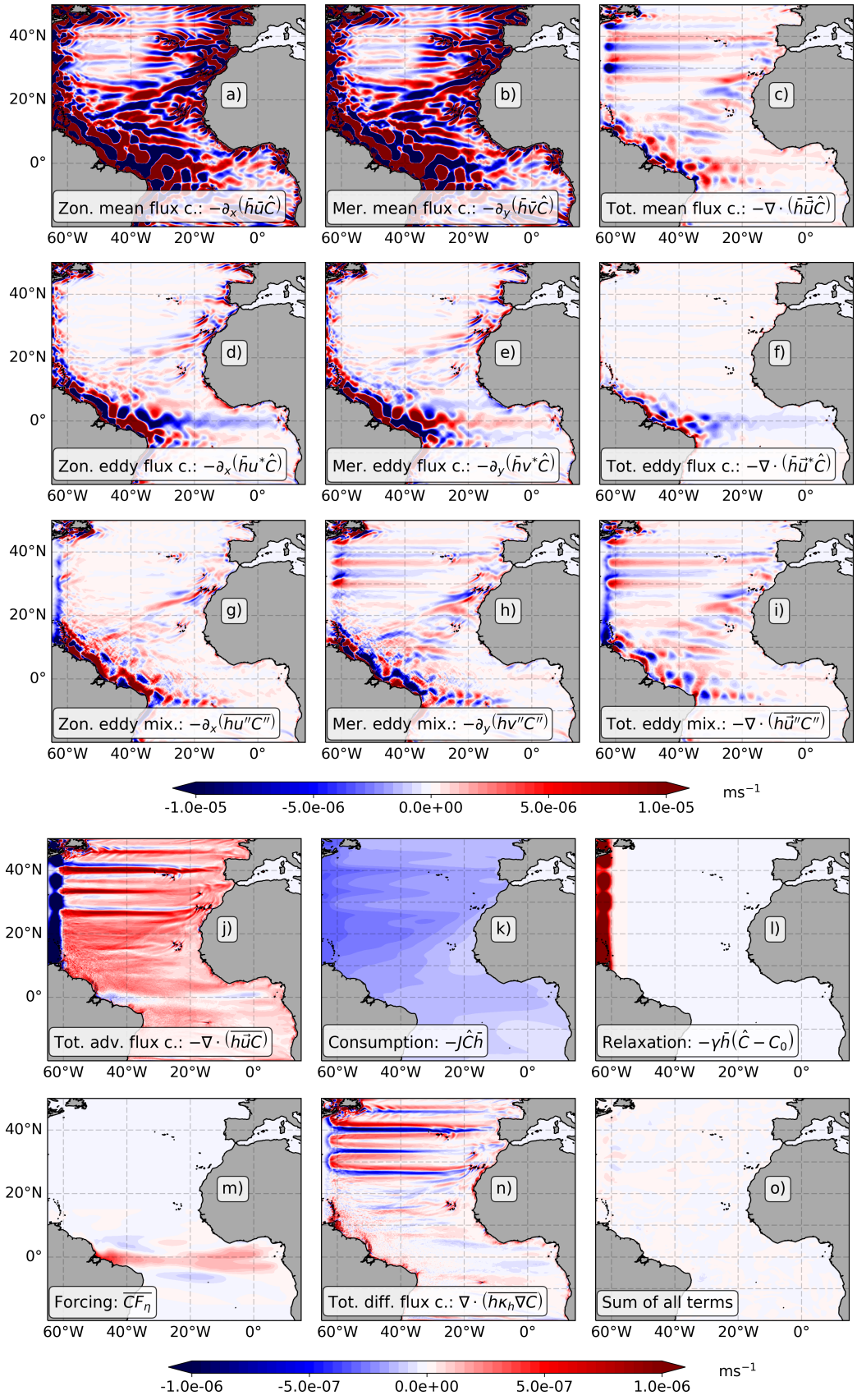

Figure 3.15: Tracer budget terms for the last 80 years of model integration in the Atlantic basin. See the panel labelling for the individual panel content, whereby "c." abbreviates "convergence". The decomposed advective terms a) and b), d) and e), g) and h) are summed in c), f) and i) respectively or summarized in j). Note the different colorbar in the lower 6 panels.

content is performed. This way, the diffusive part is determined, while a projection onto the gradient rotated by 90 ° yields the part that is directed along lines of constant concentration, i.e. the advective part. Figure 3.14a,b shows that a clear distinction cannot be made between the diffusive and advective part with the flux being seemingly equally strong across as along isolines, especially in the western part of the basin. The fact that the diffusive part of the flux is almost entirely directed down the tracer gradient thereby suggests that it is a genuine diffusive flux. In the centre of the basin in the northern hemisphere the advective part is dominant. This also applies to the edges of the equatorial tracer tongue. Along the break-up line of the Rossby wave fronts, the eddy mixing term is composed of both advective and diffusive parts. To summarize the analysis of the advective flux convergence components, the main terms in establishing the northern hemisphere total advective flux convergence are the zonal and meridional mean flux convergence as well as the meridional component of the eddy mixing term. For the latter a clear identification as either advective or diffusive process is not possible. As the diffusive part of the eddy mixing term is mostly directed down the tracer gradient it qualifies as a genuine diffusive flux.

The main results of the rectangular basin tracer budget apply to a large extent also to the Atlantic basin (Fig. 3.15). The biggest difference is that the region in the eastern part of the basin, i.e. off the north-west African coast, the zonal and meridional components of the mean advective flux convergence still exhibit strong latitudinally alternating zonally elongated structures (Fig. 3.15a,b). However in the total mean advective flux convergence the structures cancel out to a large degree, leaving weaker zonally elongated structures, reaching from the basin interior up to the western boundary of the region with locally minimum tracer concentration (Fig. 3.15c). These structures are again balanced by similar structures in the meridional flux convergence associated with the eddy mixing term (Fig. 3.15h). Along the western boundary of the tracer minimum region, the eddy mixing term is again composed of both an advective and diffusive part (Fig. 3.14c,d). The overall results show that there

is no dominant process that transports tracer well into the tracer minimum region. The rather weak total advection of tracer into the region off the north-west African coast is thereby the reason for the establishment of the tracer minimum region.

3.5 Variability of the zonal jets and the associated tracer variability

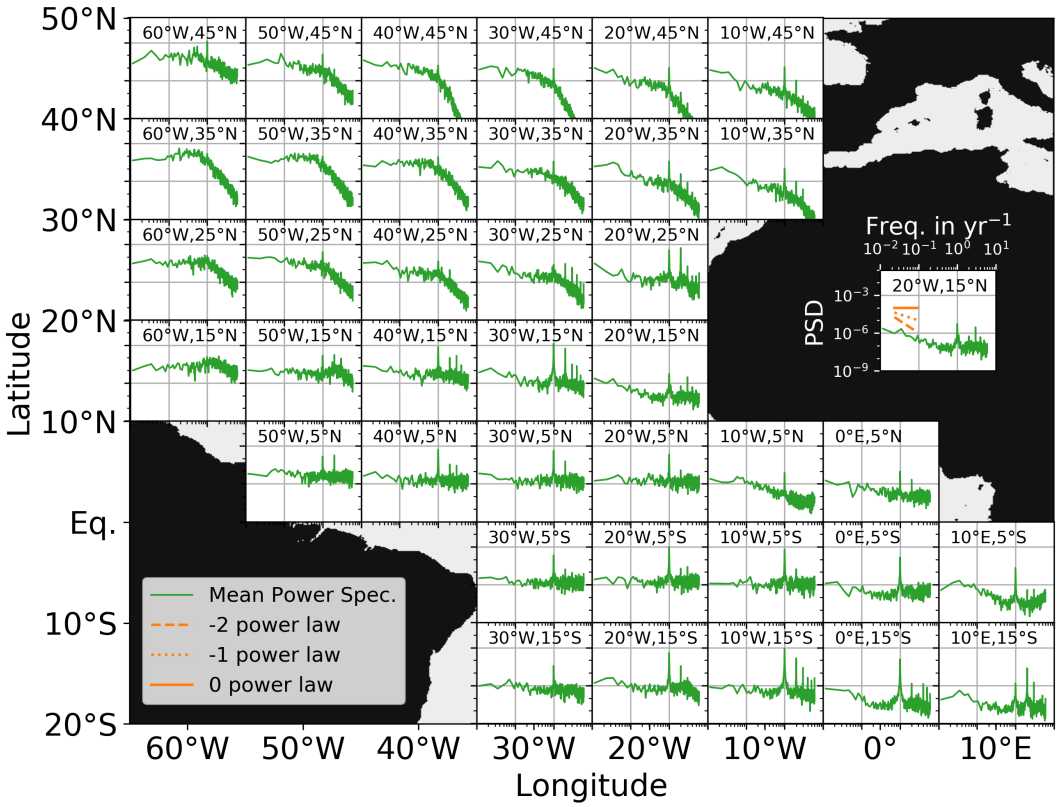

Figure 3.16: Mean power spectra at locations arranged in a 10 °×10 ° grid across the Atlantic basin for the last 240 years of model integration. Per location, four power spectra are calculated for a period of 1024 months with an overlap between sub-samples of 409 months. The spectra are consequently averaged to improve the signal-to-noise ratio. The inset panels are centred at the location of the corresponding time series and are labelled by their coordinates. On the African continent an example panel shows the axis labelling pertinent to all panels and contains for orientation the -2, -1 and 0 power laws, which appear linearly in the log-log plot.

Judging from Fig. 3.8b there is increased variability in the tracer field throughout

large parts of the Atlantic basin. Thereby, areas such as the boundaries of the tracer minimum region off the north-west African coast are marked by increased variance. Conducting spectral analysis of the tracer time series at selected locations across the basin reveals further information about the associated time scales. Figure 3.16 shows power spectra of the tracer time series at single point locations, arranged in a regular 10 ° by 10 ° degrees grid. It reveals that the periodicities of the tracer variability show a strong dependency on the location. Time series around the equator (5 °N and 5 °S) show a general "white" behaviour, i.e. similar power distributed across all frequency bands, with a pronounced peak in the annual period and its shorter harmonics (half year period etc.), linked to the annual forcing period acting on the equator.

Along the eastern boundary, the annual period signal is still well visible, in conjunction with the passage of annual Kelvin waves. However, the "white" behaviour observed at the equator for time scales longer than annual period is changed to a "pink" behaviour. The power increases towards longer periods roughly following a -1 power law. At 20 °W, 15 °N, i.e. in the centre of the tracer minimum region, the power on the longest diagnosed period ($\sim$85 yr) is comparable to the annual peak. Moving into the ocean interior away from the equator, the relative strength of the annual peak weakens, showing almost no peak close to the western boundary or in the well developed eddy field. There the power is generally plateauing on periods longer than the annual period. In summary, despite the solely annual period forcing, spectral analysis reveals variability of the tracer field on longer time scales. In general, no dominant period is discernible for interannual to multidecadal periods. However, especially the region along the eastern boundary, and with it the tracer minimum region, seems to be prone to variations on interannual to multidecadal time scales.

Despite the "pink" behaviour in the tracer minimum region for interannual periods, the overall power in variability seems to be damped. Further, the tracer concentration averaged in the region of the ETNA OMZ (chosen as 9 °N to 15 °N and 26 °W to

20 °W corresponding to *Brandt et al.* (2015)) only shows some low amplitude temporal variability (Fig. 3.4). Because spatial averaging dampens the tracer variance, the variability of the tracer concentration is analysed in more detail along the 23 °W section. Figure 3.17 shows the velocity and tracer field along 23 °W, split up in its thickness-weighted mean state and the corresponding anomalies over the last 240 yr of model integration. The mean state shows the tracer minimum zone between 8 °N and 15 °N

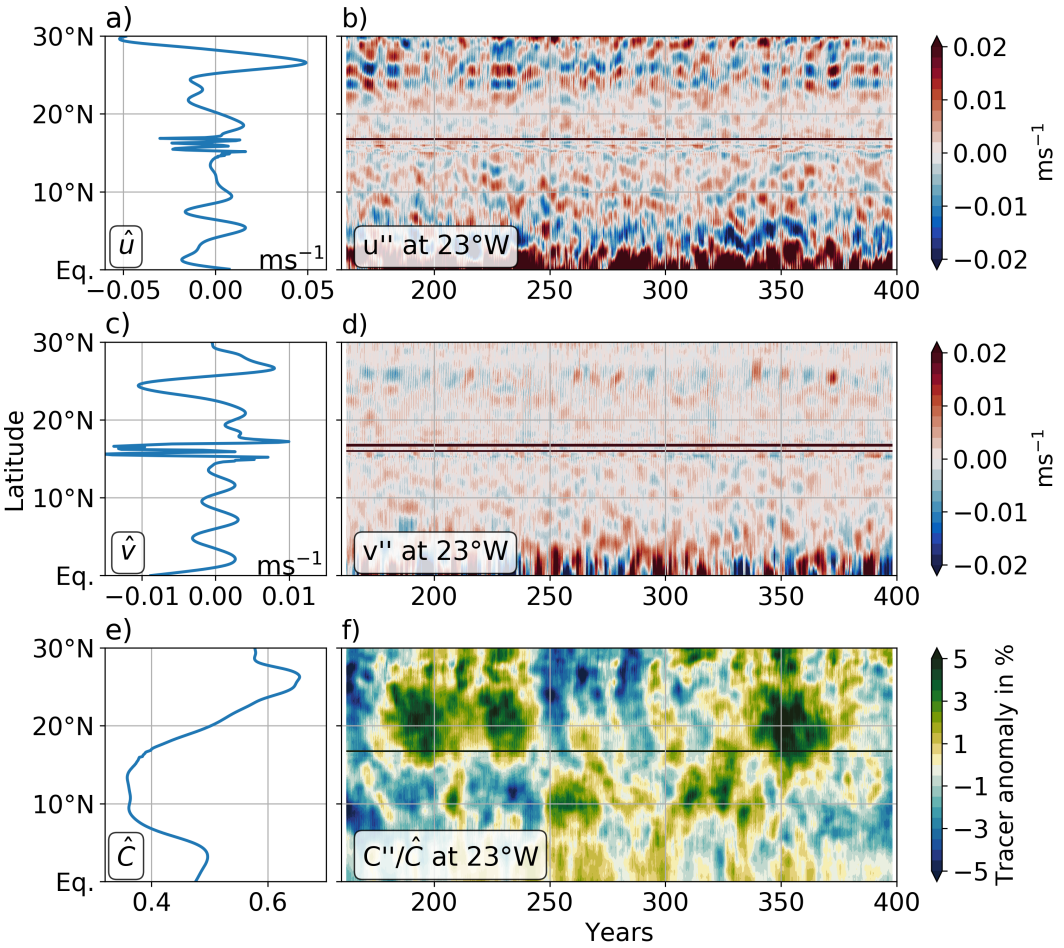

Figure 3.17: Thickness-weighted averages of a) zonal velocity, c) meridional velocity and e) tracer concentration over the last 240 years of the Atlantic basin model integration and the temporal evolution of the corresponding anomalies (b, d, f). The anomalies are convolved with a 4 year (i.e. 49 month) kernel to remove the strong seasonal cycle. Irregularities and black lines at around 17 °N are caused by the presence of the Cape Verde Islands.

(Fig. 3.17e). To the south at around 6 °N, it is bounded by an eastward mean current with a strength of 1.5 cm s^{-1}, while a secondary eastward mean current of 0.5 cm s^{-1}

is present at 10 °N. In between, a westward current of 1.5 cm s^{-1} is established (Fig. 3.17a). At the same time, the meridional component also exhibits a latitudinally alternating velocity signal, although fivefold weaker in amplitude (Fig. 3.17c). Removing the strong annual cycle by lowpass-filtering with a 4 yr kernel reveals interannual to multidecadal variability in the velocity field (Fig. 3.17b,d). North of 20 °N, the zonal velocity field is marked by intensification and weakening of the pronounced zonal currents bands. At times, a latitudinally propagating signal is observed such as at year 210 or 330. While an intensification/weakening hints towards eddies of larger/weaker amplitude, a propagating anomaly must correspond to a latitudinal modulation of the westward eddy pathway. There is hardly any variability on time scales longer than the lowpass filter period around the Cape Verde Islands, but it increases again in the area of the tracer minimum and shows many latitudinally propagating signals of the zonal current bands. Both the zonal and meridional velocity anomalies are of the same order of magnitude as the mean velocities. Hence, the meridional velocity anomalies are a lot weaker, without showing any coherent signals on time scales longer than the lowpass filter period. As the tracer concentration is solely set by the transport through the mean velocity field and as the consumption term is acting on much longer time scales than the lowpass filter period, the interannual variability in the current field must affect the tracer field as well. Indeed, Fig. 3.17f shows tracer anomalies ranging up to 5 % in amplitude of the corresponding mean value that appear consistently over multiple periods reaching from interannual to multidecadal time scales. In the region of the tracer minimum the anomalies reach up to 3 %. Establishing a direct link between the tracer anomalies and the zonal velocity anomalies is however rather difficult. While the positive anomalies at 10 °N between years 300 to 350 are accompanied by a northward propagation of the zonal current anomalies, a similar connection is not visible for the positive anomalies beginning in year 250.

3.6 Comparison with observed oxygen trends

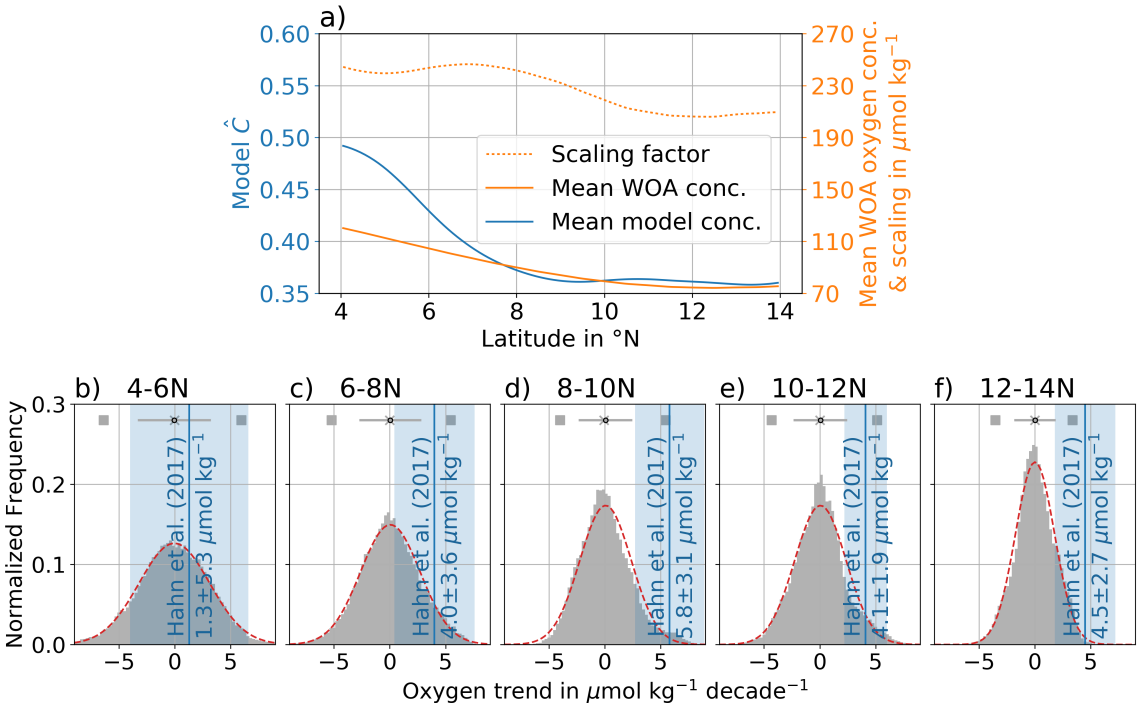

Figure 3.18: a) The thickness-weighted mean tracer distribution in the shallow water model (black line) and the mean oxygen field at 500 m to 800 m depth (solid orange line) obtained from the World Ocean Atlas (WOA) (*Garcia et al.*, 2014) (see Fig. 1.1 for details) along 23 °W. The scaling factor calculated as the ratio between the observed and modelled oxygen/tracer concentration is given in units of μmol kg^{-1} by the dashed orange line. b-f) Distributions of all possible linear decadal trends of the modelled tracer computed along 23 °W over the last 240 years of model integration (grey bars), sorted into 5 bins between 4 °-14 °N. The units of μmol kg^{-1} per decade stem from using the scaling factor from a). Gaussian normal distributions (red dashed curve) are fitted to the distributions. The horizontal grey lines and the black circle show the mean plus/minus one standard deviation. The median is given by the grey cross and the 2.5 and 97.5 percentiles are given by the grey squares. The mean decadal oxygen trends at 500-800 m depth for the same bins and their corresponding uncertainties from *Hahn et al.* (2017) are given in blue.

To put the strength of the tracer anomalies in the Atlantic set-up of the shallow water model in relation with the oxygen variability observed in the real ocean, trends in both contexts are compared. One observational reference are the decadal oxygen trends established for the lower OMZ at depth 500 m to 800 m along 23 °W by *Hahn et al.* (2017). To facilitate a comparison between the model results and the observed trends in the real ocean, the tracer concentrations in the model are scaled to concen-

trations in units of μmol kg^{-1}. The scaling factor is therefore calculated as the ratio between the mean observed oxygen concentration between 500 m to 800 m, obtained from the World Ocean Atlas data (see Fig. 1.1), and the model mean tracer concentration, both along 23 °W (Fig. 3.18a). The scaling factor varies with latitude and ranges between 205 μmol kg^{-1} to 245 μmol kg^{-1} in the latitude range between 4 °N and 14 °N. Subsequently, linear decadal trends of the modelled tracer concentrations can be calculated in units of μmol kg^{-1} per decade. Therefore, the trends are calculated at every grid point and for all possible starting points in time over the last 240 years of model integration. The obtained trends are then sorted into five bins between 4 °N and 14 °N of 2 ° latitudinal width. In each bin a nearly Gaussian shaped distribution of trends is obtained with the mean and median value situated at 0 μmol kg^{-1} per decade (Fig. 3.18b-f), in agreement with the spun-up state of the model. The width of the distribution, e.g. given by the 2.5 and 97.5 percentile, decreases with increasing latitude from $\pm$6 μmol kg^{-1} per decade in the 4 °N-6 °N bin to $\pm$4 μmol kg^{-1} per decade in the 12 °N-14 °N bin. The narrowing of the distributions is thereby outweighing the effect from the coinciding decrease in the scaling factor, indicating a real decrease in decadal variability towards the centre of the ETNA OMZ.

Comparing the obtained trend distributions with the observed decadal trends from *Hahn et al.* (2017) shows a generally good agreement. For three latitude bins (4 °N-6 °N, 6 °N-8 °N, 10 °N-12 °N) the observed trends lie within 95 % of the modelled trends. In the latitude bins 8 °N-10 °N and 12 °N-14 °N the observed trends are slightly larger than the 97.5 ° percentile, but are still represented in the modelled trend distribution. Incorporating the uncertainty of the observed trends, they can also lie within 95 % of the modelled trends. Hence, all observed trends might be possible realisations of the modelled trends.

The decadal trends diagnosed from *Hahn et al.* (2017) are in line with the findings by *Brandt et al.* (2015), who diagnose for a larger region in the ETNA OMZ (9 °N-

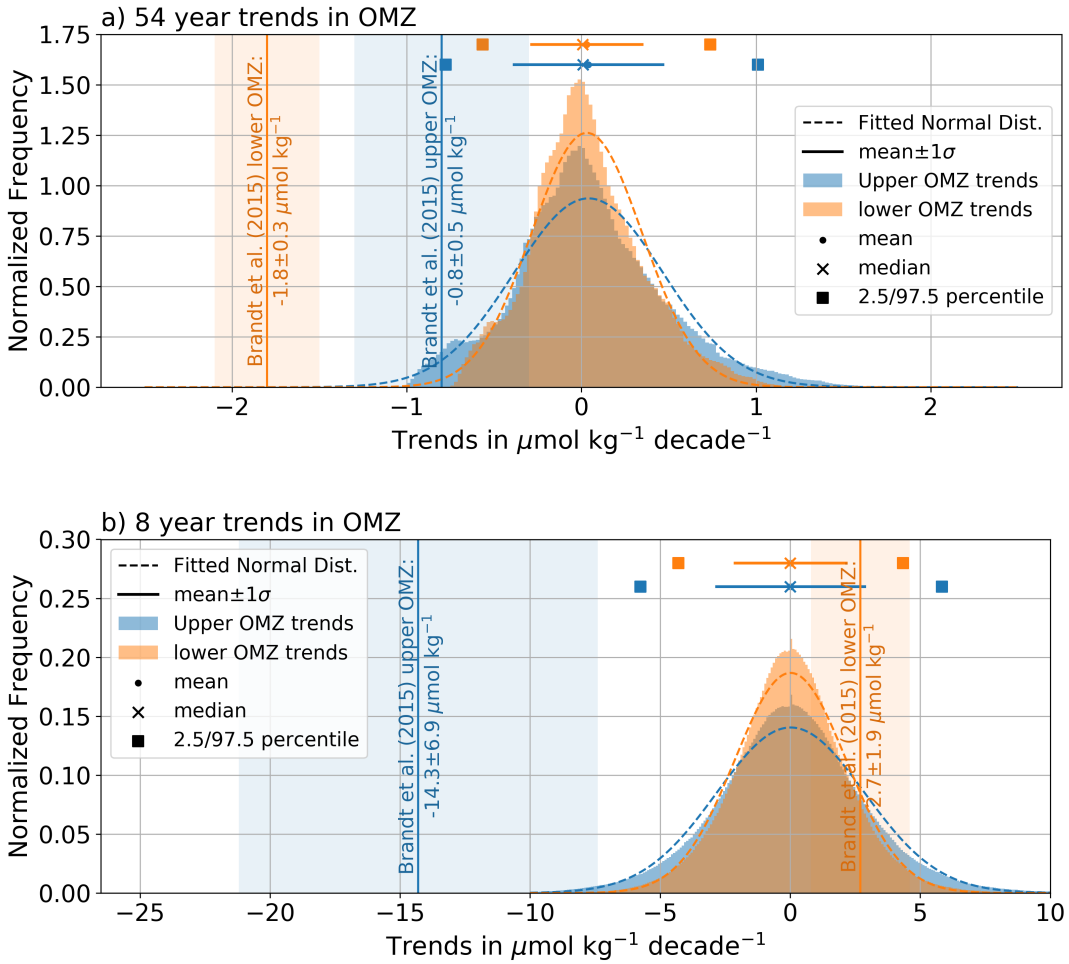

Figure 3.19: Histogram of all linear trends of the tracer concentration in 26 °W-20 °W and 9 °N - 15 °N over a time period of (a) 54 years and (b) 8 years for the last 240 years of model integration. The tracer fields were projected pointwise onto two dimensional mean oxygen fields similar to Fig. 3.18 retrieved from the World Ocean Atlas (*Garcia et al.*, 2014) (see Fig. 1.1 for details) for the depth ranges of 150 m to 300 m and 350 m to 700 m, corresponding to the depths of the trends analysis by *Brandt et al.* (2015) for the upper and lower OMZ (Fig. 1.3). Their trends and corresponding uncertainties over the periods 2006-2013 and 1900-2013 are included. For the latter, most data is available between 1960 and 2013 and is hence compared with a 54 year period.

15 °N and 26 °W-20 °W) an increase in mean oxygen in the lower OMZ between 2006 and 2013. However, *Brandt et al.* (2015) also find that the lower OMZ is marked by a decrease in oxygen over much longer time scales. Even though the authors state that the negative trends apply to the period 1900-2013, almost all data is available only after 1960. Hence, to also compare the observed trends in the entire OMZ with the

modelled trends, two periods are analysed: a 54 year period, corresponding to the years 1960-2013, and an 8 year period, corresponding to 2006-2013. To scale the modelled tracer field to concentrations in μmol kg^{-1}, a scaling factor similar to the one given in Fig. 3.18a is used. It is again a ratio of the mean observed oxygen concentration from the World Ocean Atlas (see Fig. 1.1 for further detail) and the modelled mean tracer concentration, but it is two-dimensional and spans the area 9 °N-15 °N and 26 °W-20 °W and varies in latitude and longitude. The World Ocean Atlas database allows for scaling the modelled fields individually to the upper and lower OMZ, by averaging the oxygen field in the depth range between 150 m to 300 m for the upper and between 350 m to 700 m for the lower OMZ.

Figure 3.19 shows the total distribution of the pointwise trend calculation for the area 9 °N to 15 °N and 26 °W to 20 °W in the ETNA OMZ. Overall higher oxygen concentrations in the shallow OMZ compared to the lower OMZ lead to higher scaling factors and hence wider trend distributions for both the 54 yr and 8 yr period. The distribution for the 8 yr trends again resemble a normal distribution centred around 0 μmol kg^{-1} per decade with slightly positive excess kurtosis (Fig. 3.19b) . About 95 % of the linear trends lie within $\pm 5\,\mu$mol kg^{-1} per decade. The distribution for the 54 yr trend period also shows a resemblance to a normal distribution, but with positive excess kurtosis and uneven tails, even though the mean and median values are close to 0 μmol kg^{-1} per decade. On the 8 yr time scale, the observed mean oxygen increase for the lower OMZ is well within 95 % of the pointwise modelled trends, which range within about $\pm 1\,\mu$mol kg^{-1}. The drastic observed oxygen decrease between 2006 and 2013 in the upper OMZ (c.f. Fig. 1.3) is however far outside the range. On the 54 yr time scale, the picture is reversed (Fig. 3.19a). While the observed upper OMZ decrease and its uncertainty is marginally covered by the modelled trends, the long-term oxygen decrease in the lower OMZ is well outside the modelled range.

3.7 Influence of the tracer consumption term

The analysis so far has shown that a more or less realistic tracer minimum region is established in the location of the ETNA OMZ. However, spatial gradients in the tracer concentration appear too weak. This becomes obvious in the comparison between the modelled and observed fields (Fig. 3.18a). The need to use a scaling factor that is larger towards the equator than further north implies that the meridional gradient in modelled concentrations is too weak. One reason for this could be the nature of the consumption. As it damps the tracer in proportion to the local tracer content, it tends to weaken lateral gradients.

In this section a new model run in the Atlantic will be shown, in which the tracer consumption term $-JCh$ is exchanged against a tracer consumption term $-FhQ$, where $Q = 3.25 \times 10^{-10}$ s^{-1} is a spatially and temporally uniform consumption time scale. F is either 1 or 0 depending on the local tracer concentration. If the local tracer concentration is below the threshold level of 0.2, the tracer consumption is turned off by setting $F = 0$. This method is an attempt to realistically represent the biological reaction to low oxygen concentrations. The model with the adapted advection-diffusion component is again integrated for 400 years. Averaged over the last 240 years of model integration, the basinwide average tracer concentration is 0.52 with a standard deviation of 0.56 %. Hence, by deliberately choosing Q as half the value of J the overall tracer content is set to be very similar compared to the model run in the Atlantic basin with the tracer dependent consumption scheme (see Sec. 3.1).

As the shallow water model remains unchanged, the exactly identical dynamical fields are produced, transporting the tracer through the basin. Figure 3.20a shows the thickness-weighted mean tracer concentration averaged over the last 80 years of model integration. The general distribution of tracer is very similar to the one shown in Fig. 3.6b. It again features the region of minimum tracer concentration in the ETNA. When

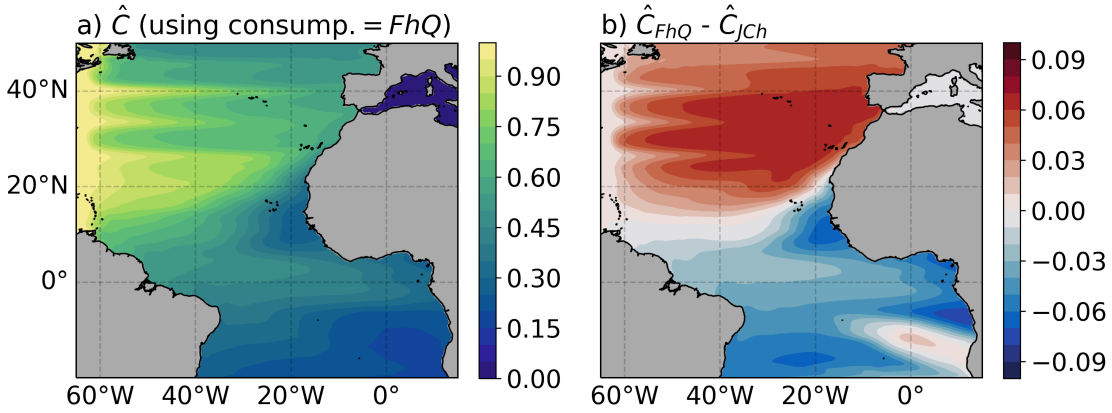

Figure 3.20: a) Thickness-weighted tracer concentration for the last 80 years of model integration using the consumption term independent of the tracer concentration above the threshold value $F = 0.2$. b) Difference between the thickness-weighted tracer concentrations for the last 80 years of model integration, using the two consumption schemes ($FhQ - JCh$).

looking at the differences between the two model runs (Fig. 3.20b), it becomes obvious that most of the North Atlantic is marked by higher tracer concentrations, while the equatorial regime features slightly lower values with the new consumption scheme. One striking feature is that employing the tracer independent consumption scheme leads to an intensified tracer minimum region with values lowered by 0.06. Still, they are above the threshold value of 0.2, indicating a surplus of ventilation. The region of intensified minimum tracer concentration goes along with an intensification of tracer gradients along its edge (Fig. 3.20b and 3.21a). For example, equatorial tracer concentrations are lower by only 0.03, hence leading to a slightly strengthened meridional gradient along the southern edge of the region with minimum tracer. However, the factor to scale the modelled tracer concentrations onto World Ocean Atlas oxygen concentrations along 23 °W exhibits values ranging between 235 μmol kg^{-1} to 285 μmol kg^{-1} depending on latitude (not shown). Thereby, similar to Fig. 3.18a, the maximum is again located at 7 °N while the minimum scaling factor is found around 12 °N. Hence, apart from an overall increase in scaling factors, the tracer independent consumption scheme does not lead to a homogenization of required scaling factors.

Plotting the thickness-weighted mean tracer concentration and its variability along

the 23 °W section shows again the stronger minimum in tracer concentration (Fig. 3.21a). Along 23 °W, interannual to multidecadal tracer variability is of slightly stronger amplitude (Fig. 3.21b), while the general structure is similar to the one presented in Fig. 3.17f. Both, the higher observed interannual to multidecadal vari-

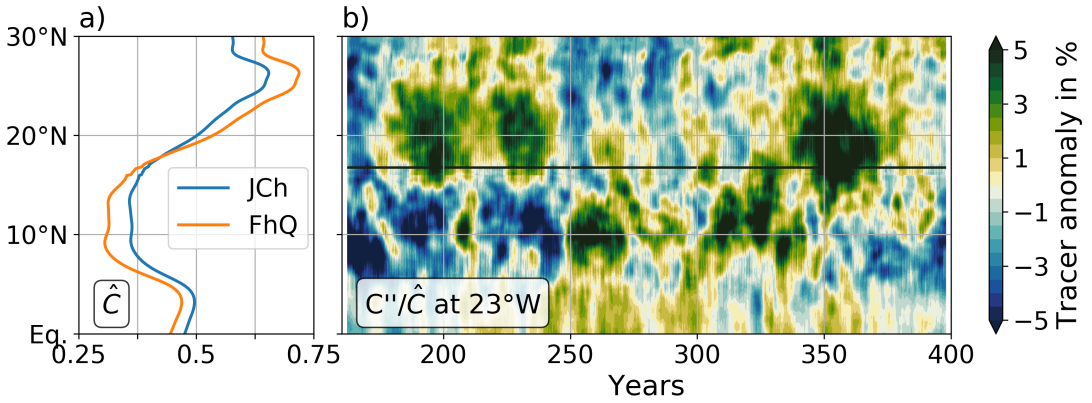

Figure 3.21: Same as Fig. 3.17e,f but using the consumption scheme independent of local tracer content. In a), the mean tracer concentration along 23 °W from the model run with the tracer dependent consumption scheme is included for comparison.

ability and the overall higher scaling factors due to lower tracer concentrations in the region of minimum tracer lead to wider trend distributions when comparing to observed trends by *Hahn et al.* (2017) or *Brandt et al.* (2015). Wider decadal trend distributions than shown in Fig. 3.18b-f make the decadal trends observed by *Hahn et al.* (2017) even more likely to be realisations of the modelled trends. In contrast, the increased variability on multidecadal time scales is still not capturing the observed long-term deoxygenation of the lower OMZ (*Brandt et al.*, 2015) (not shown).

Chapter 4
Discussion

Before delving into the discussion of the results presented in the section above, the main findings will be listed in a condensed form below. These will yield the basis for the subsequent discussion, which will be separated into three parts. Each part will be related to one of the research questions posed in Section 1.3.

1. The 1.5 layer non-linear shallow water model employed in this study is able to produce latitudinally alternating zonal current bands. Off the equator they rectify through westward propagating non-linear eddies that are formed by the break-up of annually generated baroclinic Rossby wave fronts due to resonant triad interactions. The meridional scale of the jets is set by the wavelength of the most unstable secondary waves in the resonant triad instability process and is larger than the Rossby radius of deformation and the Rhines scale. Theory predicts that the location of the break-up of the Rossby wave front and the wavelengths of the secondary waves are dependent on the amplitude of the generated primary Rossby waves.

2. In the rectangular basin the off-equatorial zonal current bands, or LAZJs, appear west of the Rossby wave front break-up. In the Atlantic basin zonal jets are also rectified east of the break-up of the Rossby waves, i.e. in the region of the ETNA OMZ. Hence, it is likely that the geometry of the African coast plays an important role for the rectification of the zonal jets.

3. The model is capable of producing a tracer minimum zone off the Mauritanian coast, which is in general spatial agreement with the observed ETNA OMZ.

The tracer minimum region is situated between an equatorial tracer tongue and higher tracer values to the north-west. The principal gradient along the north-western boundary is directed along an axis running from the north-east to the south-west, crossing the Canary and Cape Verde Islands, corresponding to the general orientation of the Rossby wave fronts.

4. Calculating a tracer budget reveals that the zonal and meridional (Eulerian) mean advective flux convergence are the dominant means of tracer redistribution. Even though the model basins are filled with eddies, the mean advective flux convergence largely outweighs the eddy flux convergence. The total mean advective flux convergence, with jet-like structures, is mainly balanced by the meridional eddy mixing term, which is both of advective and diffusive nature, and the consumption term, which acts basin-wide in proportion to the local tracer content. At the edge of the tracer minimum region, at about 23 °W, all flux convergences, also with it the mean advective flux convergence, drop in strength, leading to the weaker ventilation, and hence the tracer minimum.

5. Even though the model is driven by an annual period forcing, the latent zonal jets show some interannual variability, in the form of intensification/weakening of the mean currents or latitudinal meandering. The off-equatorial tracer field shows variability on interannual to multidecadal time scales as well. In the region of the tracer minimum zone, this variability shows some increasing power with ever longer time scales, but no dominant periodicity is discernible. Establishing a direct relation between the zonal jet variability and the tracer content in the OMZ is however difficult.

6. Most observed oxygen trends in the lower OMZ along 23 °W or in the entire ETNA OMZ on interannual to decadal time scales are possible realizations of the modelled tracer variability. However, the trends established by *Brandt et al.* (2015) for the entire lower OMZ on multidecadal time scales are outside the

range of the modelled trends. The picture is reversed for the upper OMZ, where the long-term (1900/1960-2013) decrease in oxygen is a possible realization of the modelled trends, whereas the drastic decrease in oxygen in 2006-2013 is not. Under the assumption that the chosen comparison method between modelled and observed fields is valid, this result may have two implications. Firstly, even though the shallow water model is able to reproduce the interannual to decadal variability of the lower OMZ quite well, it fails to realistically reproduce the power of the intrinsic multidecadal variability in the observed lower OMZ. The other implication might be that the observed oxygen variability in the lower OMZ on multidecadal time scales carries a background trend due to extrinsic forcing, for example of anthropogenic nature, which is not accounted for in the idealized model set-up.

4.1 Characteristics and realism of the zonal jets

The zonal jets produced in the shallow water model are the rectification of westward propagating eddies or Rossby waves. As we are only dealing with a 1.5 layer model, all dynamics in the basin are purely baroclinic with mode one structure. In the real ocean or in OGCMs the vertical structure of LAZJs appears to be strongly dependent on the geographical location and the large-scale background flow. For example, in an OGCM of the (north-) western Atlantic, *Kamenkovich et al.* (2009b) have identified the vertical structure of the time mean zonal velocity field, which features zonal jets to be largely dominated by the barotropic and the first two baroclinic modes. The observations presented in *Brandt et al.* (2015) show the off-equatorial LAZJs to carry a barotropic signature below the thermocline, with vertically almost constant zonal velocity signals in the upper 1000 m. Hence, it is questionable whether a purely first baroclinic mode model is, despite its instructive simplicity, an appropriate tool to study the dynamics of the zonal jets, as previously done for example by *Marshall*

et al. (2013) or *Qiu et al.* (2013a). The latter yield an argument for the usage of the 1.5 layer model, by studying the so-called Pacific NEUC jets (*Qiu et al.*, 2013b), which are zonal current bands with eastward flow centred at 9 °N, 13 °N and 18 °N, reaching from below the thermocline down to 1500 m depth. In their region the zonal flow variability exhibits a first baroclinic mode vertical structure, implying that the NEUC jets would even reach well into the thermocline if it was not for the superposition of the strong wind driven westward Pacific NEC. Guided by this finding, the idealized first baroclinic mode model appears to be a valuable tool in understanding the zonal jet mechanisms and their impact on the tracer transport. In their study of the flow field at 1000 m depth in the ETNA, *Chu et al.* (2007) identified the imprint of annual and semi-annual baroclinic Rossby waves, generated either by modulation in the meridional wind stress near the African coast or equatorial Rossby and Kelvin waves. Following their analysis, the second baroclinic mode also seems to carry a large importance for the off-equatorial Atlantic flow field. Hence, an extension of the shallow water model to at least two or three layers, thus including the barotropic mode and allowing for further baroclinic modes, would be an instructive extension of the model set-up. Furthermore, a sufficiently high resolved three-dimensional ocean general circulation model could be used to study the LAZJs dynamics.

Rooted in the purely annual period forcing and the single mode set-up, the non-linear eddies generated by the triad instability mechanism propagate regularly aligned along lines of latitude. Both the mean and the standard deviation of the zonal velocity signal remain constant over ever larger averaging periods (Fig. 3.9). This finding is in stark contrast to the zonal jets observed in the real ocean. There, both the zonal jet strength and the standard deviation of the velocity field decrease with increasing averaging periods. For both quantities *Schlax and Chelton* (2008) detected a T^{-1} relation, with T being the averaging period, in an artificially generated random eddy field with realistic eddy properties. Even though *Buckingham and Cornillon* (2013) identified a somewhat slower decay for observed surface eddy fields, both findings are

very different from the results presented here. Introducing a superposition of a semi-annual and annual period forcing could lead to more realistic results, by shaking up the generated eddy field.

Another aspect of the time mean velocity field analysed in the present study is the meridional scale of the zonal jets. As already shown by *Qiu et al.* (2013a) the eddy generation mechanism through non-linear triad instability plays a crucial role in setting the size of the generated baroclinic eddies, which in the end rectify to the zonal jets. This eddy formation process is profoundly different to baroclinic instability, which is a typical oceanic process forming mesoscale eddies away from lateral boundaries. Thereby, the length scale of the fastest growing mode roughly corresponds to the baroclinic Rossby radius of deformation, setting the size of the developing mesoscale eddies. While large-scale Rossby waves have been shown to succumb to baroclinic instability in simplified two-layer models (*LaCasce and Pedlosky*, 2004; *Isachsen et al.*, 2007; *O'Reilly et al.*, 2012), the 1.5 layer model employed in the present study does not support this instability mechanism. The single active layer can solely allow for barotropic instability in the case of sufficiently large lateral shear. Fig. 3.10a shows that the meridional scale of the eddies/zonal jets does indeed not match with the baroclinic Rossby radius of deformation. It is however good to note that this direct comparison is difficult as briefly described in the following. The observed dominant meridional wavelength associated with zonal jets in the global ocean is roughly around 400 km (*Maximenko et al.*, 2005, 2008; *Buckingham and Cornillon*, 2013). Assuming that the zonal jets are completely rectified by eddies, this size matches well with the dominant wavelength associated with eddy activity for example in the North Atlantic (*Eden*, 2007) or the globally averaged typical eddy radius of 90 km observed with satellite altimetry *Chelton et al.* (2011). Even though the typical eddy radii decrease away from the equator, they are observed to largely exceed the local baroclinic Rossby radii of deformation, which are around 30 km at middle and higher latitudes (*Chelton et al.* (1998), Fig. 3.10b). *Chelton et al.* (2011) link this apparent discrepancy in

length scales to the up-scale transfer of energy in a geostrophically turbulent flow field after the generation of eddies through baroclinic instability (see Section 1.2, *Charney* (1971)). Hence, the inverse energy cascade and the conceptual scale difference between meridional wavelengths and eddy radii (factor four difference) complicate the direct comparison between the Rossby radius of deformation and the dominant meridional wavelength of the zonal jets as done in Fig. 3.10a. Still, the diagnosed dominant meridional wavenumber of the eddies or zonal jets of 700 km, which corresponds to an eddy radius of 175 km, is much larger than the off-equatorial Rossby radius of deformation. Despite a potential up-scale energy transfer, this discrepancy indicates that the Rossby radius of deformation does not play an important role. As the Rhines scale is even smaller than or equal to the Rossby radius of deformation (Fig. 3.10b), it also does not seem to play an important role in determining the dominant length scales in the basin.

Despite their mismatch with the observed dominant meridional wavelength, the theoretically derived Rossby radius and Rhines scale might still be helpful in understanding the generation of zonal jets around the equator. In the study of a flow field of decaying geostrophic turbulence, *Theiss* (2004) identified an anisotropy in a geostrophically turbulent two-dimensional flow, favouring zonal over meridional flow, under the condition that the Rhines scale is smaller than the Rossby radius of deformation. In contrast, regions in which the Rhines scale is larger than the Rossby radius of deformation feature an isotropic eddying field. These findings are backed by the observational and modelling study of *Eden* (2007) for the North Atlantic, with the critical latitude between both regimes located at 30 °N. In lower latitudes, i.e. where the Rhines scale is smaller than the Rossby radius of deformation, Rossby waves are found to introduce the anisotropy to the flow field as predicted by the classical idea of geostrophic turbulence on a β-plane (*Rhines*, 1975). When temporally averaged, this anisotropic flow could rectify to latitudinally alternating current bands without the need for the break-up of the Rossby wave fronts. This finding could help to understand why the

zonal jets are also observed around the equator east of the break-up line of the Rossby wave fronts (Fig. 3.5c). However, in a fully turbulent regime the meridional scale of the mean zonal jets should correspond to the Rhines scale (*Rhines* (1975)), independent of the ratio between Rossby radius and Rhines scale. As the meridional scale of the zonal jets corresponds to the wavelength of the most unstable secondary wave from the triad instability mechanism, rather than the Rhines scale, we conclude that the flow field in the presented model is not fully turbulent.

The zonal jets generated in the Atlantic basin east of the Rossby wave break-up seem to be linked to the geometry of the African coastline. There, the curvature of the coast and distinct capes introduce initial disturbances to the annual Rossby waves. Indeed, eastern boundaries have been identified to radiate instabilities into the ocean (*Hristova et al.*, 2008) or to act as a hotspot for eddy-formation (e.g. *Thomsen et al.* (2016)), including the ETNA (*Schütte et al.*, 2016). Thereby distinct features in the topography lead to preferred eddy generation sites. Resulting from meanders in an eastern boundary current, zonal jets have been observed to rectify (*Centurioni et al.*, 2008). The hotspots observed in the real ocean however do not necessarily compare to the ones visible in our model. Bathymetric features beneath the surface, such as the shelf break, might be dynamically more important than the actual coastline.

Multiple functions or characteristics have been ascribed to the zonal jets. As already described in Section 1.2, *Marshall et al.* (2013) point out the need for an eastward mass flux to balance the westward transport of mass associated with the Stokes drift of westward propagating Rossby waves and eddies. This result implies that the zonal jets must be a real feature of the mean ocean circulation. Another role of the zonal jets was proposed by *Qiu et al.* (2013a). In their study, a mean flow field similar to the zonal jets could be diagnosed by using the turbulent Sverdrup balance (*Rhines and Holland*, 1979)

$$\overline{\mathbf{u}} \cdot \nabla \overline{q} = -\overline{\mathbf{u}' \cdot \nabla q'}. \tag{4.1}$$

The authors hence conjecture that the zonal jets are likely to be driven by eddy potential vorticity flux convergences across the mean potential vorticity gradient. To obtain a more consistent picture of this relation diagnosed in a layered system, the shallow water model employed in this study could be used by using the thickness-weighted averaged version of the vorticity equation (see Appendix A.2 for further detail).

4.2 Representation of the ETNA OMZ and its ventilation

The most important role of the zonal jets in the context of this study is their impact on transporting tracers throughout the ocean basin. Driving a flow field that only features zonal jets in the temporal mean is thereby sufficient to produce a region of minimum tracer concentration which is in good agreement with the ETNA OMZ (Fig. 3.6). Hence, there seems to be some sort of "shadow zone", which tracer enriched water cannot easily reach. This result is somewhat surprising as the classical theory of the ventilated thermocline, which predicts the existence of the shadow zone (*Luyten et al.*, 1983), requires at least two moving layers above a deep ocean at rest. A dynamical expression of these shadow zones is the anomalously high potential vorticity (e.g. *Malanotte-Rizzoli et al.* (2000)), making it difficult for flow to enter this area, as potential vorticity needs to be conserved along streamlines of subducted geostrophic flow. As the shallow water model employed in this model only features one layer, no outcropping of a density surface associated with subduction is possible. Hence, the potential vorticity barrier cannot be established. At least 2.5 or 3 layers would be required to reproduce a classical shadow zone. Still, the generation of annual Rossby waves is able to set up a region of minimum tracer. Due to the curvature of the Rossby wave fronts, tracer is transported north-eastward in phases of eastward flow, thereby

feeding on tracer provided by the equatorial tracer tongue and by the off-equatorial eddy field (Fig. 3.1). The Rossby wave fronts serve as the flow guides, redirecting the tracer around the region of minimum tracer (Fig. 3.1,3.2). Hence, it is not surprising that the north-western boundary of the region of minimum tracer in the Atlantic is closely linked to the stable Rossby wave fronts (Fig. 3.2c,f and Fig. 3.6b). The southern edge of the region with minimum tracer is marked by an equatorial tracer tongue, which is also observed in the real tropical Atlantic. There, the oxygen tongue is linked to strong zonal advection associated with the strong zonal equatorial current system (see Fig. 1.2) (*Brandt et al.*, 2008). This mechanism is somewhat different from the eastward tracer transport by annual equatorial Kelvin waves developing in the shallow water model presented here. A comparison of modelled tracer concentrations and measured oxygen concentrations between 500 m to 800 m along 23 °W shows that the model is generally capable of reproducing the general oxygen distribution quite well (Fig. 3.18a). However, there are some weaknesses. The fact that scaling the modelled concentrations to the World Ocean Atlas data requires a larger scaling factor towards the southern edge than in the centre of the OMZ, implies that the modelled meridional gradient of tracer concentrations is too weak. One reason for this could be the tracer consumption term, which damps the tracer concentration with an amplitude proportional to the local tracer content (c.f. Eq. 2.7 or Fig. 3.15k). Hence, this term leads to a general reduction of tracer gradients. Using a different simplified consumption scheme independent of the local tracer content results in stronger tracer gradients around the tracer minimum region, but still exhibits the requirement of a spatially varying scaling factor (see Section 3.7).

The tracer budget (Fig. 3.15) reveals that for the tracer minimum region of the ETNA, the main balance is given by the tracer consumption and the supply through the total advective flux convergence. It is reassuring to see that there is hardly any mean impact of the forcing in this region. Also, the total diffusive flux convergence from the explicitly implemented diffusion term has only a minor impact on the ETNA

OMZ. Only north of 25 °N, this term seems to play a more important role in the diffusive meridional redistribution of tracer between the strongly developed zonal jets. A closer analysis reveals that the main terms contributing to the total advective flux convergence are given by the total mean advective flux convergence and the meridional component of the eddy mixing term. At first sight, it is counter-intuitive that the eddy advective flux convergence plays hardly any role in the distribution of tracer through the basin, even though eddies densely populate at least the western part of the basin. However, the weakness of the eddy advective flux convergence highlights the fact that the zonal jets are rather stable and show only limited variability regarding their strength and position. As a result, the eddy contribution is ascribed to the mean advective flux convergence. Further, *Marshall et al.* (2013) pointed out that the meridionally integrated zonal eddy advective flux associated with the bolus velocity is directed westward, i.e. directed up the mean zonal tracer gradient. This generally agrees with our finding that the eddy advective flux convergence does not largely contribute to the eastward spreading of the tracer.

The eddy mixing term has been analysed more closely, revealing that it consists of an advective and a diffusive part, of which the latter is almost exclusively directed down the mean tracer gradient. This result is comforting, as the diffusive part of the eddy mixing term is hence likely to be a truly diffusive flux. Rotational eddy fluxes, which are next to diffusive and advective eddy fluxes their third possible nature (*Greatbatch*, 2001; *Eden et al.*, 2007), are likely to play only a minor role. The advective part of the eddy mixing term can be added to the mean/eddy advective flux convergence to form the total supply of tracer by advective fluxes. The diffusive part of the eddy mixing term is uniquely responsible for the eddy diffusive tracer transport. Following these considerations, the terms of the tracer budget estimated by *Hahn et al.* (2014) are comparable to the terms obtained in this study. The main term balancing the oxygen consumption in the deep OMZ is identified by *Hahn et al.* (2014) as the isopycnal meridional eddy supply. Following the reasoning above, this term must correspond to

the diffusive part of the meridional component of the eddy mixing term. Interestingly, similar to the meridional alternating structure of the eddy mixing term, *Hahn et al.* (2014) also identify a meridional alternating structure in the meridional eddy-driven oxygen supply along 23 °W (see their Fig. 13). Of similar importance in the *Hahn et al.* (2014) budget is the supply via the combination of advective and zonal eddy flux convergences, which they estimate as the residual of the oxygen budget. This residual term must then correspond to the sum of mean and eddy advective flux convergence with the addition of the advective part of the eddy mixing term. The third term diagnosed by *Hahn et al.* (2014) to supply substantial amounts of oxygen to the lower ETNA OMZ is diapycnal mixing. As the shallow water model lacks a vertical axis, the advection-diffusion model does not account for this term.

Before closing the discussion of the budget terms, it is important to note that the elevated contributions of the eddy mixing term and the total mean advective flux convergence in proximity of the ETNA tracer minimum region lie in the regime of the still stable Rossby wave fronts (c.f. Fig. 3.2c). Hence, the tracer flux driven by the mere propagation of the annual Rossby waves with some potential modulations superimposed is enough to yield this alternating structure in the mean advective flux convergence and eddy mixing term. Further analysis of the dynamics behind their rectification is required to understand the OMZ ventilation.

4.3 Interannual to multidecadal variability of tracer concentrations

A tracer is set to represent oxygen by introducing a consumption term mimicking biological consumption through respiration. Further, the source was set along the western boundary mimicking the export and spreading of oxygen-enriched deep water by the deep western boundary current. Both terms are associated with a specified

time scale. As the time scale associated with the source term γ is chosen to be very short, i.e. about 8 days at its maximum, the tracer field is quickly restored to 1 along the western boundary. This guarantees that there is almost always the same amount of tracer that can be exported by the flow field. Indeed, the variability of the entire tracer inventory is rather small for every model run (Fig. 3.4). Hence, it is unlikely that the variability observed in the region of minimum tracer is related to the amount of tracer that is introduced at the western boundary. However, the consumption time scale J is rather long at 50 years. This large value is chosen to allow for the spreading of the tracer through the entire basin, before being damped away. It is twice the time scale estimated by *Van Geen et al.* (2006) by constraining a one-dimensional advection-diffusion model to observed chlorophyll data in the North Pacific OMZ. Their diagnosed value has already been used in the advection-diffusion models by *Brandt et al.* (2010, 2012). *Karstensen et al.* (2008) and *Hahn et al.* (2014) estimate the biological consumption rate in the lower OMZ of the ETNA to be about $4\,\mu\mathrm{mol\,kg^{-1}yr^{-1}}$. Dividing a mean lower ETNA OMZ oxygen concentration of roughly $60\,\mu\mathrm{mol\,kg^{-1}}$ by this consumption rate yields a time scale of 15 years. Hence, both time scales, the one estimated by *Van Geen et al.* (2006) and the one used in our study, are much longer, at least for the region around ETNA OMZ. As the consumption term acts as a restoring force on the tracer concentration, it is important to keep in mind that this choice of the consumption time scale has an influence on the tracer variability. Using a larger source region, i.e. introducing more tracer into the model, could potentially allow for the usage of a shorter consumption time scale (15 to 25 years), while still allowing for the tracer to spread through the entire basin.

In Section 3.6, the modelled trends in tracer concentration in the OMZ are compared with estimated trends in oxygen concentrations from observations. The main finding is that despite the purely annual forcing, interannual to decadal variability in the lower OMZ is reproduced by the shallow water model, whereas multidecadal variability is not. The trends obtained by *Brandt et al.* (2015) and *Hahn et al.* (2017) are based on

shipborne point measurements and mooring time series of oxygen concentrations. The big effort associated with obtaining these datasets results in quite large gaps, adding a large uncertainty at least to the multidecadal trends. Also the tracer trends estimated from the shallow water model are prone to uncertainty. Especially the employed scaling factor has a big influence on the width of the trend distributions shown in Fig. 3.18 and 3.19. It is discomforting to use a scaling factor varying for example between 205 μmol kg^{-1} to 245 μmol kg^{-1}, i.e. by roughly 16 %, along 23 °W. Using a spatially constant scaling factor would however lead to a false basis of comparison. A way to circumnavigate these complications is by achieving a better representation of the ETNA OMZ. Therefore, as discussed above, a stronger meridional gradient in tracer concentrations is required. The attempt to obtain intensified gradients by using a tracer independent tracer consumption scheme shows mixed results (Section 3.7). In this attempt the scaling factor ranges in amplitude between 235 μmol kg^{-1} to 285 μmol kg^{-1}, which is overall larger, hence leading to wider trend distributions than shown in Fig. 3.18 and 3.19. This sensitivity of the trend distributions to the modelled tracer concentrations questions the validity of the direct comparison with observed oxygen trends. However, assuming that the method for comparison is valid despite the mentioned difficulties, one could conclude that the observed long-term decrease in oxygen of the lower OMZ is a signature of an externally forced deoxygenation, as it is likely to be outside of the system's natural internal variability. Nonetheless, the shallow water model presented here is not the right tool to reject the null hypothesis of no long-term trend, as it features a lot of simplifications and shortcomings. For example, the variability throughout the basin is purely driven by an annual period forcing and is certainly lacking important periodicities to generate a realistic tracer variability.

On interannual to interdecadal time scales, climate modes such as the Atlantic Zonal Mode (AZM) or the Atlantic Meridional Mode (AMM) (*Chang et al.*, 2006; *Kushnir et al.*, 2006) are hypothesized to influence the oxygen variability in the ETNA

OMZ (*Hahn et al.*, 2017). In fact, by having a signature in the surface wind fields, these climate modes could affect the generation and amplitude of annually excited Rossby waves, which have already been shown to be closely linked to the dynamics of the NECC (*Hormann et al.*, 2012). Building on the results obtained from the study presented here, variations in the amplitude of the annual Rossby waves could also affect the LAZJs and their impact on the ventilation of the OMZ. Further research would need to be conducted to back this hypothesis with a complete physical line of argument.

Chapter 5
Summary and conclusion

In this study, the ventilation of the eastern tropical North Atlantic (ETNA) oxygen minimum zone (OMZ) is studied using a shallow water model driven by an annual period forcing term in the continuity equation. The model domain is set to represent an ocean basin stretching from 20 °S to 50 °N with a zonal extent of 80 °. For both rectangular and Atlantic basin geometry, the forcing with an equatorial Kelvin wave structure excites (off-) equatorial Kelvin and Rossby waves. The off-equatorial Rossby wave fronts propagate westward through the basin before growing unstable due to non-linear triad instability. Resulting westward propagating eddies rectify to latitudinally alternating zonal jets (LAZJs). In the Atlantic basin also the structure of the African coastline leads to modulations of the annual Rossby wave fronts, so that mean zonal jets are rectified. The shallow water model is coupled to a simplified advection-diffusion model in which a tracer is set to mimic oxygen. The tracer is found to be transported along the Rossby wave fronts, forming a region of minimum tracer concentrations corresponding well to the ETNA OMZ in its location. By establishing a tracer budget, the ventilation mechanisms of the region with minimum tracer concentration are analysed. The main tracer supply pathways are found to be via the mean advective flux convergence and the meridional component of the eddy mixing term. The diffusive part of the latter is thereby found to be a truly diffusive flux, making it possible to relate these findings directly to the oxygen budget established by (*Hahn et al.*, 2014). Despite the annual period forcing, interannual to multidecadal variability is excited off the equator. Modelled decadal trends are found to agree with observed decadal trends in the lower ETNA OMZ. A long-term decrease in oxygen

concentrations (*Brandt et al.*, 2015) in the lower OMZ is however not reproduced by the model. The picture is reversed for the upper OMZ, where the multidecadal variability is captured by the shallow water model. In contrast, the sharp decrease in oxygen in the upper ETNA OMZ observed between 2006 and 2013 is not.

All in all, this study shows that even in a strongly idealised dynamical model coupled to an advection-diffusion model a region of minimum tracer can be established in the ETNA. Despite lacking a vertical axis, which in the classical theory is essential for the generation of the ETNA OMZ (*Luyten et al.*, 1983; *Karstensen et al.*, 2008), the shallow water model is capable of creating a region of minimum tracer. Annual Rossby waves play thereby a large role. It has already been observed that the seasonal cycle of the NECC is linked to these Rossby wave dynamics (*Hormann et al.*, 2012) and it is intriguing to link parts of the LAZJs found beneath the thermocline to similar mechanisms. In fact, the LAZJs observed in repeat shipborne measurements along the 23 °W line have not yet been shown to be a permanent feature or a mere rectification of transient features. The findings of *Marshall et al.* (2013) however imply that the zonal jets need to be present in the Eulerian mean to balance the westward mass transport associated with eddies and Rossby waves.

The non-linear shallow water model seems to be a useful tool in studying the processes involved in the ventilation of the ETNA OMZ. The main terms contributing to the supply of oxygen diagnosed by observations are reproduced by the idealized model. Extending the used model to feature the barotropic and more baroclinic modes and forcing the model with different superimposed periodicities promise to be instructive ways forward. A fully three dimensional ocean general circulation model with sufficiently high resolution would further provide valuable insights concerning the characteristics of the zonal jets and their impact on the ETNA OMZ ventilation.

Appendix

A.1 Implementing the model equations

A.1.1 Implementation of the dynamical equations

Figure A.1: The Arakawa-C grid, including a landmass located in the domain. The dashed grey lines mark the boundaries of grid cells carrying the same indices.

The non-linear shallow water model used in this study has already been used in its linear version for example in the studies of *Greatbatch et al.* (2012) and *Claus et al.* (2014). The dynamical equations in spherical coordinates are discretized with finite

differences on an Arakawa-C grid (Fig. A.1) (*Arakawa*, 1972), yielding the following set of equations for u, v and η at the zonal and meridional grid indices i and j, respectively:

$$\delta u|_u^{i,j} = q|_u^{i,j} V|_u^{i,j} - \frac{E|_\eta^{i,j} - E|_\eta^{i-1,j}}{r\Delta\lambda \cos\vartheta|_u^j} + M_u|_u^{i,j} + F_u|_u^{i,j} \tag{A.1a}$$

$$\delta v|_v^{i,j} = -q|_v^{i,j} U|_v^{i,j} - \frac{E|_\eta^{i,j} - E|_\eta^{i,j-1}}{r\Delta\vartheta} + M_v|_v^{i,j} + F_v|_v^{i,j} \tag{A.1b}$$

$$\delta\eta|_\eta^{i,j} = -\frac{1}{r\cos\vartheta|_\eta^j}\left(\frac{U|_u^{i+1,j} - U|_u^{i,j}}{\Delta\lambda} + \frac{V|_v^{i,j+1}\cos\vartheta|_v^{j+1} - V|_v^{i,j}\cos\vartheta|_v^j}{\Delta\vartheta}\right) + F_\eta|_\eta^{i,j} \tag{A.1c}$$

with the mass fluxes $U|_u^{i,j} = h|_u^{i,j} u|_u^{i,j}$ and $V|_v^{i,j} = h|_v^{i,j} v|_v^{i,j}$, and the energy density $E|_\eta^{i,j} = \left(u^2|_\eta^{i,j} + v^2|_\eta^{i,j}\right)/2 + g'\eta|_\eta^{i,j}$. The potential vorticity is defined as $q|_H^{i,j} = \left(f|_H^j + \zeta|_H^{i,j}\right)/h|_H^{i,j}$, where the relative vorticity is given by

$$\zeta|_H^{i,j} = \frac{v|_v^{i,j} - v|_v^{i-1,j}}{r\Delta\lambda\cos\vartheta|_H^j} - \frac{u|_u^{i,j} - u|_u^{i,j-1}}{r\Delta\vartheta} \tag{A.2}$$

On land points, i.e. where the depth $h|_H^{i,j} = 0$, the depth is set to the smallest possible positive number in double precision to avoid instabilities in the calculation of the potential vorticity. To move a variable from one grid to another, the variable is bilinearly interpolated in two or four point averages, depending on the relative position of the original and target grid. Due to the sphericity, the grid point values are weighted for the averaging process by their corresponding grid box area.

Solving the advection term in the zonal and meridional momentum balance as written above corresponds to the potential enstrophy conserving advection scheme of *Sadourny* (1975). It is computationally relatively fast in handling the non-linear terms, but it is not as sophisticated as the *Arakawa and Lamb* (1981) scheme, which conserves both energy and enstrophy. The conservation of these quantities is always based on the assumption of an infinitesimally small integration time step. The existence of lateral mixing required for model stability undermines the exact potential enstrophy conservation in any case.

A.1.2 Lateral mixing of momentum

The lateral mixing is implemented using the scheme of *Shchepetkin and O'Brien* (1996). For an ocean grid point (i.e. if $h|_u^{i,j}$ or $h|_v^{i,j}$ are larger than 0, respectively), the zonal and meridional components of lateral mixing are given by)

$$M_u|_u^{i,j} = \frac{A_h}{h|_u^{i,j}} \Bigg[-\frac{\iota|_u^{i,j}}{r \cos\vartheta|_u^j \Delta\lambda} \left(P_{\lambda\lambda}^{i,j} - P_{\lambda\lambda}^{i-1,j} \right) - \frac{\iota|_u^{i,j}}{r\Delta\vartheta} \left(P_{\lambda\vartheta}^{i,j+1} - P_{\lambda\vartheta}^{i,j} \right) + \frac{2\tan\vartheta|_u^j}{rO|_H} \left(P_{\lambda\vartheta}^{i,j+1} + P_{\lambda\vartheta}^{i,j} \right) \Bigg] \tag{A.3a}$$

$$M_v|_v^{i,j} = \frac{A_h}{h|_v^{i,j}} \Bigg[-\frac{\iota|_v^{i,j}}{r \cos\vartheta|_v^j \Delta\lambda} \left(P_{\lambda\vartheta}^{i+1,j} - P_{\lambda\vartheta}^{i,j} \right) - \frac{\iota|_v^{i,j}}{r\Delta\vartheta} \left(-P_{\lambda\lambda}^{i,j} + P_{\lambda\lambda}^{i,j-1} \right) - \frac{2\tan\vartheta|_v^j}{rO|_\eta} \left(P_{\lambda\lambda}^{i,j} + P_{\lambda\lambda}^{i,j-1} \right) \Bigg] \tag{A.3b}$$

where ι is the boundary condition factor, which is 1 in the ocean interior, but is set to 2 on the boundaries accounting for no-slip conditions. The value $O|_H$ is given by $\max\left(1, o|_H^{i,j} + o|_H^{i,j+1}\right)$, where $o|_H$ is 1, if the corresponding H grid point is an ocean grid point and 0 otherwise. In a similar fashion $O|_\eta$ is defined by $\max\left(1, o|_\eta^{i,j} + o|_\eta^{i,j-1}\right)$. The components of the viscous part of the momentum flux density tensor $\mathbf{P}$ on ocean grid points are given by

$$P_{\lambda\lambda}^{i,j} = h|_\eta^{i,j} \Bigg[-\frac{\iota|_\eta^{i,j}}{\Delta\lambda r \cos\vartheta|_\eta^j} \left(u|_u^{i+1,j} - u|_u^{i,j} \right) + \frac{1}{r} \left(\frac{\iota|_\eta^{i,j}}{\Delta\vartheta} + \frac{o|_v^{i,j+1} \tan\vartheta|_\eta^j}{O|_v} \right) v|^{i,j+1} + \frac{1}{r} \left(-\frac{\iota|_\eta^{i,j}}{\Delta\vartheta} + \frac{o|_v^{i,j} \tan\vartheta|_\eta^j}{O|_v} \right) v|^{i,j} \Bigg] \tag{A.4a}$$

$$P^{i,j}_{\lambda\vartheta} = h|^{i,j}_{H}\Bigg[- \frac{\iota|^{i,j}_{H}}{\Delta\lambda r\cos\vartheta|^{j}_{H}} \left(v|^{i,j}_{v} - v|^{i-1,j}_{v}\right) + \frac{1}{r}\left(\frac{\iota|^{i,j}_{H}}{\Delta\vartheta} + \frac{o|^{i,j}_{u}\tan\vartheta|^{j}_{H}}{O|_{u}}\right) u|^{i,j} + \frac{1}{r}\left(-\frac{\iota|^{i,j}_{H}}{\Delta\vartheta} + \frac{o|^{i,j-1}_{u}\tan\vartheta|^{j}_{H}}{O|_{u}}\right) u|^{i,j-1}\Bigg] \quad \text{(A.4b)}$$

with $O|_u = \max\left(1, o|^{i,j}_{u} + o|^{i,j-1}_{u}\right)$ and $O|_v = \max\left(1, o|^{i,j}_{v} + o|^{i,j-1}_{v}\right)$.

A.1.3 Time stepping scheme

The model is integrated using the 3^{rd} order Adams-Bashforth time stepping scheme, which carries a fourth order truncation error. This multistep method evaluates the variable α at timestep $k+1$ considering three previous timesteps following

$$\alpha|^{k+1} = \alpha|^{k} + \underbrace{\frac{\Delta t}{12}\left(23\left(\delta\alpha\right)^{k} - 16\left(\delta\alpha\right)^{k-1} + 5\left(\delta\alpha\right)^{k-2}\right)}_{AB(\alpha)} \quad \text{(A.5)}$$

where Δt is the length of a timestep and $\delta\alpha$ refers to the left hand sides of Eq. A.1 at the associated timestep. Their weighted average yields the increment $AB(\alpha)$ from timestep k to $k+1$. The first two timesteps are calculated using a simple Euler forward scheme.

A.1.4 Implementation of the tracer equation

The tracer equation is implemented using the tracer content Ch on the η grid as prognostic variable following

$$\delta[Ch]|^{i,j}_{\eta} = \text{adv.Ch}|^{i,j}_{\eta} + \text{diff.Ch}|^{i,j}_{\eta} - \text{relax.C}|^{i,j}_{\eta} + \text{forc.C}|^{i,j}_{\eta} \quad \text{(A.6)}$$

with the advection, diffusion, relaxation and forcing terms

$$\begin{aligned}
\text{adv.Ch}|_\eta^{i,j} = &-[Ch]|_\eta^{i+1,j} u|_u^{i+1,j} \frac{o|_u^{i+1,j} o|_\eta^{i+1,j}}{\left(o|_\eta^{i+1,j} + o|_\eta^{i,j}\right) r\Delta\lambda \cos\vartheta|_\eta^j} \\
&+[Ch]|_\eta^{i-1,j} u|_u^{i,j} \frac{o|_u^{i,j} o|_\eta^{i-1,j}}{\left(o|_\eta^{i-1,j} + o|_\eta^{i,j}\right) r\Delta\lambda \cos\vartheta|_\eta^j} \\
&-[Ch]|_\eta^{i,j+1} v|_v^{i,j+1} \frac{\cos\vartheta|_v^{j+1} o|_v^{i,j+1} o|_\eta^{i,j+1}}{\left(o|_\eta^{i,j+1} + o|_\eta^{i,j}\right) r\Delta\vartheta \cos\vartheta|_\eta^j} \\
&+[Ch]|_\eta^{i,j-1} v|_v^{i,j} \frac{\cos\vartheta|_v^{j} o|_v^{i,j} o|_\eta^{i,j-1}}{\left(o|_\eta^{i,j-1} + o|_\eta^{i,j}\right) r\Delta\vartheta \cos\vartheta|_\eta^j} \\
&-[Ch]|_\eta^{i,j} u|_u^{i+1,j} \frac{o|_u^{i+1,j} o|_\eta^{i,j}}{\left(o|_\eta^{i+1,j} + o|_\eta^{i,j}\right) r\Delta\lambda \cos\vartheta|_\eta^j} \\
&+[Ch]|_\eta^{i,j} u|_u^{i,j} \frac{o|_u^{i,j} o|_\eta^{i,j}}{\left(o|_\eta^{i-1,j} + o|_\eta^{i,j}\right) r\Delta\lambda \cos\vartheta|_\eta^j} \\
&-[Ch]|_\eta^{i,j} v|_v^{i,j+1} \frac{\cos\vartheta|_v^{j+1} o|_v^{i,j+1} o|_\eta^{i,j}}{\left(o|_\eta^{i,j+1} + o|_\eta^{i,j}\right) r\Delta\vartheta \cos\vartheta|_\eta^j} \\
&+[Ch]|_\eta^{i,j} v|_v^{i,j} \frac{\cos\vartheta|_v^{j} o|_v^{i,j} o|_\eta^{i,j}}{\left(o|_\eta^{i,j-1} + o|_\eta^{i,j}\right) r\Delta\vartheta \cos\vartheta|_\eta^j}
\end{aligned} \tag{A.7a}$$

$$\begin{aligned}
\text{diff.Ch}|_\eta^{i,j} = &\kappa_h h|_u^{i+1,j} \left(C|_\eta^{i+1,j} - C|_\eta^{i,j}\right) \frac{o|_u^{i+1,j}}{r^2(\Delta\lambda)^2 \cos\vartheta|_u^j \cos\vartheta|_\eta^j} \\
&+\kappa_h h|_u^{i,j} \left(C|_\eta^{i,j} - C|_\eta^{i-1,j}\right) \frac{-o|_u^{i,j}}{r^2(\Delta\lambda)^2 \cos\vartheta|_u^j \cos\vartheta|_\eta^j} \\
&+\kappa_h h|_v^{i,j+1} \left(C|_\eta^{i,j+1} - C|_\eta^{i,j}\right) \frac{o|_v^{i,j+1} \cos\vartheta|_v^{j+1}}{r^2(\Delta\vartheta)^2 \cos\vartheta|_\eta^j} \\
&+\kappa_h h|_v^{i,j} \left(C|_\eta^{i,j} - C|_\eta^{i,j-1}\right) \frac{-o|_v^{i,j} \cos\vartheta|_v^{j}}{r^2(\Delta\vartheta)^2 \cos\vartheta|_\eta^j}
\end{aligned} \tag{A.7b}$$

$$\text{relax.C}|_\eta^{i,j} = \gamma|_\eta^{i,j} h|_\eta^{i,j} \left(C|_\eta^{i,j} - C_0|_\eta^{i,j}\right) \tag{A.7c}$$

$$\text{forc.C}|_\eta^{i,j} = C|_\eta^{i,j} F_\eta|_\eta^{i,j} \tag{A.7d}$$

The consumption term is implicitly implemented. The tracer content Ch at the new timestep $k+1$ is thus calculated as

$$[Ch]|_{\eta}^{i,j,k+1} = \frac{[Ch]|_{\eta}^{i,j,k} + AB([Ch]|_{\eta}^{i,j})}{1 + J\Delta t} \tag{A.8}$$

A.2 The turbulent Sverdrup balance

Averaging the non-viscous and unforced version of the horizontal momentum equations (2.4a and 2.4b) and introducing the thickness-weighted averages of the potential vorticity and horizontal velocity yields

$$\frac{\partial \overline{u}}{\partial t} = \overline{h}\hat{v}\hat{q} - \frac{1}{r\cos\vartheta}\frac{\partial \overline{E}}{\partial \lambda} + \overline{hq''v''} \tag{A.9a}$$

$$\frac{\partial \overline{v}}{\partial t} = -\overline{h}\hat{u}\hat{q} - \frac{1}{r}\frac{\partial \overline{E}}{\partial \vartheta} - \overline{hq''u''} \tag{A.9b}$$

Taking the curl of these two equations and using the mean continuity equation

$$\frac{\partial \overline{h}}{\partial t} + \nabla \cdot \left(\overline{h}\hat{\mathbf{u}}\right) = 0 \tag{A.10}$$

yields the thickness-weighted potential vorticity equation (*Greatbatch*, 1998)

$$\frac{\partial \hat{q}}{\partial t} + \hat{\mathbf{u}} \cdot \nabla \hat{q} = -\frac{1}{\overline{h}} \nabla \cdot \overline{hq''\mathbf{u}''}. \tag{A.11}$$

For these non-viscous, unforced shallow water equations, the potential vorticity is conserved, i.e. $Dq/Dt = 0$. In a statistically steady state the "turbulent Sverdrup balance" (*Rhines and Holland*, 1979) is then given by

$$\hat{\mathbf{u}} \cdot \nabla \hat{q} = -\frac{1}{\overline{h}} \nabla \cdot \overline{hq''\mathbf{u}''} \tag{A.12}$$

which corresponds to Eq. 4.1. With $\hat{u}\partial q/\partial x$ almost vanishing the balance can be

expressed in spherical coordinates as

$$\hat{v}\overline{h} = -\left(\frac{\partial \hat{q}}{\partial y}\right)^{-1} \nabla \cdot \overline{hq''\mathbf{u}''} \tag{A.13}$$

This equation, in conjunction with the continuity equation, can be used to diagnose the time mean zonal mass flux due to the eddy flux convergence of potential vorticity (*Qiu et al.*, 2013a). The time mean continuity equation in steady state (and in Cartesian coordinates) is given by

$$\frac{\partial}{\partial x}\left(\hat{u}\overline{h}\right) + \frac{\partial}{\partial y}\left(\hat{v}\overline{h}\right) = 0 \tag{A.14}$$

Solving for $\hat{u}\overline{h}$ yields:

$$\hat{u}\overline{h} = -\int_{x_e}^{x} \frac{\partial}{\partial y}\left(\hat{v}\overline{h}\right) dx \tag{A.15}$$

Hence, plugging in equation A.13

$$\hat{u}\overline{h} = \int_{x_e}^{x} \frac{\partial}{\partial y}\left(\left(\frac{\partial \hat{q}}{\partial y}\right)^{-1} \nabla \cdot \overline{hq''\mathbf{u}''}\right) dx \tag{A.16}$$

With the Favre decomposition (Eq. 2.16) this can be rewritten as

$$\hat{u}\overline{h} = \int_{x_e}^{x} \frac{\partial}{\partial y}\left(\left(\frac{\partial \hat{q}}{\partial y}\right)^{-1} \nabla \cdot \left(\overline{hq\mathbf{u}} - \overline{h}\hat{q}\hat{\mathbf{u}}\right)\right) dx \tag{A.17}$$

Table A.1: Main variables and constants used in this study

Symbol	Name/Meaning	Value/Unit
A_0	Forcing amplitude	$3 \times 10^{-5}\ \mathrm{m\,s^{-1}}$
A_h	Lateral eddy viscosity	$100\,\mathrm{m^2\,s^{-1}}$
C	Tracer concentration	-
C_0	Relaxation field	-
c, c_{gr}	Gravity wave speed, group velocity	$\mathrm{m\,s^{-1}}$
E	Energy density	$\mathrm{m^2\,s^{-2}}$
F_u, F_v	Zonal, meridional momentum forcing	$\mathrm{m\,s^{-2}}$
F_η	Continuity equation forcing	$\mathrm{m\,s^{-1}}$
$f\ (= 2\Omega \sin\vartheta)$	Coriolis parameter	$\mathrm{s^{-1}}$
g	Gravitational acceleration	$\mathrm{m\,s^{-2}}$
g'	Reduced gravity	$1.5 \times 10^{-2}\ \mathrm{m\,s^{-2}}$
H	Undisturbed active layer depth	$500\,\mathrm{m}$
h	Total active layer depth	m
J	Tracer consumption rate	$0.0205\ \mathrm{yr^{-1}}$
k, l	zonal, meridional wavenumber	$\mathrm{m^{-1}}$
M_u, M_v	Zonal, meridional mixing of momentum	$\mathrm{m\,s^{-2}}$
$\mathbf{P}$ ($P_{\lambda\lambda}$, $P_{\lambda\vartheta}$, $P_{\vartheta\vartheta}$)	Momentum flux density tensor (viscous entries)	$(\mathrm{m^2\,s^{-2}})$
Q	uniform tracer consumption rate	$0.010\,25\ \mathrm{yr^{-1}}$
q, ζ	Potential vorticity, relative vorticity	$\mathrm{m^{-1}\,s^{-1}}$, $\mathrm{s^{-1}}$
r	Earth's radius	$6\,371\,000\,\mathrm{m}$
t	Time	s
U, V	Zonal, meridional mass flux	$\mathrm{m^2\,s^{-1}}$
$\mathbf{u} = (u, v)$	Horizontal velocity (zonal, meridional)	$\mathrm{m\,s^{-1}}$
x, y	Cartesian zonal, meridional coordinate	m
$\beta\ (= r^{-1}\partial f/\partial\vartheta)$	Meridional gradient of Coriolis parameter	$\mathrm{m^{-1}\,s^{-1}}$
γ	Zonally varying tracer relaxation rate	$\mathrm{s^{-1}}$
γ_0	Tracer relaxation rate at western boundary	$1/8.35\,\mathrm{d^{-1}}$
ζ	Relative vorticity	$\mathrm{s^{-1}}$
η	Downward interface displacement	m
κ_h	Lateral tracer diffusivity	$100\,\mathrm{m^2\,s^{-1}}$
λ, ϑ	Longitude, latitude	degrees
ξ	Upward surface displacement	m
ρ	Density	$\mathrm{kg\,m^{-3}}$
ρ_0	Active layer density	$1024\,\mathrm{kg\,m^{-3}}$
σ_0, σ_1	Potential density referenced to 0, 1000 dbar	$\mathrm{kg\,m^{-3}}$
χ	Triad instability growth rate	$\mathrm{s^{-1}}$
ψ	Quasi-geostrophic streamfunction	$\mathrm{m^2\,s^{-1}}$
Ω	Earth's angular velocity	$7.272205 \times 10^{-5}\ \mathrm{rad\,s^{-1}}$
ω, ω_{yr}	Frequency, annual frequency	$\mathrm{s^{-1}}$

Table A.2: Notation and symbols used in this study

Symbol	Name/Meaning
$\delta\alpha$, $\Delta\alpha$	Difference of variable α
$\partial\alpha_1/\partial\alpha_2$	Partial derivative of α_1 w.r.t. α_2
$D\alpha/Dt$	Rate of change of α following a fluid particle
$\nabla\alpha$	Horizontal gradient of α
$\nabla^{\perp}\alpha$	Horizontal gradient of α rotated by 90 °
$\nabla\cdot\alpha$	Horizontal divergence of α
$\overline{\alpha}$	Temporal mean of α
$\hat{\alpha}$	Thickness-weighted temporal mean of α
α'	Deviation of α from temporal mean
α''	Deviation of α from thickness-weighted temporal mean
$\langle\rangle^{\lambda\vartheta}$	Spatial average
$a\vert_b^{c,d}$	Variable a on grid b at zonal and meridional grid indices c, d
$AB(\alpha)$	Adams-Bashforth increment of variable α

Acknowledgements

I would like to thank my supervisors Prof. Dr. Martin Claus and Prof. Dr. Richard Greatbatch for sparking my interest in shallow water modelling and theoretical oceanography. Thank you for providing the model code, technical assistance and for many fruitful discussions of the analysis and results.

From a technical viewpoint, I would like to thank the Python community for many useful data analysis packages (NumPy, Matplotib, etc...), the World Ocean Atlas Database and NASA Earth Observations website for easy data access, and the high performance computing system at the Christian-Albrechts-Universität zu Kiel.

I would further like to thank Milan Klöwer, Ole Wulff and Swantje Bastin for facilitating a fun and productive working environment in the office with lots of stimulating discussions as well as mutual support and encouragement. Furthermore, I am indebted to Marius Kunte and Felix Wolf for proofreading the thesis.

In the end, I want to thank Laurène for her radiant optimism and my family for continuously supporting me throughout my whole studies.

Bibliography

Afanasyev, Y. D., S. O'Leary, P. B. Rhines, and E. Lindahl (2011), On the origin of jets in the ocean, *Geophysical & Astrophysical Fluid Dynamics*, *106*(2), 113–137, doi:10.1080/03091929.2011.562896.

Aiki, H., and R. J. Greatbatch (2012), Thickness-Weighted Mean Theory for the Effect of Surface Gravity Waves on Mean Flows in the Upper Ocean, *Journal of Physical Oceanography*, *42*(5), 725–747, doi:10.1175/JPO-D-11-095.1.

Arakawa, A. (1972), Design of the UCLA general circulation model, *Tech. Rep. Technical Report No. 7*, Dep. of Meteorology, Univ. of California, Los Angeles.

Arakawa, A., and V. R. Lamb (1981), A potential enstrophy and energy conserving scheme for the shallow water equations, *Monthly Weather Review*, *109*, 18–36.

Baldwin, M. P., P. B. Rhines, H. P. Huang, and M. E. McIntyre (2007), The jet-stream conundrum, *Science*, *315*(5811), 467–468.

Belmadani, A., E. Concha, D. Donoso, A. Chaigneau, F. Colas, N. A. Maximenko, and E. Di Lorenzo (2017), Striations and preferred eddy tracks triggered by topographic steering of the background flow in the eastern South Pacific, *Journal of Geophysical Research: Oceans*, *122*, doi:10.1002/2014JC010066.Received.

Berloff, P., I. Kamenkovich, and J. Pedlosky (2009), A Model of Multiple Zonal Jets in the Oceans: Dynamical and Kinematical Analysis, *Journal of Physical Oceanography*, *39*(11), 2711–2734, doi:10.1175/2009JPO4093.1.

Berloff, P., S. Karabasov, J. T. Farrar, and I. Kamenkovich (2011), On latency of

multiple zonal jets in the oceans, *Journal of Fluid Mechanics*, *686*, 534–567, doi: 10.1017/jfm.2011.345.

Brandt, P., V. Hormann, B. Bourlès, J. Fischer, F. A. Schott, L. Stramma, and M. Dengler (2008), Oxygen tongues and zonal currents in the equatorial Atlantic, *Journal of Geophysical Research*, *113*(C4), C04,012, doi:10.1029/2007JC004435.

Brandt, P., V. Hormann, A. Körtzinger, M. Visbeck, G. Krahmann, L. Stramma, R. Lumpkin, and C. Schmid (2010), Changes in the Ventilation of the Oxygen Minimum Zone of the Tropical North Atlantic, *Journal of Physical Oceanography*, *40*(8), 1784–1801, doi:10.1175/2010JPO4301.1.

Brandt, P., R. J. Greatbatch, M. Claus, S. H. Didwischus, V. Hormann, A. Funk, J. Hahn, G. Krahmann, J. Fischer, and A. Körtzinger (2012), Ventilation of the equatorial Atlantic by the equatorial deep jets, *Journal of Geophysical Research: Oceans*, *117*(12), 1–15, doi:10.1029/2012JC008118.

Brandt, P., H. W. Bange, D. Banyte, M. Dengler, S.-H. Didwischus, T. Fischer, R. J. Greatbatch, J. Hahn, T. Kanzow, J. Karstensen, A. Körtzinger, G. Krahmann, S. Schmidtko, L. Stramma, T. Tanhua, and M. Visbeck (2015), On the role of circulation and mixing in the ventilation of oxygen minimum zones with a focus on the eastern tropical North Atlantic, *Biogeosciences*, *12*(2), 489–512, doi:10.5194/bg-12-489-2015.

Brandt, P., M. Claus, R. J. Greatbatch, R. Kopte, J. M. Toole, W. E. Johns, and C. W. Böning (2016), Annual and Semiannual Cycle of Equatorial Atlantic Circulation Associated with Basin-Mode Resonance, *Journal of Physical Oceanography*, *46*(10), 3011–3029, doi:10.1175/JPO-D-15-0248.1.

Breitburg, D., L. A. Levin, A. Oschlies, M. Grégoire, F. P. Chavez, D. J. Conley, V. Garçon, D. Gilbert, D. Gutiérrez, K. Isensee, G. S. Jacinto, K. E. Limburg, I. Montes, S. W. A. Naqvi, G. C. Pitcher, N. N. Rabalais, M. R. Roman, K. A.

Rose, B. A. Seibel, M. Telszewski, M. Yasuhara, and J. Zhang (2018), Declining oxygen in the global ocean and coastal waters, *Science*, *359*(January), doi:10.1126/science.aam7240.

Buckingham, C. E., and P. C. Cornillon (2013), The contribution of eddies to striations in absolute dynamic topography, *Journal of Geophysical Research: Oceans*, *118*(1), 448–461, doi:10.1029/2012JC008231.

Buckingham, C. E., P. C. Cornillon, F. Schloesser, and K. Obenour (2014), Global observations of quasi-zonal bands in microwave sea surface temperature, *Journal of Geophysical Research: Oceans*, *119*, 1–27, doi:10.1002/2014JC010088.Received.

Cane, M. A., and D. W. Moore (1981), A note on low-frequency equatorial basin modes, *Journal of Physical Oceanography*, *11*, 1578–1584.

Centurioni, L. R., J. C. Ohlmann, and P. P. Niiler (2008), Permanent Meanders in the California Current System, *Journal of Physical Oceanography*, *38*(8), 1690–1710, doi:10.1175/2008JPO3746.1.

Chang, P., T. Yamagata, P. Schopf, S. K. Behera, J. Carton, W. S. Kessler, G. Meyers, T. Qu, F. Schott, S. Shetye, and S.-P. Xie (2006), Climate Fluctuations of Tropical Coupled Systems - The Role of Ocean Dynamics, *Journal of Climate*, *19*(20), 5122–5174, doi:10.1175/JCLI3903.1.

Charney, J. G. (1971), Geostrophic Turbulence, *Journal of Atmospheric Sciences*, *28*, 1087–1095.

Chelton, D. B., R. A. DeZoeke, M. G. Schlax, K. El Naggar, and N. Siwertz (1998), Geographical Variability of the First Baroclinic Rossby Radius of Deformation, *J. Phys. Oceanogr.*, *28*(1984), 433–460.

Chelton, D. B., M. G. Schlax, and R. M. Samelson (2011), Global observations of

nonlinear mesoscale eddies, *Progress in Oceanography*, *91*(2), 167–216, doi:10.1016/j.pocean.2011.01.002.

Chen, C., I. Kamenkovich, and P. Berloff (2016), Eddy Trains and Striations in Quasi-geostrophic Simulations and the Ocean, *Journal of Physical Oceanography*, *46*(9), 2807–2825, doi:10.1175/JPO-D-16-0066.1.

Chen, R., and G. R. Flierl (2015), The Contribution of Striations to the Eddy Energy Budget and Mixing: Diagnostic Frameworks and Results in a Quasigeostrophic Barotropic System with Mean Flow, *Journal of Physical Oceanography*, *45*(8), 2095–2113, doi:10.1175/JPO-D-14-0199.1.

Chen, R., G. R. Flierl, and C. Wunsch (2015), Quantifying and Interpreting Striations in a Subtropical Gyre: A Spectral Perspective, *Journal of Physical Oceanography*, *45*(2), 387–406, doi:10.1175/JPO-D-14-0038.1.

Chu, P. C., L. M. Ivanov, O. V. Melnichenko, and N. C. Wells (2007), On long baroclinic Rossby waves in the tropical North Atlantic observed from profiling floats, *Journal of Geophysical Research*, *112*(C5), C05,032, doi:10.1029/2006JC003698.

Claus, M., R. J. Greatbatch, and P. Brandt (2014), Influence of the Barotropic Mean Flow on the Width and the Structure of the Atlantic Equatorial Deep Jets, *Journal of Physical Oceanography*, *44*(9), 2485–2497, doi:10.1175/JPO-D-14-0056.1.

Courant, R., K. Friedrichs, and H. Lewy (1928), Über die partiellen differenzengleichungen in der mathematischen physik, *Mathematische Annalen*, *100*, 32–74.

Cravatte, S., W. S. Kessler, and F. Marin (2012), Intermediate Zonal Jets in the Tropical Pacific Ocean Observed by Argo Floats, *Journal of Physical Oceanography*, *42*(9), 1475–1485, doi:10.1175/JPO-D-11-0206.1.

Davis, A., E. Di Lorenzo, H. Luo, A. Belmadani, N. A. Maximenko, O. V. Melnichenko, and N. Schneider (2014), Mechanisms for the emergence of ocean stria-

tions in the North Pacific, *Geophysical Research Letters*, *41*, 948–953, doi:10.1002/2013GL057956.Received.

Diaz, R. J., and R. Rosenberg (2008), Spreading Dead Zones and Consequences for Marine Ecosystems, *Science*, *321*(5891), 926–929, doi:10.1126/science.1156401.

Dritschel, D. G., and M. E. McIntyre (2008), Multiple Jets as PV Staircases: The Phillips Effect and the Resilience of Eddy-Transport Barriers, *Journal of the Atmospheric Sciences*, *65*(3), 855–874, doi:10.1175/2007JAS2227.1.

Duteil, O., F. U. Schwarzkopf, C. W. Böning, and A. Oschlies (2014), Major role of the equatorial current system in setting oxygen levels in the eastern tropical Atlantic Ocean: a high resolution model study, *Geophysical Research Letters*, *41*, 2033–2040, doi:10.1002/2013GL058888.Received.

Eden, C. (2007), Eddy length scales in the North Atlantic Ocean, *Journal of Geophysical Research*, *112*(C6), C06,004, doi:10.1029/2006JC003901.

Eden, C., R. J. Greatbatch, and D. Olbers (2007), Interpreting Eddy Fluxes, *Journal of Physical Oceanography*, *37*(5), 1282–1296, doi:10.1175/JPO3050.1.

Favre, A. (1965), Review on space-time correlations in turbulent fluids, *Journal of Applied Mechanics*, *32*(2), 241–257.

Favre, A. (1983), Turbulence: Space-time statistical properties and behavior in supersonic flows, *Physics of Fluids*, *26*(10), 2851, doi:10.1063/1.864049.

Galperin, B., H. Nakano, H. P. Huang, and S. Sukoriansky (2004), The ubiquitous zonal jets in the atmospheres of giant planets and Earth's oceans, *Geophysical Research Letters*, *31*(13), 1–5, doi:10.1029/2004GL019691.

Garcia, H. E., T. P. Boyer, R. A. Locarnini, J. I. Antonov, A. V. Mishonov, O. K. Baranova, M. M. Zweng, J. R. Reagan, and D. R. Johnson (2014), *World Ocean*

Atlas 2013. Volume 3: dissolved oxygen, apparent oxygen utilization, and oxygen saturation, 27 pp.

Gent, P. R., J. Willebrand, T. J. McDougall, and J. C. McWilliams (1995), Parameterizing Eddy-Induced Tracer Transports in Ocean Circulation Models, *Journal of Physical Oceanography*, *25*, 463–474.

Gill, A. E. (1982), *Atmosphere-Ocean Dynamics*, 662 pp., International Geophysics Series, Academic Press, New-York.

Greatbatch, R. J. (1998), Exploring the Relationship between Eddy-Induced Transport Velocity, Vertical Momentum Transfer, and the Isopycnal Flux of Potential Vorticity, *Journal of Physical Oceanography*, *28*(3), 422–432, doi:10.1175/1520-0485(1998)028⟨0422:ETRBEI⟩2.0.CO;2.

Greatbatch, R. J. (2001), A Framework for Mesoscale Eddy Parameterization Based on Density-Weighted Averaging at Fixed Height, *Journal of Physical Oceanography*, *31*(9), 2797–2806, doi:10.1175/1520-0485(2001)031⟨2797:AFFMEP⟩2.0.CO;2.

Greatbatch, R. J., P. Brandt, M. Claus, S.-H. Didwischus, and Y. Fu (2012), On the Width of the Equatorial Deep Jets, *Journal of Physical Oceanography*, *42*(10), 1729–1740, doi:10.1175/JPO-D-11-0238.1.

Hahn, J., P. Brandt, R. J. Greatbatch, G. Krahmann, and A. Körtzinger (2014), Oxygen variance and meridional oxygen supply in the Tropical North East Atlantic oxygen minimum zone, *Climate Dynamics*, *43*(11), 2999–3024, doi:10.1007/s00382-014-2065-0.

Hahn, J., P. Brandt, S. Schmidtko, and G. Krahmann (2017), Decadal oxygen change in the eastern tropical North Atlantic, *Ocean Science Discussions*, *1*(January), 1–43, doi:10.5194/os-2016-102.

Helly, J. J., and L. a. Levin (2004), Global distribution of naturally occurring marine hypoxia on continental margins, *Deep Sea Research Part I: Oceanographic Research Papers*, *51*(9), 1159–1168, doi:10.1016/j.dsr.2004.03.009.

Hofmann, A. F., E. T. Peltzer, P. M. Walz, and P. G. Brewer (2011), Hypoxia by degrees: Establishing definitions for a changing ocean, *Deep-Sea Research Part I: Oceanographic Research Papers*, *58*(12), 1212–1226, doi:10.1016/j.dsr.2011.09.004.

Hormann, V., R. Lumpkin, and G. R. Foltz (2012), Interannual North Equatorial Countercurrent variability and its relation to tropical Atlantic climate modes, *Journal of Geophysical Research: Oceans*, *117*(4), 1–17, doi:10.1029/2011JC007697.

Hristova, H. G., J. Pedlosky, and M. A. Spall (2008), Radiating Instability of a Meridional Boundary Current, *Journal of Physical Oceanography*, *38*(10), 2294–2307, doi:10.1175/2008JPO3853.1.

Huang, H. P., A. Kaplan, E. N. Curchitser, and N. A. Maximenko (2007), The degree of anisotropy for mid-ocean currents from satellite observations and an eddy-permitting model simulation, *Journal of Geophysical Research: Oceans*, *112*(9), 1–12, doi:10.1029/2007JC004105.

Isachsen, P. E., J. H. LaCasce, and J. Pedlosky (2007), Rossby Wave Instability and Apparent Phase Speeds in Large Ocean Basins, *Journal of Physical Oceanography*, *37*(5), 1177–1191, doi:10.1175/JPO3054.1.

Ivanov, L. M., C. A. Collins, and T. M. Margolina (2012), Detection of oceanic quasi-zonal jets from altimetry observations, *Journal of Atmospheric and Oceanic Technology*, *29*(8), 1111–1126, doi:10.1175/JTECH-D-11-00130.1.

Kamenkovich, I., P. Berloff, and J. Pedlosky (2009a), Role of Eddy Forcing in the Dynamics of Multiple Zonal Jets in a Model of the North Atlantic, *Journal of Physical Oceanography*, *39*(6), 1361–1379, doi:10.1175/2008JPO4096.1.

Kamenkovich, I., P. Berloff, and J. Pedlosky (2009b), Anisotropic Material Transport by Eddies and Eddy-Driven Currents in a Model of the North Atlantic, *Journal of Physical Oceanography*, *39*(12), 3162–3175, doi:10.1175/2009JPO4239.1.

Kamenkovich, I., I. I. Rypina, and P. Berloff (2015), Properties and Origins of the Anisotropic Eddy-Induced Transport in the North Atlantic, *Journal of Physical Oceanography*, *45*(3), 778–791, doi:10.1175/JPO-D-14-0164.1.

Karstensen, J., L. Stramma, and M. Visbeck (2008), Oxygen minimum zones in the eastern tropical Atlantic and Pacific oceans, *Progress in Oceanography*, *77*(4), 331–350, doi:10.1016/j.pocean.2007.05.009.

Keeling, R. F., A. Körtzinger, and N. Gruber (2010), Ocean Deoxygenation in a Warming World, *Annual Review of Marine Science*, *2*(1), 199–229, doi:10.1146/annurev.marine.010908.163855.

Kushnir, Y., W. A. Robinson, P. Chang, and A. W. Robertson (2006), The Physical Basis for Predicting Atlantic Sector Seasonal-to-Interannual Climate Variability, *Journal of Climate*, *19*(23), 5949–5970, doi:10.1175/JCLI3943.1.

LaCasce, J. (2002), On turbulence and normal modes in a basin, *Journal of Marine Research*, *60*(3), 431–460, doi:10.1357/002224002762231160.

LaCasce, J. H., and J. Pedlosky (2004), The Instability of Rossby Basin Modes and the Oceanic Eddy Field, *Journal of Physical Oceanography*, *34*(9), 2027–2041, doi:10.1175/1520-0485(2004)034⟨2027:TIORBM⟩2.0.CO;2.

Locarnini, R. A., A. V. Mishonov, J. I. Antonov, T. P. Boyer, H. E. Garcia, O. K. Baranova, M. M. Zweng, C. R. Paver, J. R. Reagan, D. R. Johnson, M. Hamilton, and D. Seidov (2013), World Ocean Atlas 2013, Volume 1: Temperature, in *NOAA Atlas NESDIS 73*, edited by S. Levitus and A. V. Mishonov, p. 40 pp.

Luyten, J. R., J. Pedlosky, and H. Stommel (1983), The ventilated thermocline, *Journal of Physical Oceanography*, *13*, 292–309.

Malanotte-Rizzoli, P., K. Hedstrom, H. Arango, and D. B. Haidvogel (2000), Water mass pathways between the subtropical and tropical ocean in a climatological simulation of the North Atlantic ocean circulation, *Dynamics of Atmospheres and Oceans*, *32*(3-4), 331–371, doi:10.1016/S0377-0265(00)00051-8.

Marshall, D. P., B. Vogel, and X. Zhai (2013), Rossby rip currents, *Geophysical Research Letters*, *40*(16), 4333–4337, doi:10.1002/grl.50842.

Maximenko, N. A., B. Bang, and H. Sasaki (2005), Observational evidence of alternating zonal jets in the world ocean, *Geophysical Research Letters*, *32*(12), 1–4, doi:10.1029/2005GL022728.

Maximenko, N. A., O. V. Melnichenko, P. P. Niiler, and H. Sasaki (2008), Stationary mesoscale jet-like features in the ocean, *Geophysical Research Letters*, *35*(8), 1–6, doi:10.1029/2008GL033267.

Melnichenko, O. V., N. A. Maximenko, N. Schneider, and H. Sasaki (2010), Quasi-stationary striations in basin-scale oceanic circulation: Vorticity balance from observations and eddy-resolving model, *Ocean Dynamics*, *60*(3), 653–666, doi:10.1007/s10236-009-0260-z.

Nakano, H., and H. Hasumi (2005), A Series of Zonal Jets Embedded in the Broad Zonal Flows in the Pacific Obtained in Eddy-Permitting Ocean General Circulation Models, *Journal of Physical Oceanography*, *35*(4), 474–488, doi:10.1175/JPO2698.1.

Olbers, D., J. Willebrand, and C. Eden (2012), *Ocean dynamics*, 703 pp., Springer Science & Business Media, doi:10.1007/978-3-642-23450-7.

Oliphant, T. E. (2006), *A guide to NumPy*, vol. 1, Trelgol Publishing USA.

Ollitrault, M., and A. Colin de Verdière (2014), The Ocean General Circulation near 1000-m Depth, *Journal of Physical Oceanography*, *44*(1), 384–409, doi:10.1175/JPO-D-13-030.1.

Ollitrault, M., M. Lankhorst, D. Fratantoni, P. Richardson, and W. Zenk (2006), Zonal intermediate currents in the equatorial Atlantic Ocean, *Geophysical Research Letters*, *33*(5), 2–5, doi:10.1029/2005GL025368.

O'Reilly, C. H., A. Czaja, and J. H. Lacasce (2012), The emergence of zonal ocean jets under large-scale stochastic wind forcing, *Geophysical Research Letters*, *39*(11), 1–6, doi:10.1029/2012GL051684.

Panetta, R. L. (1993), Zonal Jets in Wide Baroclinically Unstable Regions: Persistence and Scale Selection, doi:10.1175/1520-0469(1993)050⟨2073:ZJIWBU⟩2.0.CO;2.

Paulmier, A., and D. Ruiz-Pino (2009), Oxygen minimum zones (OMZs) in the modern ocean, *Progress in Oceanography*, *80*(3-4), 113–128, doi:10.1016/j.pocean.2008.08.001.

Pedlosky, J. (1975), On Secondary Baroclinic Instability and the Meridional Scale of Motion in the Ocean, *Journal of Physical Oceanography*, *5*(4), 603–607, doi:10.1175/1520-0485(1975)005⟨0603:OSBIAT⟩2.0.CO;2.

Pedlosky, J. (1987), *Geophysical fluid dynamics*, 2 ed., Springer Verlag New York, doi:10.1007/978-1-4612-4650-3.

Pena-Izquierdo, J., E. Van Sebille, J. L. Pelegrí, J. Sprintall, E. Mason, P. J. Llanillo, and F. Machin (2015), Water mass pathways to the North Atlantic oxygen minimum zone, *Journal of Geophysical Research: Oceans*, *120*, 3350–3372, doi:10.1002/2014JC010557.Received.

Press, W. H., S. A. Teukolsky, W. T. Vetterling, and B. P. Flannery (1992), *Numerical Recipes in C: The Art of Scientific Computing*, 2 ed., Cambridge university press.

Qiu, B., S. Chen, and H. Sasaki (2013a), Generation of the North Equatorial Undercurrent Jets by Triad Baroclinic Rossby Wave Interactions, *Journal of Physical Oceanography*, *43*(12), 2682–2698, doi:10.1175/JPO-D-13-099.1.

Qiu, B., D. L. Rudnick, S. Chen, and Y. Kashino (2013b), Quasi-stationary North Equatorial Undercurrent jets across the tropical North Pacific Ocean, *Geophysical Research Letters*, *40*(10), 2183–2187, doi:10.1002/grl.50394.

Rhines, P. B. (1975), Waves and turbulence on a beta-plane, *Journal of Fluid Mechanics*, *69*(03), 417, doi:10.1017/S0022112075001504.

Rhines, P. B., and W. R. Holland (1979), A theoretical discussion of eddy-driven mean flows, *Dynamics of Atmospheres and Oceans*, *3*(2-4), 289–325, doi:10.1016/0377-0265(79)90015-0.

Sadourny, R. (1975), The Dynamics of Finite-Difference Models of the Shallow-Water Equations, doi:10.1175/1520-0469(1975)032⟨0680:TDOFDM⟩2.0.CO;2.

Salmon, R. (1982), Geostrophic Turbulence, in *Topics in Ocean Physics, Proceedings of the International School of Physics 'Enrico Fermi'*, pp. 30–78, Varenna, Italy.

Schlax, M. G., and D. B. Chelton (2008), The influence of mesoscale eddies on the detection of quasi-zonal jets in the ocean, *Geophysical Research Letters*, *35*(24), 1–5, doi:10.1029/2008GL035998.

Schmidtko, S., G. C. Johnson, and J. M. Lyman (2013), MIMOC: A global monthly isopycnal upper-ocean climatology with mixed layers, *Journal of Geophysical Research: Oceans*, *118*(4), 1658–1672, doi:10.1002/jgrc.20122.

Schmidtko, S., L. Stramma, and M. Visbeck (2017), Decline in global oceanic oxygen content during the past five decades, *Nature*, *542*(7641), 335–339, doi:10.1038/nature21399.

Schopf, P. S., D. L. T. Anderson, and R. Smith (1981), Beta-dispersion of low-frequency Rossby waves, *Dynamics of Atmospheres and Oceans*, *5*, 187–214.

Schütte, F., P. Brandt, and J. Karstensen (2016), Occurrence and characteristics of mesoscale eddies in the tropical northeastern Atlantic Ocean, *Ocean Science*, *12*, 663–685, doi:10.5194/os-12-663-2016.

Shchepetkin, A. F., and J. J. O'Brien (1996), A Physically Consistent Formulation of Lateral Friction in Shallow-Water Equation Ocean Models, *Monthly Weather Review*, *124*(June), 1285–1300.

Stramma, L., S. Hüttl, and J. Schafstall (2005), Water masses and currents in the upper tropical northeast Atlantic off northwest Africa, *Journal of Geophysical Research*, *110*(C12), C12,006, doi:10.1029/2005JC002939.

Stramma, L., G. C. Johnson, J. Sprintall, and V. Mohrholz (2008a), Expanding oxygen-minimum zones in the tropical oceans., *Science (New York, N.Y.)*, *320*(5876), 655–8, doi:10.1126/science.1153847.

Stramma, L., P. Brandt, J. Schafstall, F. Schott, J. Fischer, and A. Körtzinger (2008b), Oxygen minimum zone in the North Atlantic south and east of the Cape Verde Islands, *Journal of Geophysical Research*, *113*(C4), C04,014, doi:10.1029/2007JC004369.

Stramma, L., S. Schmidtko, L. A. Levin, and G. C. Johnson (2010), Ocean oxygen minima expansions and their biological impacts, *Deep Sea Research Part I: Oceanographic Research Papers*, *57*(4), 587–595, doi:10.1016/j.dsr.2010.01.005.

Stramma, L., E. D. Prince, S. Schmidtko, J. Luo, J. P. Hoolihan, M. Visbeck, D. W. R. Wallace, P. Brandt, and A. Körtzinger (2012a), Expansion of oxygen minimum zones may reduce available habitat for tropical pelagic fishes, *Nature Climate Change*, *2*(1), 33–37, doi:10.1038/nclimate1304.

Stramma, L., A. Oschlies, and S. Schmidtko (2012b), Mismatch between observed and modeled trends in dissolved upper-ocean oxygen over the last 50 yr, *Biogeosciences*, *9*(10), 4045–4057, doi:10.5194/bg-9-4045-2012.

Theiss, J. (2004), Equatorward Energy Cascade, Critical Latitude, and the Predominance of Cyclonic Vortices in Geostrophic Turbulence, *Journal of Physical Oceanography*, *34*, 1663–1678, doi:10.1175/1520-0485(2004)034⟨1663:EECCLA⟩2.0.CO;2.

Thomsen, S., T. Kanzow, G. Krahmann, R. J. Greatbatch, M. Dengler, and G. Lavik (2016), The formation of a subsurface anticyclonic eddy in the Peru-Chile Undercurrent and its impact on the near-coastal salinity, oxygen, and nutrient distributions, *Journal of Geophysical Research: Oceans*, *121*(1), 476–501, doi:10.1002/2015JC010878.

Van Geen, A., J. M. Smethie, A. Homeman, and H. Lee (2006), Sensitivity of the North Pacific oxygen minimum zone to changes in ocean circulation: A simple model calibrated by chlorofluorocarbons, *Journal of Geophysical Research: Oceans*, *111*(10), 1–11, doi:10.1029/2005JC003192.

Van Sebille, E., I. Kamenkovich, and J. K. Willis (2011), Quasi-zonal jets in 3-D Argo data of the northeast Atlantic, *Geophysical Research Letters*, *38*(2), 2–6, doi:10.1029/2010GL046267.

Vaquer-Sunyer, R., and C. M. Duarte (2008), Thresholds of hypoxia for marine biodiversity, *Proceedings of the National Academy of Sciences*, *105*(40), 15,452–15,457, doi:10.1073/pnas.0803833105.

Wang, J., M. A. Spall, G. R. Flierl, and P. Malanotte-Rizzoli (2012), A new mechanism for the generation of quasi-zonal jets in the ocean, *Geophysical Research Letters*, *39*(10), 2–5, doi:10.1029/2012GL051861.

Wyrtki, K. (1962), The oxygen minima in relation to ocean circulation, *Deep Sea*

Research and Oceanographic Abstracts, *9*(1-2), 11–23, doi:10.1016/0011-7471(62)90243-7.

Zhai, X., H. L. Johnson, and D. P. Marshall (2010), Significant sink of ocean-eddy energy near western boundaries, *Nature Geoscience*, *3*(9), 608–612, doi:10.1038/ngeo943.

Zweng, M. M., J. R. Reagan, J. I. Antonov, R. A. Locarnini, A. V. Mishonov, T. P. Boyer, H. E. Garcia, O. K. Baranova, D. R. Johnson, D. Seidov, and M. M. Biddle (2013), World Ocean Atlas 2013, Volume 2: Salinity, in *NOAA Atlas NESDIS 74*, edited by S. Levitus and A. V. Mishonov, p. 39 pp.

ERKLÄRUNG

Hiermit erkläre ich, dass ich die vorliegende Arbeit selbständig und ohne fremde Hilfe angefertigt und keine anderen als die angegebenen Quellen und Hilfsmittel verwendet habe. Die eingereichte schriftliche Fassung der Arbeit entspricht der auf dem elektronischen Speichermedium. (Name der Datei: Köhn_1005856.pdf) Weiterhin versichere ich, dass diese Arbeit noch nicht als Abschlussarbeit an anderer Stelle vorgelegen hat.

_____

Datum, Unterschrift